UNIVERSIDADE ESTADUAL PAULISTA
"JÚLIO DE MESQUITA FILHO"

FACULDADE DE ENGENHARIA BAURU

Heber Agnelo Antonel Fabbri

MODELING THE EFFECTS OF NATURAL FRACTURES ON THE PERMEABILITY OF RESERVOIR ROCKS

Bauru

2019

Heber Agnelo Antonel Fabbri

MODELING THE EFFECTS OF NATURAL FRACTURES ON THE PERMEABILITY OF RESERVOIR ROCKS

Dissertação apresentada à Faculdade de Engenharia de Bauru, Programa de Pós-Graduação em Engenharia Mecânica na Área de Projetos Mecânicos, como parte dos requisitos necessários à obtenção de Título de Mestre em Engenharia Mecânica.

Orientador: Prof. Dr. Osvaldo Luís Manzoli

Bauru

2019

Fabbri, Heber Agnelo Antonel.
Modeling the effects of natural fractures on the permeability of reservoir rocks / Heber Agnelo Antonel Fabbri, 2019
92 f. : il.

Orientador: Osvaldo Luís Manzoli

Dissertação (Mestrado)–Universidade Estadual Paulista. Faculdade de Engenharia de Bauru, Bauru, 2019

1. Fractured reservoir. 2. Hydromechanical coupling. 3. Barton-Bandis model. 4. interface finite elements with high aspect ratio. Universidade Estadual Paulista. Faculdade de Engenharia de Bauru. II. Título.

ATA DA DEFESA PÚBLICA DA DISSERTAÇÃO DE MESTRADO DE HEBER AGNELO ANTONEL FABBRI, DISCENTE DO PROGRAMA DE PÓS-GRADUAÇÃO EM ENGENHARIA MECÂNICA, DA FACULDADE DE ENGENHARIA - CÂMPUS DE BAURU.

Aos 12 dias do mês de julho do ano de 2019, às 09:00 horas, no(a) Anfiteatro da Seção Técnica de Pós-graduação da FEB, reuniu-se a Comissão Examinadora da Defesa Pública, composta pelos seguintes membros: Prof. Dr. OSVALDO LUIS MANZOLI - Orientador(a) do(a) Departamento de Engenharia Civil e Ambiental / Faculdade de Engenharia de Bauru - UNESP, Prof. Dr. MARCIO ARAB MURAD do(a) Coordenação de Modelagem Computacional / Laboratório Nacional de Computação Científica, Dr. LEONARDO CABRAL PEREIRA do(a) Centro de Pesquisas (CENPES) / Petrobras, sob a presidência do primeiro, a fim de proceder a arguição pública da DISSERTAÇÃO DE MESTRADO de HEBER AGNELO ANTONEL FABBRI, intitulada **MODELING THE EFFECTS OF NATURAL FRACTURES ON THE PERMEABILITY OF RESERVOIR ROCKS**. Após a exposição, o discente foi arguido oralmente pelos membros da Comissão Examinadora, tendo recebido o conceito final:_ _ _ _ APROVADO_ _ _. Nada mais havendo, foi lavrada a presente ata, que após lida e aprovada, foi assinada pelos membros da Comissão Examinadora.

Prof. Dr. OSVALDO LUIS MANZOLI
Prof. Dr. MARCIO ARAB MURAD
Dr. LEONARDO CABRAL PEREIRA

"Do not go where the path may lead; go instead where there is no path and leave a trail."

Ralph Waldo Emerson

Acknowledgements

Primeiramente gostaria de agradecer ao meus pais, Ismael e Maria Elvira, e minha irmã Milca por todo amor, apoio e suporte que sempre me deram. Sem vocês ao meu lado minha jornada não seria possível.

Agradeço ao professor Osvaldo Luís Manzoli por ter sido meu orientador e mentor, por ter acreditado e confiado em mim, pelas críticas e elogios, ambos indispensáveis ao meu aperfeiçoamento acadêmico. Agradeço também aos os professores da pós-graduação, em especial aos professores Marcos Silveira, Roger Augusto Rodrigues, Caio Nogueira e Heraldo Luiz Giacheti, pelo auxílio ao longo do mestrado.

Agradeço aos amigos e colegas do mestrado, Pedro Cleto, Eduardo Rodrigues, José Ambiel, Alfredo Saab, Breno Rocha, Isabela Silveira, Jhaber Yacoub, Marcela Gimenes, Murilo Camargo e Júlio Fernandes pelo altruísmo, confiança, convivência e cafés tomados ao longo de todo o curso de mestrado.

O presente trabalho foi realizado com apoio da Coordenação de Aperfeiçoamento de Pessoal de Nível Superior – Brasil (CAPES) – Código de Financiamento 001, e da Petrobras – Termo de Compromisso nº 2016/00129-1.

Abstract

FABBRI, H. A. A., MODELING THE EFFECTS OF NATURAL FRACTURES ON THE PERMEABILITY OF RESERVOIR ROCKS, Engineering College of Bauru, UNESP - São Paulo State University, 2019, 78 p., Dissertation (Master's degree).

This work presents a numerical method based on Discrete Fracture Model (DFM) and the Finite Element Method (FEM), where the fractures are approximated by a reduced model. The flow along and across the fracture is described by a simplified set of equations considering both conductive fractures and barriers. The coupled hydromechanical model is composed of a linear poroelastic Biot medium and a nonlinear model based on damage mechanics for the fractures, which captures the nonlinear normal deformation and shear dilation according to the Barton-Bandis model. Both flow and geomechanical models are approximated using the finite element model. Fractures are explicitly represented by three-node standard finite elements with high aspect ratio (i.e. ratio between the largest and the smallest element dimensions) and appropriate constitutive laws. These interface high aspect ratio elements represent a regularization method which continuously approximate the discontinuous pressure and displacement fields on a narrow material band around the fracture. The complete mathematical formulation is presented together with the algorithm suggested for its numerical implementation. The efficiency of the proposed method is demonstrated through numerical examples, as well as the effects of fractures in the hydraulic properties of porous rocks and its dependency of the stress state.

Keywords: Fractured reservoir, hydromechanical coupling, Barton-Bandis model, interface finite elements with high aspect ratio.

Resumo

FABBRI, H. A. A., MODELAGEM DO EFEITO DE FRATURAS NATURAIS NA PERMEABILIDADE DE ROCHAS RESERVATÓRIO, Faculdade de Engenharia de Bauru, UNESP - Universidade Estadual Paulista, 2019, 78 p., Dissertação (Mestrado).

Este trabalho apresenta um método numérico baseado no Modelo de Fratura Discreta (MFD) e no Método dos Elementos Finitos (MEF), onde as fraturas são aproximadas por um modelo reduzido. O fluxo ao longo e através da fratura é descrito por um conjunto simplificado de equações, considerando tanto fraturas condutoras quanto barreiras. O modelo hidromecânico acoplado é composto por um meio poroelástico linear e um modelo não linear para fraturas, baseado na mecânica do dano e que captura a deformação normal não linear e a dilatância ao cisalhamento de acordo com o modelo de Barton-Bandis. Os modelos de fluxo e geomecânico são aproximados usando o método dos elementos finitos. As fraturas são explicitamente representadas por elementos finitos triangulares de três nós com elevada razão de aspecto (isto é, a razão entre a maior e a menor dimensão do elemento) e leis constitutivas apropriadas. Esses elementos de elevada razão de aspecto representam um método de regularização que aproxima de forma contínua os campos de pressão e deslocamento descontínuos em uma estreita faixa material ao redor da fratura. A formulação matemática completa é apresentada juntamente com o algoritmo sugerido para sua implementação numérica. A eficiência do método proposto é demonstrada através de exemplos numéricos, bem como os efeitos de fraturas nas propriedades hidráulicas de rochas porosas e sua dependência do estado de tensão.

Palavras-chave: Reservatórios fraturados, aclopamento hidromecânico, model de Barton-Bandis, elementos finitos de interface com elevada razão de aspecto.

List of Figures

LIST OF TABLES

CONTENTS

CHAPTER 1

INTRODUCTION

The problem of coupled fluid flow and geomechanics is encountered in many areas of geoscience. Geomaterials usually contain pores and other cavities, like fractures and vugs, that are deformable and filled with fluid under saturated or unsaturated conditions. The pressure of the fluid in the void space and the deformation of the medium are intimately related in the so-called hydromechanical coupling, which has been studied in depth since the classical works of Terzaghi (1925) and Biot (1941). Changes in the fluid pressure of a geological formation due to injection or removal of fluid can lead to geomechanical deformation. The understanding of these mechanisms is required in water management, for instance, to avoid subsidence due to excessive ground-water pumping (BUDHU, 2011; RUTQVIST; STEPHANSSON, 2003). Similar mechanisms are encountered in oil and gas recovery processes (DUSSEAULT, 2011; FREDRICH et al., 2000). Geomechanical effects are expected to be particularly important in rock formations, once they generally contain or develop discontinuities. Fractures often play an important role in the hydrodynamic behavior of the system, strongly affecting the flow. Since fracture's permeability may greatly differ from that on the surrounding medium, they introduce heterogeneity in the medium. As a consequence, the fractures hydraulic behavior may range from acting as preferential paths for flow, making flow in certain directions several orders of magnitude faster than in others, or act as barriers, blocking flow in certain directions and possibly isolating some part of the fluid. Another factor of complexity is the fracture deformation (opening or closing, sliding and propagation) due to fluid pressure variations, which means also the aperture or closure of a preferential flow path (TSANG; RUTQVIST; MIN, 2007; OLSSON; BARTON, 2001). Therefore, the understanding of the hydromechanical response of fractured rock plays an important role in many geotechnical engineering applications such as unconventional oil and gas production, aquifers performance, contaminant transport, geothermal energy production, water retention in dam reservoirs, to cite just a few. As numerical simulations are very important for the planning of subsurface operations, there exist an important demand for numerical methods capable of accurately treating fractured domains.

1.1 LITERATURE REVIEW

The study of mechanical behavior of a single rock fracture under different loading conditions can be divided into two main categories: filled and unfilled fractures. The mechanical behavior of unfilled fractures is a function of the roughness and compressive strength of the fracture walls, while the behavior of filled fractures depends mainly on the physical and mineralogical properties of the material separating the fracture walls (BARTON; CHOUBEY, 1977). The nonlinear relation between compressive stress and fracture closure was first investigated by Goodman, Taylor e Brekke (1968), Goodman (1974). Later, Bandis, Lumsden e Barton (1983) proposed the hyperbolic equation relating the closure to the compressive stress.

The prediction of the shear strength of non-planar rock fractures has been addressed by many researchers that reported curved relationships between the shear strength of the rock fractures and the normal stress, including Krsmanović e Langof (1964), Jaeger (1971), Patton et al. (1966). Degradation of fracture asperities was also investigated by several authors (LADANYI; ARCHAMBAULT et al., 1969; JAEGER, 1971; BARTON, 1973; BARTON, 1976; SAEB; AMADEI, 1992; HOMAND; BELEM; SOULEY, 2001; HENCHER; RICHARDS, 2015; ZHU; LI; DENG, 2018).

The prediction of the dilation phenomenon of regular or irregular fractures subjected to direct shear loading has been addressed by Ladanyi, Archambault et al. (1969), Jaeger (1971), Barton (1973), Bandis, Lumsden e Barton (1983), Barton, Bandis e Bakhtar (1985), Plesha (1987), Jing (1990), Olsson e Barton (2001), among others.

Several empirical and theoretical constitutive models were proposed to give a quantitative description of the mechanical properties of rock fractures, following two main approaches: the theoretical approach, which adopts known theories like plasticity, contact theory, etc. to simulate the observed behavior; and the empirical approach, in which physical data are analyzed to derive correlations between variables of influence and models are formulated according to observed behavior. Theoretical and empirical models were developed by several authors, including Goodman (1974), Barton e Choubey (1977), Bandis, Lumsden e Barton (1983), Plesha (1987), Jing (1990), Gens, Carol e Alonso (1990), Saeb e Amadei (1992), Amadei e Stephansson (1997), Samadhiya, Viladkar e Al-Obaydi (2008).

From the numerical perspective, due to the scale discrepancy of several orders of magnitude between the width of the fractures and the other physical dimensions involved in the problem, and since fracture width is usually much smaller than the typical mesh size, it is unreasonable and often completely unaffordable to make a mesh refinement such that the fracture may be represented exactly. There exist many models in literature addressing this issue, which may be classified in three main groups: the simplest group of models, which are frequently used for very large domains, replace the fractured domain by an equivalent continuum medium that averages the properties of both the porous medium and fractures by some homogenization technique (JACKSON; HOCH; TODMAN, 2000; LONG et al., 1982; ODA, 1985). Other models, called double porosity models, distinguish between the flow properties of the intact matrix and fractures network (BARENBLATT; ZHELTOV; KOCHINA, 1960; WARREN; ROOT et al., 1963; KAZEMI et al., 1976; DEAN; LO et al., 1988; ARBOGAST; DOUGLAS JR; HORNUNG, 1990; JR; ARBOGAST, 1990; WU et al., 2011). Such models do not resolve the fractures geometrically, instead they include the fractures as one or more overlaying continua as a form to incorporate the micro-scale effects on the macro scale without the necessity of the high spatial resolutions. The interaction of the different continua is expressed through exchange terms. The third group of models, called discrete fracture models (DFM), explicitly include the geometries of individual fractures, which are meshed and often introduce additional degrees of freedom to the global system. This model allow the explicit computation of fluid exchange between fractures and the surrounding medium (JAFFRÉ; MNEJJA; ROBERTS, 2011; KARIMI-FARD; FIROOZABADI et al., 2001; KARIMI-FARD et al., 2003; BACA; ARNETT; LANGFORD, 1984; MORALES; SHOWALTER, 2010; MORALES; SHOWALTER, 2012).

The present work deals with DFM, and more precisely is concerned with models where fractures are approximated based on a reduced model, where flow along and across the fracture is described using a simplified set of equations. Some works treat the fracture as interfaces: Segura e Carol (2004) employed zero-thickness finite elements to treat single-phase flow in a fractured porous medium in the context of finite elements, and latter extended the element in Segura e Carol (2008a) and Segura e Carol (2008b) to treat hydro-mechanical coupling. The work of Alboin et al. (1999), which uses mixed finite elements, introduces a model where the fractures are modeled as $(d-1)$ dimensional interfaces in an d dimensional medium. The fractures are assumed to have a high permeability, so the pressure considered continuous across the fractures. The flux, however, is not supposed to be continuous as the fluid could flow into and out of as well as along the fractures. The works of Martin, Jaffré e Roberts (2005), Faille et al. (2002), which also provide a comprehensive derivation of the formulation used in this work, generalized the model in order to handle both large and small permeability in the fracture, therefore it is no longer assumed that pressure is continuous across the fracture. An extension of this model incorporating a Forchheimer's correction to Darcy's law is then presented in Frih, Roberts e Saada (2008). Two-phase flow was also addressed by Jaffré, Mnejja e Roberts (2011). Finite-volume methods has also been applied to DFM by Reichenberger et al. (2006), Karimi-Fard et al. (2003), Ahmed et al. (2015), Gläser et al. (2017). The embedded discrete-fracture models (e-DFM) are another class of models where two independent grids for fractures and matrix may be used. The advantage of these models is that a simple structured mesh can be used for the matrix, which substantially facilitates grid generation. Examples of e-DFM are given in Lee et al. (1999), Li, Lee et al. (2006), Faille et al. (2016), Ţene et al. (2017).

1.2 Objectives of the work

In order to assess the influence of fractures on the permeability of reservoir rocks, DFM formulation are employed for simulate coupled single-phase flow and geomechanics. This work has two objectives: the first one is to propose a new DFM approach based on standard finite elements to model single-phase flow in a porous media containing fractures and barriers. The second one is to extend this model to treat coupled flow and geomechanics, considering fractures deformation according to the Barton-Bandis joint model. The fractures are explicitly represented by three-node standard finite elements with high aspect ratio (i.e. ratio between the largest and the smallest element dimensions). These high aspect ratio elements have been used before to model cracks in reinforced concrete (MANZOLI et al., 2014), desiccation soil crack networks (SÁNCHEZ; MANZOLI; GUIMARÃES, 2014) and hydraulic fracturing (MANZOLI et al., 2019), so its natural the idea of using this elements to treat natural fractures. For the flow model, its is demonstrated that by equipping the high aspect ratio (HAR) elements with appropriate constitutive laws, when the aspect ratio increases, the pressure and Darcy velocity fields in the element tend to the fracture-interface model (lower-dimensional formulation (ANGOT; BOYER; HUBERT, 2009; MARTIN; JAFFRÉ; ROBERTS, 2005)). For the geomechanical model, its is demonstrated that these HAR elements equipped with appropriate constitutive laws are able to reproduce, in a computationally efficient way, complex fracture mechanical behavior like nonlinear normal closure and shear dilation, according to the Barton-Bandis model. This proposed approach has several advantages, for example it uses a mesh composed by standard finite elements only, usually available in FEM codes, together with an appropriate constitutive model. The discontinuity is handled in a completely continuous approach, without the need of implementing special interpolation functions or integration rules (as it happens in most of the existing approaches). Thus, it is relatively simple to upgrade existing FEM codes to tackle engineering problems involving fractures and/or barriers in porous media.

1.3 Outline

Chapter 2 addresses the problem of fluid flowing through a fractured porous media. A reduced dimension model is derived to represent fractures on a d dimensional domain as $(d-1)$ dimensional geometrical entities. According to this model, the fluid pressure and flow velocity may be discontinuous across the fracture. An appropriate regularization method is presented, where the discontinuous pressure field, called *strong discontinuity regime*, can be approximated by a continuous field, called *regularized discontinuity regime*, posed over a narrow material domain around the fracture, called *regularization band*. It is shown that the original discontinuous pressure field is recovered in the limit case where the width h of the *regularization band* tends to zero.

Chapter 3 deals with the finite element discretization of the flow problem on fractured porous media. The weak form of the *regularized discontinuity regime* is derived and it is shown that it converges to the weak form of the *strong discontinuity regime* when the width h of the *regularization band* tends to zero. The finite element discretization of the weak form of the *regularized discontinuity regime* is presented, with the *regularization band* been explicitly discretized by interface HAR finite elements, which are basically degenerated three-node triangular elements. It is shown that as the aspect ratio (ratio of the largest to the smallest dimension) of a standard three-node triangular element increases, the element pressure and Darcy velocity tends towards the ones of the fracture model.

Chapter 4 presents a general framework for the formulation of coupled flow and geomechanics with constitutive relations consistent with Biot's theory, based on the approach of Coussy (2004). The fractures are incorporated by extending the reduced dimension model from chapter 2 to account coupled flow geomechanics. The model results in a discontinuous displacement field and a (possibly) discontinuous pressure field. The pressure and displacement field are regularized similarly to chapter 2.

Chapter 5 focuses on the mechanical behavior of rock fractures. The Barton-Bandis constitutive model for fracture is presented in details. A continuum constitutive (stress-strain) relation based on damage mechanics and consistent with the regularized displacement field is proposed to represent fracture mechanical response according to the Barton-Bandis model.

Chapter 6 deals with the finite element discretization of the coupled flow and geomechanics problem on fractured porous media. The weak form of the governing equations for the regularized problem is presented, with its corresponding finite element discretization. It is shown that the interface HAR elements are suited to represent the pressure and displacement field of the fracture, as long as their aspect ratio is high.

Chapter 7 discuss the main numerical results related to the validate the proposed approach. It is shown through synthetic benchmarks that the flow model is able to properly represent both fractures and barriers. Numerical simulations of uniaxial compression test and direct shear test show that the geomechanical model is able to reproduce the nonlinear normal deformation and shear dilation of fractures. The coupled hydromechanical model is used to investigate the stress dependency of the permeability of fractured porous rocks. Finally, chapter 8 brings the dissertation results and conclusions.

CHAPTER 2

MODELING FLUID FLOW ON FRACTURED POROUS MEDIA

2.1 MATHEMATICAL MODEL

The starting point of this work is to describe fluid flow on a porous domain containing geological discontinuities, as fractures and barriers. The porous domain is assumed to be fully saturated with a single phase fluid such that the flow is governed by the mass conservation equation and the Darcy's law. Steady flow is assumed. Without any loss of generality, gravitational effects can be neglected, which leads to a simplified notation. The main unknown of the problem is the pressure field p.

2.1.1 GLOBAL DARCY'S MODEL

Let $\Omega \subset \mathbb{R}^d$, $d = 2$ or 3, be porous domain with boundary $\Gamma = \partial\Omega$ and outward normal $\mathbf{n}$. For this model, suppose that the fracture splits the domain Ω into two subdomains: the porous matrix Ω_m and the fracture domain Ω_f. Assume that there exist a hyperplane $\Sigma \subset \Omega_f$ (i.e. a line for $d = 2$ and surface for $d = 3$ (see Fig. 2.1(a)), such that:

$$\Omega_f = \left\{ \boldsymbol{s} + r\boldsymbol{\nu} | \boldsymbol{s} \in \Sigma,\ r \in \left(-\frac{w}{2}, \frac{w}{2} \right) \right\},$$

where w denotes the fracture aperture and $\boldsymbol{\nu}(\boldsymbol{s})$ denotes the unit normal vector to Σ at point $\boldsymbol{s} \in \Sigma$. The unit vector $\boldsymbol{\tau}(\boldsymbol{s})$ tangential to Σ at point $\boldsymbol{s}$ (in $d = 2$ dimensions $\boldsymbol{\tau}$ will be a vector and in $d = 3$ dimensions will be a 3×2 matrix whose columns constitute an orthonormal basis for the tangent plane to Σ) is defined such that $(\boldsymbol{\tau}, \boldsymbol{\nu})$ is positively oriented.

According to the different porous microstructure of the bulk and the fracture, different permeability tensors $\mathbf{K}_m \in \Omega_m$ and $\mathbf{K}_f \in \Omega_f$ are considered porous matrix and the fracture domain, respectively. The tensor $\mathbf{K}_f$ is assumed to be block-diagonal according to the local coordinate system $(\boldsymbol{\tau}, \boldsymbol{\nu})$, i.e.

$$\mathbf{K}_f = \begin{pmatrix} \mathrm{K}_{f,\tau} & 0 \\ 0 & \mathrm{K}_{f,\nu} \end{pmatrix}, \tag{2.1}$$

where $\mathrm{K}_{f,\nu}$ is the transversal (normal) permeability and $\mathrm{K}_{f,\tau}$ is the longitudinal (tangential) permeability tensor. Although it is possible to take into account smooth variations of $\mathbf{K}_m$ and $\mathbf{K}_f$, both are assumed uniform for sake of simplicity.

Within the above assumptions, the problem is to find the pressure field solution to the following global Darcy problem:

$$\boldsymbol{\nabla} \cdot \boldsymbol{v} = q \quad \text{in } \Omega, \tag{2.2}$$

$$\boldsymbol{v} = -\frac{1}{\mu}\mathbf{K}(\mathbf{x})\boldsymbol{\nabla} p \quad \text{in } \Omega, \tag{2.3}$$

$$p = p_D \quad \text{on } \Gamma_D, \tag{2.4}$$

$$\boldsymbol{v} \cdot \mathbf{n} = q_N \quad \text{on } \Gamma_N, \tag{2.5}$$

where $\mathbf{K}(\mathbf{x}) = \mathbf{K}_m$ for $\mathbf{x} \in \Omega_m$ and $\mathbf{K}(\mathbf{x}) = \mathbf{K}_f$ for $\mathbf{x} \in \Omega_f$, μ is the fluid viscosity, q is source/sink term and p_D and q_N are the prescribed pressure and flow on the Dirichlet and Newmann boundary parts Γ_D and Γ_N, respectively, with $\overline{\Gamma_D \cup \Gamma_N} = \Gamma$ and $\Gamma_D \cap \Gamma_N = \emptyset$.

Notice that, since the typical size of fracture's aperture is small compared to the length scale of the fracture, that is $w \ll |\Sigma|$, it is unreasonable and often completely unaffordable to make a mesh refinement such that the fracture may be represented exactly. Therefore, the objective is to simplify the geometry of the fracture domain Ω_f by the hyperplane Σ, aiming to provide a good approximation of the flow in the considered fractured media.

2.1.2 REDUCED DIMENSION MODEL

In what follows, a reduced dimension model is derived based on the model presented by Martin, Jaffré e Roberts (2005), Frih, Roberts e Saada (2008), Angot, Boyer e Hubert (2009). The main idea is to reduce the d dimensional fracture domain Ω_f inside Ω by the $(d-1)$ dimensional hyperplane Σ. As a consequence, the porous domain Ω_m will be replaced by the larger set $\tilde{\Omega}_m = \Omega \setminus \Sigma$, such that $\Omega = \tilde{\Omega}_m \cup \Sigma$ and $\partial\tilde{\Omega}_m = \Gamma \cup \Sigma$. The following notation is adopted in the sequel of this work:

- The hyperplane Σ divides the domain Ω into two open disjoint subdomains Ω^+ and Ω^-, such that $\Omega = \Omega^- \cup \Sigma \cup \Omega^+$ (see Figure 2.1).

- Let $\mathbf{n}$ be the outward unit normal vector on the boundary Γ of the porous domain, and $\boldsymbol{\nu}$ the unit normal vector on Σ oriented from Ω^- to Ω^+. The outward unit normal to $\partial\Omega^+$ on Σ is then $\mathbf{n}^+ = -\boldsymbol{\nu}$ and the outward unit normal to $\partial\Omega^-$ on Σ is $\mathbf{n}^- = \boldsymbol{\nu}$.

- The following notations are adopted for the jump and the average of any function ψ that may be discontinuous across Σ:

$$[\![\psi]\!] = \psi^+ - \psi^-, \qquad \{\!\{\psi\}\!\} = \frac{1}{2}\left(\psi^+ + \psi^-\right),$$

where ψ^+ and ψ^- are the traces of ψ on each side of Σ, i.e.:

$$\psi^\pm = \lim_{\varepsilon \to 0^\pm} \psi\left(\boldsymbol{x} + \varepsilon \boldsymbol{\nu}\right), \quad \boldsymbol{x} \in \Sigma.$$

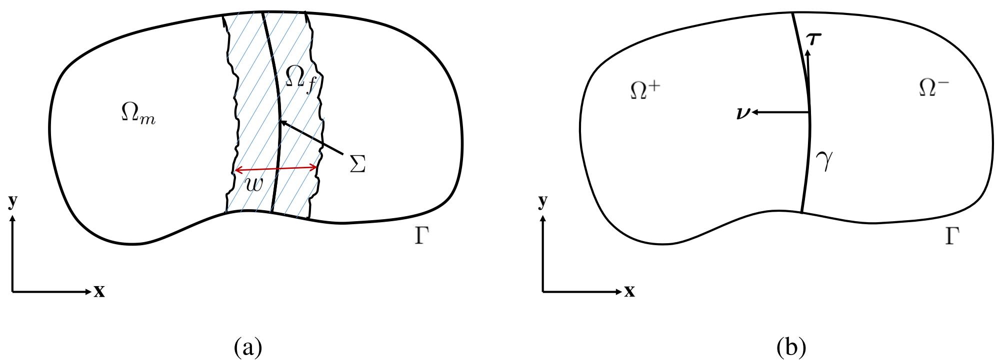

Figure 2.1: (a) Original domain Ω with fracture Ω_f. (b) Reduced dimension domain with fracture represented by the hyperplane Σ.

The first part of this model consists in writing the governing equations inside the new larger porous matrix domain $\tilde{\Omega}_m = \Omega \setminus \Sigma$:

$$\boldsymbol{\nabla} \cdot \boldsymbol{v} = q \quad \text{in } \Omega \setminus \Sigma, \tag{2.6}$$

$$\boldsymbol{v} = -\frac{1}{\mu}\mathbf{K}_m \boldsymbol{\nabla} p \quad \text{in } \Omega \setminus \Sigma, \tag{2.7}$$

$$p = p_D \quad \text{on } \Gamma_D, \tag{2.8}$$

$$\boldsymbol{v} \cdot \mathbf{n} = q_N \quad \text{on } \Gamma_N. \tag{2.9}$$

It is emphasize here the fact that the above system of equations is posed on the domain $\Omega \setminus \Sigma$, with constant permeability $\mathbf{K}_m$. The properties of the fracture Σ have not been taken into account and therefore the system of equations is not closed yet. In order to derive the supplementary set of equations posed on the fracture Σ which will complete the problem, the following cross-section mean values of the variables are defined:

$$\boldsymbol{v}_{f,\tau}(s) = \frac{1}{w}\int_{-\frac{w}{2}}^{\frac{w}{2}} \boldsymbol{v}(s,t)\cdot\boldsymbol{\tau}(s)\ dt, \tag{2.10}$$

$$\boldsymbol{v}_{f,\nu}(s) = \frac{1}{w}\int_{-\frac{w}{2}}^{\frac{w}{2}} \boldsymbol{v}(s,t)\cdot\boldsymbol{\nu}(s)\ dt, \tag{2.11}$$

$$p_f(s) = \frac{1}{w}\int_{-\frac{w}{2}}^{\frac{w}{2}} p(s,t)\ dt, \tag{2.12}$$

$$q_f(s) = \frac{1}{w}\int_{-\frac{w}{2}}^{\frac{w}{2}} q(s,t)\ dt. \tag{2.13}$$

Integrating the mass conservation equation (2.2) and the Darcy's law (2.3) over the cross-section of the fracture, one obtains:

$$\boldsymbol{\nabla}_\tau \cdot (w\boldsymbol{v}_{f,\tau}) = wq_f - [\![\boldsymbol{v}\cdot\boldsymbol{\nu}]\!], \tag{2.14}$$

$$\boldsymbol{v}_{f,\tau} = -\frac{1}{\mu}\mathrm{K}_{f,\tau}\boldsymbol{\nabla}_\tau p_f, \tag{2.15}$$

$$\boldsymbol{v}_{f,\nu} = -\frac{1}{\mu}\mathrm{K}_{f,\nu}\frac{[\![p]\!]}{w}. \tag{2.16}$$

$$\tag{2.17}$$

where $\boldsymbol{\nabla}_\tau$ and $\boldsymbol{\nabla}_\tau\cdot$ denote the tangential gradient and divergent operators along Σ, respectively. Adopting the trapezoidal quadrature rule to approximate the mean variables:

$$p_f \approx \{\!\{p\}\!\}, \qquad \boldsymbol{v}_{f,\nu} \approx \{\!\{\boldsymbol{v}\cdot\boldsymbol{\nu}\}\!\}, \tag{2.18}$$

we obtain the reduced model of flow along the fracture Σ:

$$\boldsymbol{\nabla}_\tau \cdot (w\boldsymbol{v}_{f,\tau}) = wq_f - [\![\boldsymbol{v}\cdot\boldsymbol{\nu}]\!] \quad \text{on } \Sigma, \tag{2.19}$$

$$\boldsymbol{v}_{f,\tau} = -\frac{1}{\mu}\mathrm{K}_{f,\tau}\boldsymbol{\nabla}_\tau p_f \quad \text{on } \Sigma, \tag{2.20}$$

$$\boldsymbol{v}_{f,\nu} = \{\!\{\boldsymbol{v}\cdot\boldsymbol{\nu}\}\!\} = -\frac{1}{\mu}\mathrm{K}_{f,\nu}\frac{[\![p]\!]}{w} \quad \text{on } \Sigma, \tag{2.21}$$

$$p_f = \{\!\{p\}\!\} \quad \text{on } \Sigma. \tag{2.22}$$

$$\tag{2.23}$$

Remark 1 *The model can be generalized to other quadrature rules in place of the trapezoidal rule to approximate the cross-section mean values of the pressure p_f and of $\boldsymbol{v}\cdot\boldsymbol{\nu}$. Following Martin, Jaffré e Roberts (2005), Frih, Roberts e Saada (2008), Angot, Boyer e Hubert (2009), eq.* (2.18) *may be replaced by:*

$$p_f = \{\!\{p\}\!\} + \frac{(2\xi-1)\mu}{4K_{f,\nu}}w[\![\boldsymbol{v}\cdot\boldsymbol{\nu}]\!], \quad \textit{on } \Sigma, \tag{2.24}$$

where $\xi \geq 1/2$ is a quadrature parameter. For example, the trapezoidal rule (2.18) *is recovered for $\xi = 1/2$, while the use of the mid-point rule gives $\xi = 3/4$. Martin, Jaffré e Roberts (2005) and Frih, Roberts e Saada (2008) proved that the problem is well-posed for values of $\xi > 1/2$ (typically $\xi = 2/3$, $\xi = 3/4$ or $\xi = 1$), while Angot, Boyer e Hubert (2009) also proved the well-posedness of the problem for $\xi = 1/2$, and concluded that $\xi = 1/2$ leads to more precise results. Throughout this work we will only consider the case $\xi = 1/2$.*

Gathering the previous equations, the resulting problem reads:

$$\boldsymbol{\nabla} \cdot \boldsymbol{v} = q \quad \text{in } \Omega \setminus \Sigma, \tag{2.25}$$

$$\boldsymbol{v} = -\frac{1}{\mu}\mathbf{K}\boldsymbol{\nabla} p \quad \text{in } \Omega \setminus \Sigma, \tag{2.26}$$

$$\boldsymbol{\nabla}_\tau \cdot (w\boldsymbol{v}_{f,\tau}) = wq_f - [\![\boldsymbol{v} \cdot \boldsymbol{\nu}]\!] \quad \text{on } \Sigma, \tag{2.27}$$

$$\boldsymbol{v}_{f,\tau} = -\frac{1}{\mu}\mathrm{K}_{f,\tau}\boldsymbol{\nabla}_\tau p_f \quad \text{on } \Sigma, \tag{2.28}$$

$$\boldsymbol{v}_{f,\nu} = \{\!\{\boldsymbol{v} \cdot \boldsymbol{\nu}\}\!\} = -\frac{1}{\mu}\mathrm{K}_{f,\nu}\frac{[\![p]\!]}{w} \quad \text{on } \Sigma, \tag{2.29}$$

$$p_f = \{\!\{p\}\!\} \quad \text{on } \Sigma, \tag{2.30}$$

$$p = p_D \quad \text{on } \Gamma_D, \tag{2.31}$$

$$\boldsymbol{v} \cdot \mathbf{n} = q_N \quad \text{on } \Gamma_N. \tag{2.32}$$

Here, $\boldsymbol{v}_{f,\nu}$ and $\boldsymbol{v}_{f,\tau}$ are the averaged transversal and longitudinal Darcy's velocity, respectively, and q_f is the source/sink term on Σ. Equation (2.27) is the mass conservation equation in the $(d-1)$ dimensional domain Σ, with the term $[\![\boldsymbol{v} \cdot \boldsymbol{\nu}]\!]$ accounting for the fluid exchange between the fracture and the surrounding porous medium. Equation (2.28) corresponds to the averaged Darcy's law in the longitudinal direction along the fracture. Finally, Eq. (2.29) corresponds to the averaged Darcy's law in the transversal direction, with the term $\mathrm{K}_{f,\nu}/w$ providing a coupling condition between the transversal fluxes and the pressure drop across the fracture:

$$p^+ - p^- = [\![p]\!] = -\frac{\mu w}{\mathrm{K}_{f,\nu}}\boldsymbol{v}_{f,\nu}. \tag{2.33}$$

The study of geological discontinuities can be divided into two main categories: discontinuities filled with granular material and the unfilled ones. Some geological discontinuities may represent an obstacle for the transversal flow, due to the physical and mineralogical properties of the infill material separating the fracture walls. This can be observed, for instance, in many petroleum reservoirs with sealing faults that act as impermeable barriers. Unfilled discontinuities, on the other hand, may be highly conductive, representing no obstacle for the transversal flow (i.e. $\mathrm{K}_{f,\nu} \to \infty$). Then, according to Eq. (2.33), since the transversal flow $\boldsymbol{v}_{f,\nu}$ must be bounded, we can suppose that the pressure p is continuous through Σ:

$$p^{-} = p_f = p^{+}. \tag{2.34}$$

Physically, due to the complex roughness pattern of fracture's walls and their three-dimensional character, opposite surfaces will be in contact, in general, only in some areas and will be separated in others, forming an interconnected network of open space where fluid can flow. This open space defines the fracture's flow characteristics, of which the effective longitudinal permeability is the most important (BARTON; BANDIS; BAKHTAR, 1985; OLSSON; BARTON, 2001; JING; STEPHANSSON, 2007). For practical purpose the flow along unfilled fractures is generally idealized as a laminar flow between smooth parallel plates. Under those conditions, the flow is proportional to the pressure gradient in the longitudinal direction by the cube of the aperture, according to the so-called cubic law (LOMIZE, 1951; SNOW, 1965). The cubic law validity has been widely studied both experimentally and numerically and confirmed for a large range of situations, and can be corrected to account the effects fracture tortuosity and roughness (LOMIZE, 1951; WITHERSPOON et al., 1980; ZIMMERMAN; BODVARSSON, 1996; OLSSON; BARTON, 2001).

2.2 CONTINUOUS APPROACH OF THE DISCONTINUOUS PRESSURE

2.2.1 DECOMPOSITION OF THE DISCONTINUOUS PRESSURE FIELD

Let us consider the pressure field $p(\mathbf{x})$ discontinuous on Σ, defined by:

$$p(\mathbf{x}) = \overline{p} + H_\Sigma(\mathbf{x})[\![p]\!](\mathbf{x}), \tag{2.35}$$

where $\mathbf{x}$ stands for the material points of Ω, $[\![p]\!]$ is the pressure discontinuity across Σ, $\overline{p}$ is the continuous counterpart of p, and $H_\Sigma(\mathbf{x})$ is the Heaviside function placed along Σ:

$$H_\Sigma(\mathbf{x}) = \begin{cases} 0 & \text{if} \quad \mathbf{x} \in \Omega^{-}, \\ \dfrac{1}{2} & \text{if} \quad \mathbf{x} \in \Sigma, \\ 1 & \text{if} \quad \mathbf{x} \in \Omega^{+}. \end{cases} \tag{2.36}$$

The gradient of the pressure field (2.35) is given by:

$$\boldsymbol{\nabla} p = \underbrace{\boldsymbol{\nabla}\overline{p} + H_\Sigma \boldsymbol{\nabla}[\![p]\!]}_{\boldsymbol{\nabla}\hat{p}\ \text{(bounded)}} + \underbrace{\delta_\Sigma [\![p]\!]\boldsymbol{\nu}}_{\boldsymbol{\nabla}\tilde{p}\ \text{(unbounded)}}, \tag{2.37}$$

where δ_Σ is the Dirac delta function posed along Σ. Note that $\boldsymbol{\nabla} p$ can be decomposed into $\boldsymbol{\nabla}\hat{p}$,

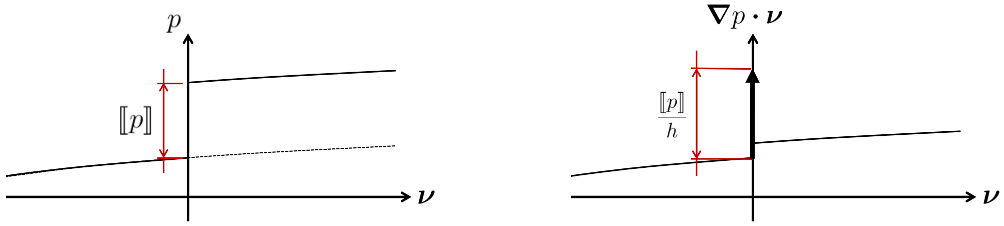

(a) (b)

Figure 2.2: (a) Pressure field and (b) pressure gradient for the *strong discontinuity regime*.

which is discontinuous but bounded, and the unbounded counterpart $\boldsymbol{\nabla}\tilde{p}$ (see Fig. 2.2). The pressure field defined by Eqs (2.35) and (2.37) will be referred hereafter as *strong discontinuity regime*.According to Eqs. (2.25)-(2.32), the pressure field and Darcy's velocity are (possibly) discontinuous, yet at most bounded across Σ. Therefore, since $\mathbf{K}_f$ is not null, bounded Darcy's velocities can not be obtained from the *strong discontinuity regime*.

2.2.2 Regularized discontinuity pressure field

Consider the subdomain $\Omega_\Sigma \subset \Omega$, hereafter referred as *regularization band*, corresponding to a narrow material band centered in Σ with width $h > 0$, $\Omega_\Sigma = \{\mathbf{s} + t\boldsymbol{\nu}; \mathbf{s} \in \Sigma,\ t \in [-\frac{h}{2}, \frac{h}{2}]\}$, enclosed by the material surfaces Σ^+ and Σ^- (see fig. 2.3), so that Ω_Σ collapses into Σ when h tends to zero. The discontinuous pressure field (2.35) can be interpreted as the limit when $h \to 0$ of the continuous field (*regularized discontinuity regime*):

$$p(\mathbf{x}) = \overline{p} + Z_{\Omega_\Sigma}(\nu)[\![p]\!](\mathbf{x}), \tag{2.38}$$

where ν is the coordinate of the material point $\mathbf{x}$ according to the local coordinate system (τ, ν) along Σ, such that $\mathbf{x}(\tau, 0) = \Sigma$, $\mathbf{x}(\tau, -h/2) = \Sigma^-$ and $\mathbf{x}(\tau, h/2) = \Sigma^+$ (see Fig. 2.3), and $Z_{\Omega_\Sigma}(\nu)$ is the continuous *unit ramp function*, defined by:

$$Z_{\Omega_\Sigma}(\nu) = \begin{cases} 0 & \text{if} \quad \nu < -h/2, \\ \dfrac{1}{2} + \dfrac{\nu}{h} & \text{if} \quad -h/2 \leq \nu \leq h/2, \\ 1 & \text{if} \quad \nu > h/2. \end{cases} \tag{2.39}$$

The gradient of the pressure (2.38) is given by:

$$\boldsymbol{\nabla} p = \underbrace{\boldsymbol{\nabla}\overline{p} + Z_{\Omega_\Sigma}(\nu)\boldsymbol{\nabla}[\![p]\!]}_{\boldsymbol{\nabla}\hat{p}\ \text{(continuous)}} + \underbrace{\frac{\mu_{\Omega_\Sigma}(\nu)}{h}[\![p]\!]\boldsymbol{\nu}}_{\boldsymbol{\nabla}\tilde{p}\ \text{(bounded)}}, \tag{2.40}$$

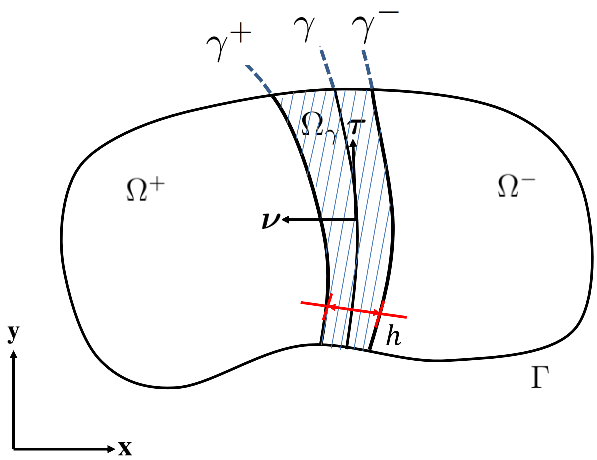

Figure 2.3: Regularization band.

where $\mu_{\Omega_\Sigma}(\nu)$ is the collocation function posed on Ω_Σ ($\mu_{\Omega_\Sigma}(\nu) = 1$ if $-h/2 \leq \nu \leq h/2$ and $\mu_{\Omega_\Sigma}(\nu) = 0$ otherwise), $\boldsymbol{\nabla}\hat{p}$ is the continuous part of $\boldsymbol{\nabla}p$ and $\boldsymbol{\nabla}\tilde{p}$ is the discontinuous (bounded) counterpart, as illustrated by Fig. 2.4. Therefore, bounded Darcy's velocities can be obtained from the *regularized discontinuity regime*.

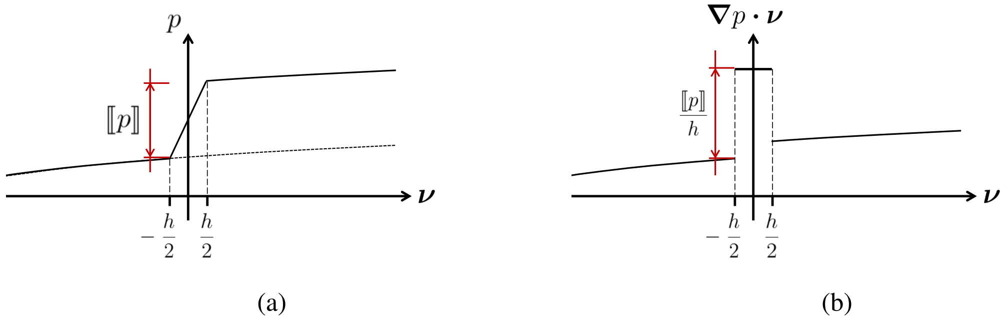

Figure 2.4: (a) Regularized pressure field and (b) pressure gradient for the *regularized discontinuity regime*.

Remark 2 *Note that when $h \to 0$, $Z_{\Omega_\Sigma} \to H_\Sigma$ and $\mu_{\Omega_\Sigma}/h \to \delta_\Sigma$. Therefore the regularized discontinuity regime tends to the strong discontinuity regime when h tends to zero.*

Remark 3 *For relatively small values of h in comparison to the typical size of Ω, the weak discontinuity regime can be considered representative of the strong discontinuity regime.*

2.2.3 Modeling the effects of the discontinuity on the flow problem

The basic idea behind the numerical scheme proposed in this work is to explicitly discretize the *regularization band* with proper interface finite elements that will be presented on sec. 3.2.1.

The effects of the fracture Σ are accounted on Ω_Σ by incorporating into the mass conservation equation and Darcy's law an appropriate source/sink term and permeability tensor, such that:

$$\tilde{\mathbf{K}}(\mathbf{x}) = \begin{cases} \mathbf{K}_m, & \text{for } \mathbf{x} \in \Omega \setminus \Omega_\Sigma, \\ \dfrac{h\mathrm{K}_{f,\nu}}{w}\boldsymbol{\nu} \otimes \boldsymbol{\nu} + \dfrac{w\mathrm{K}_{f,\tau}}{h}\boldsymbol{\tau} \otimes \boldsymbol{\tau}, & \text{for } \mathbf{x} \in \Omega_\Sigma, \end{cases} \tag{2.41}$$

and

$$\tilde{q}(\mathbf{x}) = \begin{cases} q, & \text{for } \mathbf{x} \in \Omega \setminus \Omega_\Sigma, \\ \dfrac{wq_f}{h}, & \text{for } \mathbf{x} \in \Omega_\Sigma, \end{cases} \tag{2.42}$$

where $\otimes$ denotes the dyadic product. Within the previous definitions, the govern equations of the problem can be written, according to the *regularized discontinuity regime*, as:

$$\boldsymbol{\nabla} \cdot \tilde{\boldsymbol{v}} = \tilde{q} \quad \text{in } \Omega, \tag{2.43}$$

$$\tilde{\boldsymbol{v}} = -\frac{1}{\mu}\tilde{\mathbf{K}}\boldsymbol{\nabla} p \quad \text{in } \Omega, \tag{2.44}$$

$$p = p_D \quad \text{on } \Gamma_D, \tag{2.45}$$

$$\boldsymbol{v} \cdot \mathbf{n} = q_N \quad \text{on } \Gamma_N. \tag{2.46}$$

Remark 4 *Despite the similarity between the system of equations governing the global model, Eqs.* (2.2) *to* (2.5)*, and the one governing the regularized discontinuity regime, Eqs.* (2.43) *to* (2.46)*, they are not directly related. The former requires the explicit representation of the fracture actual geometry, while the later is a regularized form of the reduced dimension model given by Eqs.* (2.25) *to* (2.32)*. The width h of the regularization band becomes merely a mesh parameter on the finite element solution of the later model, and is completely unrelated to the fracture aperture $w(\boldsymbol{s})$.*

CHAPTER 3

FINITE ELEMENT SCHEME FOR THE FLOW PROBLEM

3.1 WEAK FORM OF THE GOVERNING EQUATIONS

The starting point for the finite element method is to obtain the weak form of the governing equations (2.43)-(2.46). Let $\mathcal{H}^1(\Omega)$ be the space of functions with square integrable derivatives in Ω and denote $\mathcal{V}$ the solution function space for the fluid pressure, satisfying the essential boundary conditions:

$$\mathcal{V} = \left\{ \eta = \overline{\eta} + Z_{\Omega_\Sigma}(\nu)[\![\eta]\!] \mid \overline{\eta},\ [\![\eta]\!] \in \mathcal{H}^1(\Omega), \eta = p_D \text{ on } \Gamma_D \right\}, \tag{3.1}$$

and $\mathcal{V}_0$ the corresponding test function space satisfying the homogeneous counterpart of the essential boundary conditions:

$$\mathcal{V}_0 = \left\{ \eta = \overline{\eta} + Z_{\Omega_\Sigma}(\nu)[\![\eta]\!] \mid \overline{\eta},\ [\![\eta]\!] \in \mathcal{H}^1(\Omega), \eta = 0 \text{ on } \Gamma_D \right\}. \tag{3.2}$$

Using standard arguments, i.e. integrating the governing equations multiplied by a test functions $\psi \in \mathcal{V}_0$, applying the divergence theorem and imposing the natural boundary conditions, the weak form of the problem reads:

Find $p \in \mathcal{V}$ such that:

$$\int_\Omega \boldsymbol{\nabla}\psi \cdot \left(\frac{1}{\mu} \tilde{\mathbf{K}} \boldsymbol{\nabla} p \right) d\Omega = - \int_{\Gamma_N} \psi q_N d\Gamma + \int_\Omega \psi \tilde{q} d\Omega, \quad \forall\ \psi \in \mathcal{V}_0. \tag{3.3}$$

Writing the weak form (3.3) in Ω_Σ, one obtains:

$$\int_{\Omega_\Sigma} \boldsymbol{\nabla}\psi \cdot \left(\frac{1}{\mu} \tilde{\mathbf{K}} \boldsymbol{\nabla} p \right) d\Omega = - \int_{\Sigma^+} \psi q_{\Sigma^+} d\Gamma - \int_{\Sigma^-} \psi q_{\Sigma^-} d\Gamma + \int_{\Omega_\Sigma} \psi \tilde{q} d\Omega, \tag{3.4}$$

where $q_{\Sigma^+} = \boldsymbol{v}_{|_{\Sigma^+}} \cdot \boldsymbol{\nu}$ and $q_{\Sigma^-} = \boldsymbol{v}_{|_{\Sigma^-}} \cdot (-\boldsymbol{\nu})$ stands for the fluid flow from Ω_Σ through its boundaries, Σ^+ and Σ^-. From Eqs. (2.41) and (2.42), equation (3.4) becomes:

$$\int_\Sigma \int_{-\frac{h}{2}}^{\frac{h}{2}} \boldsymbol{\nabla}\psi \cdot \frac{1}{\mu}\left(\frac{h\mathrm{K}_{f,\nu}}{w}\boldsymbol{\nu}\otimes\boldsymbol{\nu} + \frac{w\mathrm{K}_{f,\tau}}{h}\boldsymbol{\tau}\otimes\boldsymbol{\tau}\right)\boldsymbol{\nabla}p \, d\nu d\tau = \\ -\int_{\Sigma^+}\psi q_{\Sigma^+}\cdot\boldsymbol{\nu} d\Gamma - \int_{\Sigma^-}\psi q_{\Sigma^-} d\Gamma + \int_\Sigma \int_{-\frac{h}{2}}^{\frac{h}{2}} \psi\left(\frac{wq_f}{h}\right) d\nu d\tau. \quad (3.5)$$

Recalling the approximation of the *regularized discontinuity regime*, the gradient of the pressure field and test function can be decomposed according to the local (τ,ν) reference frame, yielding:

$$\boldsymbol{\nabla}p = \boldsymbol{\nabla}_\tau\hat{p} + \boldsymbol{\nabla}_\nu\hat{p} + \frac{[\![p]\!]}{h}\boldsymbol{\nu}, \quad (3.6)$$

$$\boldsymbol{\nabla}\psi = \boldsymbol{\nabla}_\tau\hat{\psi} + \boldsymbol{\nabla}_\nu\hat{\psi} + \frac{[\![\psi]\!]}{h}\boldsymbol{\nu}, \quad (3.7)$$

where $\boldsymbol{\nabla}_\nu$ stands for the normal gradient, and $\boldsymbol{\nabla}\hat{p}$ and $\boldsymbol{\nabla}\hat{\psi}$ are the continuous part of $\boldsymbol{\nabla}p$ and $\boldsymbol{\nabla}\psi$, respectively. Therefore, Eqs. (3.6) and (3.7) imply the continuity of the tangential gradient, since it only depends on the continuous part of the gradient.

Using Eqs. (3.6) and (3.7) into Eq. (3.5), taking the limit when $h \to 0$ and recalling that in the limit situation $\Sigma^\pm \to \Sigma$, one obtains:

$$\int_\Sigma [\![\psi]\!]\frac{1}{\mu}\left(\frac{\mathrm{K}_{f,\nu}}{w}[\![p]\!]\right) d\tau + \int_\Sigma \boldsymbol{\nabla}_\tau\psi_{|\Sigma}\cdot\frac{1}{\mu}\left(w\mathrm{K}_{f,\tau}\boldsymbol{\nabla}_\tau p_{|\Sigma}\right) d\tau = \\ -\int_\Sigma \underbrace{\psi^+(v^+\cdot\boldsymbol{\nu}) - \psi^-(v^-\cdot\boldsymbol{\nu})}_{[\![\psi\boldsymbol{v}\cdot\boldsymbol{\nu}]\!]} d\tau + \int_\Sigma \psi_{|\Sigma} w q_f d\tau. \quad (3.8)$$

From the continuity of the tangential gradient $\boldsymbol{\nabla}_\tau p_{|\Sigma} = \boldsymbol{\nabla}_\tau p_f$ and $\boldsymbol{\nabla}_\tau\psi_{|\Sigma} = \boldsymbol{\nabla}_\tau\psi_f$, where $\psi_f = \{\!\{\psi\}\!\} = \psi_{|\Sigma}$ (see Eqs. (2.38) and (2.39)). Making use of the identity $[\![ab]\!] = [\![a]\!]\{\!\{b\}\!\} + \{\!\{a\}\!\}[\![b]\!]$, Eq. (3.8) reads:

$$\int_\Sigma [\![\psi]\!]\left(\frac{1}{\mu}\frac{\mathrm{K}_{f,\nu}}{w}[\![p]\!]\right) d\tau + \int_\Sigma \boldsymbol{\nabla}_\tau\psi_f\cdot\left(\frac{1}{\mu}w\mathrm{K}_{f,\tau}\boldsymbol{\nabla}_\tau p_f\right) d\tau = \\ -\int_\Sigma [\![\psi]\!]\{\!\{\boldsymbol{v}\cdot\boldsymbol{\nu}\}\!\} d\tau - \int_\Sigma \psi_f[\![\boldsymbol{v}\cdot\boldsymbol{\nu}]\!] d\tau + \int_\gamma \psi_f w q_f d\tau. \quad (3.9)$$

Finally, from Eq. (2.29), the first term on the left hand side of Eq. (3.9) cancels out with the first term on the right hand side, yielding:

$$\int_\Sigma \boldsymbol{\nabla}_\tau\psi_f\cdot\left(\frac{1}{\mu}w\mathrm{K}_{f,\tau}\boldsymbol{\nabla}_\tau p_f\right) d\tau = \int_\gamma \psi_f w q_f d\tau - \int_\Sigma \psi_f[\![\boldsymbol{v}\cdot\boldsymbol{\nu}]\!] d\tau, \quad (3.10)$$

which is the weak form of the averaged mass conservation equation in the discontinuity Σ (Eq. (2.27)) including the coupling condition (Eq. (2.29)). Therefore, Eq. (3.3) intrinsically accounts for the mass conservation equation in the discontinuity and the fluid exchange with the surrounding porous medium.

3.2 Finite element aproximation

Following the usual framework of the finite element method, let $\mathcal{T}_h$ be a partition of the domain Ω into n_{elem} nonoverlapping elements E_j, such that $\Omega \approx \Omega^h = \cup_{j=1}^{n_{elem}} E_j$ and $\Omega_\Sigma^h \subset \Omega^h$ is a finite element discretization of the *regularization band* Ω_Σ, as shown on Fig. 3.1. The finite element space associated with the standard Galerkin finite element method requires only $\mathcal{C}^0$ continuity:

$$\mathcal{V}^h = \left\{\eta^h = \overline{\eta}^h + Z_{\Omega_\Sigma}(\nu)[\![\eta]\!]^h \mid \overline{\eta}^h, [\![\eta]\!]^h \in \mathcal{C}^0(\Omega)\right\}, \tag{3.11}$$

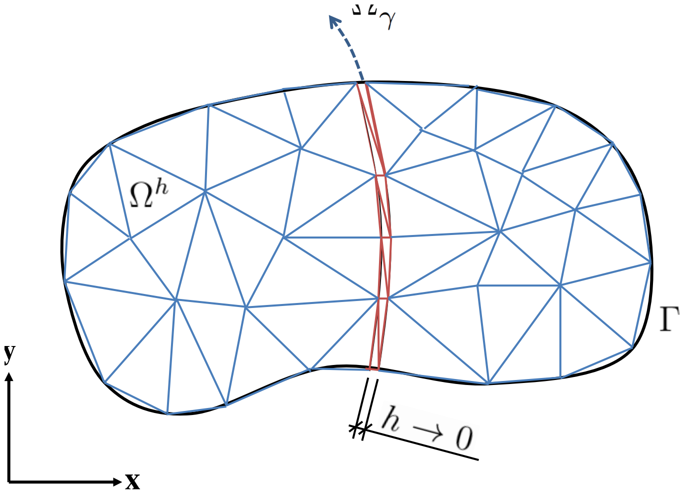

Figure 3.1: Finite element discretizetion Ω^h of Ω. The *regularization band* Ω_Σ is discretized with interface HAR elements.

where $\mathcal{P}^1(E_j)$ denotes the polynomial space of degree 1 on E_j. The standard finite element approximation of the pressure field is given by:

$$p^h = \sum_{i=j}^{n_{elem}} \varphi_j \mathbf{P}_j, \tag{3.12}$$

where φ_j and $\mathbf{P}_j$ are the standard finite element shape functions and the nodal pressures of the element E_j. Applying Galerking technique, the finite element discretization of Eq. (3.3) reads:

$$\mathbf{K}^p \mathbf{P} = \mathbf{Q}^p, \tag{3.13}$$

where $\mathbf{P}$ is the vector of nodal pressures and $\mathbf{K}^p$ and $\mathbf{Q}^p$ are given by:

$$\mathbf{K}^p_{i,j} = \int_\Omega \boldsymbol{\nabla}\varphi_i \frac{1}{\mu} \tilde{\mathbf{K}} \boldsymbol{\nabla}\varphi_j d\Omega, \tag{3.14}$$

$$\mathbf{Q}_i^p = -\int_{\Gamma_N} \varphi_i q_N d\Gamma + \int_{\Omega} \varphi_i \tilde{q} d\Omega. \tag{3.15}$$

3.2.1 Interface HAR finite element for the fluid flow problem

Consider a standard three-node finite element with base b and height h, as shown in Fig 3.2. The finite element approximation of the of the gradient of pressure via standard shape functions is given by:

$$\boldsymbol{\nabla} p^h = \boldsymbol{\nabla} \hat{p}^h + \underbrace{\frac{1}{h}[\![p]\!]^h \boldsymbol{\nu}}_{\boldsymbol{\nabla}\tilde{p}^h}, \tag{3.16}$$

where $\boldsymbol{\nu}$ is the unit vector normal to the element base, $\boldsymbol{\nabla}\hat{p}^h$ is the part of $\boldsymbol{\nabla} p^h$ that do not depend on the element height h and $[\![p]\!]^h$ is the difference of pressure between the node (1) and its projection on the base of the element $(1')$. Note that expression (3.16) is equivalent to (2.40).

According to the local coordinate system (τ, ν), Eq. (3.16) reads:

$$\boldsymbol{\nabla}\hat{p}^h = \frac{1}{b}\left\{ \begin{array}{c} p^{(3)} - p^{(2)} \\ 0 \end{array} \right\}, \tag{3.17}$$

$$\boldsymbol{\nabla}\tilde{\boldsymbol{p}}^h = \frac{1}{h}\left\{ \begin{array}{c} 0 \\ [\![p]\!] \end{array} \right\}, \tag{3.18}$$

where $p^{(1)}$, $p^{(2)}$ and $p^{(3)}$ are the pressures on the nodes (1), (2) and (3), respectively, $[\![p]\!]^h = p^{(1)} - p^{(1')}$, and $p^{(1')} = p^{(3)} b_2/b + p^{(2)}(1 - b_2/b)$.

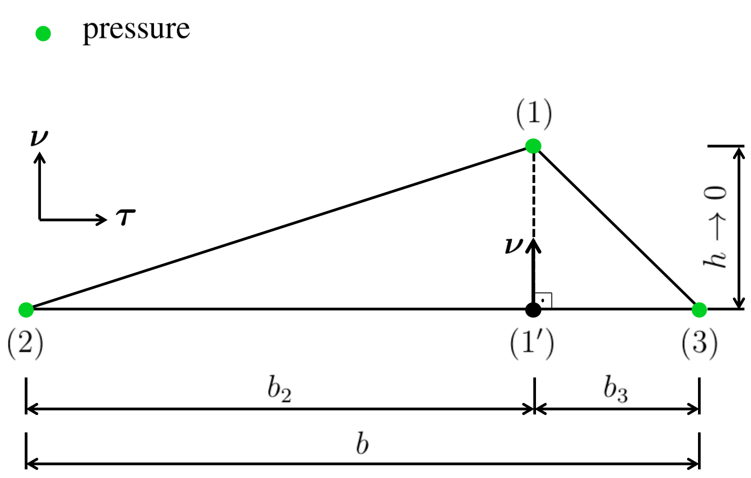

Figure 3.2: Three nodes solid finite element with high aspect ratio (adapted from (MANZOLI et al., 2012)).

Denoting AR $= b/h$ the aspect ratio of the element, the interface HAR elements are defined as three-node finite elements with high values of aspect ratio. Note that when the element height h tends to zero, node (1) and its base projection $(1')$ tend to the same material point and, as a consequence, $[\![p]\!]^h$ become a measure of the pressure discontinuity. Therefore, given the equivalence between Eqs. (3.16) and (2.40), the elements with high aspect ratio (HAR elements) provide the element for the space $\mathcal{V}^h$. As a consequence, the pressure field of the whole domain (*discontinuity band* Ω_Σ and porous domain $\Omega \setminus \Omega_\Sigma$) can be approximated via standard finite elements, as illustrated in fig. 3.1 where the discontinuity band is discretized with HAR elements.

Remark 5 *The fracture discontinuity* p_f *is not directly computed in the model. Instead, it is post-processed by* $p_f = (p^{(1)} - p^{(1')})/2$.

CHAPTER 4

MODELING HYDROMECHANICAL COUPLING ON FRACTURED POROUS MEDIA

Within the flow model for fractured porous media presented in chapter 2, this chapter goal is to extend the model to account the effects on geomechanical deformations, leading to a coupled system of hydromechanical equations. The geomechanical behavior of a saturated porous material arises by combining the linear momentum balance equation for the equilibrium of the mixture solid/fluid, the Biot effective stress principle, the constitutive relationship for solid phase relating effective stresses to strains, and the compatibility equation that links strains to displacements. The mass balance equation for the fluid is combined with Darcy's law to describe the flow behavior of the porous medium under the influence of the solid skeleton deformation. Within the fractures, the flow is influenced by fracture deformation through changes in the permeability and the storage capacity. Similarly, changes in fluid pressure result in changes in the effective stress distribution, leading to fracture's opening or closure. The propagation of the fracture will not be treated in this work.

4.1 MATEMATICAL AND PHYSICAL MODEL

This section presents the governing equations for the coupled fluid flow and solid skeleton deformation, for both the porous medium and the fractures.

4.1.1 POROUS MATRIX

The physical model for the deformable porous medium is based on the Lagrangean formulation of the poroelasticity theory, covered by Coussy (2004) and Coussy (2011). Denote $I = [0, T]$ the time interval and $\Omega \subset \mathbb{R}^d$, $d = 2$ or 3, the reservoir domain with piecewise smooth boundary Γ and outward normal **n**. Throughout this work the stress is defined as positive on tension. The main unknowns of the problem are the fluid pressure p and the solid phase displacement $\mathbf{u}$. The Lagrangian porosity is defined by (COUSSY, 2004; COUSSY, 2011):

$$\phi = \frac{dV_p}{dV_0}, \tag{4.1}$$

where V_0 and V_p denote the initial bulk volume and the current porous volume, respectively. The fluid mass balance equation reads:

$$\frac{\partial m_{fl}}{\partial t} + \nabla \cdot (\rho_{fl}\boldsymbol{v}) = \rho_f q, \tag{4.2}$$

where $m_{fl} = \rho_{fl}\phi$ is the Lagrangian fluid mass content, ρ_{fl} is the fluid density, $\boldsymbol{v}$ is the fluid Darcy's velocity and q is the volumetric source/sink term. For a slightly compressible fluid, mass density is governed by the constitutive relation:

$$\frac{1}{\rho_{fl}}\frac{\partial \rho_{fl}}{\partial t} = \frac{1}{\mathbb{K}_{fl}}\frac{\partial p}{\partial t}, \tag{4.3}$$

where $\mathbb{K}_{fl}$ is the fluid bulk modulus. The Lagrangian porosity ϕ relates to the fluid pressure and solid volumetric deformation according to (COUSSY, 2004):

$$\frac{\partial \phi}{\partial t} = \alpha\frac{\partial \varepsilon_v}{\partial t} + \frac{1}{N}\frac{\partial p}{\partial t}, \tag{4.4}$$

where $\varepsilon_v = \boldsymbol{\nabla} \cdot \mathbf{u}$, α is the Biot-Willis coefficient, and N is a poromechanical parameter. The parameters α and N are given by:

$$\alpha = 1 - \frac{\mathbb{K}}{\mathbb{K}_s}, \quad \frac{1}{N} = \frac{\alpha - \phi}{\mathbb{K}_s}. \tag{4.5}$$

where $\mathbb{K}$, and $\mathbb{K}_s$ are the matrix and solid grain bulk modulus, respectively. Using Eqs. (4.3) and (4.4), the variation on the Lagrangian fluid mass content reads:

$$\frac{\partial m_{fl}}{\partial t} = \rho_{fl}\alpha\frac{\partial \varepsilon_v}{\partial t} + \frac{\rho_{fl}}{M}\frac{\partial p}{\partial t}. \tag{4.6}$$

where M is the Biot modulus, given by:

$$\frac{1}{M} = \frac{\phi}{\mathbb{K}_{fl}} + \frac{1}{N}. \tag{4.7}$$

The fluid mass balance equation can be expressed in terms of fluid pressure p and solid displacement $\mathbf{u}$ by combining eq. (4.2) and (4.6) , yielding:

$$\frac{1}{M}\frac{\partial p}{\partial t} + \alpha\nabla \cdot \frac{\partial \mathbf{u}}{\partial t} + \nabla \cdot \boldsymbol{v} = q. \tag{4.8}$$

Neglecting gravitational effects, the fluid velocity is given by Darcy's law:

$$\boldsymbol{v} = -\frac{1}{\mu}\mathbf{K}\nabla p, \tag{4.9}$$

where μ is the fluid viscosity and $\mathbf{K}$ is the permeability tensor, which becomes a scalar K for isotropic media. Usually the permeability varies with the porosity, $\mathbf{K} = \mathbf{K}(\phi)$. A typical model for the permeability is proposed by (DAVID et al., 1994):

$$\mathbf{K} = \mathbf{K}_0 \left(\frac{\phi}{\phi_0}\right)^A, \tag{4.10}$$

where $\mathbf{K}_0$ is the permeability in the reference configuration and A is a property of the porous material.

The overall equilibrium of the solid-fluid mixture is given by:

$$\nabla \cdot \boldsymbol{\sigma}_T = \mathbf{0}, \tag{4.11}$$

where $\boldsymbol{\sigma}_T$ is the total stress tensor, which admits the Biot decomposition (BIOT, 1941; GEERTSMA et al., 1957; COUSSY, 2004; BORJA, 2006):

$$\boldsymbol{\sigma}_T = \boldsymbol{\sigma} - \alpha p \mathbf{1}, \tag{4.12}$$

where $\boldsymbol{\sigma}$ is the effective stress tensor of the porous skeleton, given by

$$\boldsymbol{\sigma} = \boldsymbol{\sigma}_0 + \boldsymbol{C} : \varepsilon, \tag{4.13}$$

where $\boldsymbol{\sigma}_0$ is the effective stress in the reference configuration, $\boldsymbol{C}$ is the porous material rank-4 elastic tensor and ε is the porous matrix small strain tensor, given by:

$$\varepsilon = \boldsymbol{\nabla}^s \mathbf{u} = \frac{1}{2}\left(\boldsymbol{\nabla}\mathbf{u} + \boldsymbol{\nabla}\mathbf{u}^T\right). \tag{4.14}$$

Assuming isotropic elastic porous material, the elastic tensor become:

$$\boldsymbol{C} = \lambda \mathbf{1} \otimes \mathbf{1} + 2\mu \mathbf{I}, \tag{4.15}$$

where $\mathbf{1}$ is the rank-2 identity tensor, $\mathbf{1}_{ij} = \delta_{ij}$, and $\mathbf{I}$ is the rank-4 symmetric unit tensor, $\mathbf{I}_{ijkl} = (\delta_{ik}\delta_{jl} + \delta_{il}\delta jk)/2$, and λ and μ are the Lamé's constant, which relates to the Young modulus E and the Poisson coefficient ν by:

$$\lambda = \frac{E\nu}{(1+\nu)(1-2\nu)}, \quad \mu = \frac{E}{2(1+\nu)}. \tag{4.16}$$

The model is completed by the boundary and initial conditions:

$$\begin{aligned}
&\mathbf{u}(\mathbf{x},t) = \mathbf{u}_D(t) && \text{on} \quad \Gamma_D^u \times I,\\
&\boldsymbol{\sigma}(\mathbf{x},t)\cdot\mathbf{n} = \mathbf{t}_N(t) && \text{on} \quad \Gamma_N^u \times I,\\
&p(\mathbf{x},t) = p_D(t) && \text{on} \quad \Gamma_D^p \times I,\\
&\boldsymbol{v}(\mathbf{x},t)\cdot\mathbf{n} = q_N(t) && \text{on} \quad \Gamma_N^p \times I,\\
&\mathbf{u}(\mathbf{x},0) = \mathbf{u}_0(\mathbf{x}) && \text{in} \quad \Omega,\ t=0,\\
&p(\mathbf{x},0) = p_0(\mathbf{x}) && \text{in} \quad \Omega,\ t=0,
\end{aligned} \tag{4.17}$$

where $\Gamma_D^u \cap \Gamma_N^u = \emptyset$, $\overline{\Gamma_D^u \cup \Gamma_N^u} = \Gamma$, $\Gamma_D^p \cap \Gamma_N^p = \emptyset$, $\overline{\Gamma_D^p \cup \Gamma_N^p} = \Gamma$, $\mathbf{u}_D$, $\mathbf{t}_N$, p_D and q_N are the prescribed boundary displacement, traction, pore pressure and flow rate, and $\mathbf{u}_0(\mathbf{x})$ and $p_0(\mathbf{x})$ are the initial conditions, respectively.

4.1.2 FRACTURES

Following the same methodology presented in chapter 2, the fracture is represented by the $(d-1)-$ dimensional hyperplane Σ, which divides the porous domain into two open disjoint subdomains Ω^+ and Ω^-, such that $\tilde{\Omega} = \Omega^- \cup \Sigma \cup \Omega^+$. The unit vectors $\boldsymbol{\nu}(\boldsymbol{s})$ and $\boldsymbol{\tau}(\boldsymbol{s})$ are the normal and tangential vectors to Σ at point $\boldsymbol{s}$, respectively. The outward unit normal to $\partial\Omega^+$ on Σ is then $\mathbf{n}^+ = -\boldsymbol{\nu}$ and the outward unit normal to $\partial\Omega^-$ on Σ is $\mathbf{n}^- = \boldsymbol{\nu}$.

In order to derive the set of governing equations posed on the fracture Σ, we define the cross-section mean values of the variables $\boldsymbol{v}_{f,\tau}$, $\boldsymbol{v}_{f,\nu}$, p_f and q_f similarly to Eqs. (2.10) to (2.13). The averaged mass conservation equation in Σ is obtained by integrating Eq. (4.8) over the fracture aperture w:

$$\frac{w}{M_f}\frac{\partial p_f}{\partial t} + \alpha_f \frac{\partial w}{\partial t} + \nabla_\tau \cdot (w\boldsymbol{v}_{f,\tau}) = wq_f - [\![\boldsymbol{v}\cdot\boldsymbol{\nu}]\!]. \tag{4.18}$$

Parameters α_f and M_f correspond to the Biot coefficient and Biot modulus on the fracture Σ, respectively. These parameters may depend on properties of the fracture microstructure, such as the roughness of fracture walls, the presence of infill material and the stress state. The experimental determination of reasonable values for these parameters is very difficult, but for unfilled fractures, it is reasonable to assume unitary Biot coefficient and Biot modulus equal to the inverse of the fluid bulk modulus (RUTQVIST; STEPHANSSON, 2003). Given these experimental limitation on parameters determination, this work will only address the case of high conductivity fractures with no infill material.

The averaged normal and tangential components of the Darcy's velocity over the fracture are given by:

$$\boldsymbol{v}_{f,\tau} = -\frac{1}{\mu}\mathrm{K}_{f,\tau}\boldsymbol{\nabla}_\tau p_f, \tag{4.19}$$

$$\boldsymbol{v}_{f,\nu} = -\frac{1}{\mu}\mathrm{K}_{f,\nu}\frac{[\![p]\!]}{w}, \tag{4.20}$$

where $\mathrm{K}_{f,\nu}$ and $\mathrm{K}_{f,\tau}$ are the transversal and longitudnal permeability. With the hypotheses that the longitudinal flow within the fracture relate to the pressure tangencial gradient according to the modified cubic law (WITHERSPOON et al., 1980):

$$\underbrace{\int_{-\frac{w}{2}}^{\frac{w}{2}} \boldsymbol{v}\left(s,t\right) \cdot \boldsymbol{\tau}\left(s\right)\ dt}_{w\boldsymbol{v}_{f,\tau}} = -\frac{w^3}{f12\mu}\boldsymbol{\nabla}_\tau \cdot p_f, \tag{4.21}$$

where $f \geq 1$ is a friction coefficient that accounts for the roughness of the fracture surface. The longitudinal permeability relates to the aperture according to:

$$\mathrm{K}_{f,\tau} = \frac{w^2}{12f}, \tag{4.22}$$

or it can be expressed in terms of the initial longitudinal permeability $\mathrm{K}_{f,\tau 0}$ and the initial aperture w_0:

$$K_{f,\tau} = K_{f,\tau 0}\left(\frac{w}{w_0}\right)^2. \tag{4.23}$$

As a consequence of the cubic law, the fracture longitudinal permeability depends strongly on the deformation of the fracture and its surroundings. Within the hypothesis of conductivity fractures with no infill material, $\mathrm{K}_{f,\nu} \rightarrow \infty$ and as a consequence the pressure is continuous across the fracture (see eqs. (2.33) and (2.34)).

While porous matrix mechanical behavior can be reasonably described by linear elasticity, the fracture mechanical behavior is generally non-linear. A mechanical model for the fracture must relate the changes in the stress on the surfaces of the fracture walls and their relative displacement, given by the jump on the displacement field across the fracture Σ, $[\![\mathbf{u}]\!]$. The normal component, $[\![u_\nu]\!] = [\![\mathbf{u} \cdot \boldsymbol{\nu}]\!]$, defines changes in the aperture w relative to the reference configuration w_0, $w = w_0 + [\![u_\nu]\!]$, while the tangential component $[\![u_\tau]\!] = [\![\mathbf{u} \cdot \boldsymbol{\tau}]\!]$ represents the length of the tangential displacement along the plane of the fracture. The case $[\![u_\nu]\!] = 0$ corresponds to a stress-free contact. For $[\![u_\nu]\!] < 0$, there is "penetration" due to deformation of the contact points, and $[\![u_\nu]\!] > 0$ represent the lose of physical contact.

The balance of traction across the fracture yields:

$$\boldsymbol{\sigma}_{T|\Sigma} \cdot \boldsymbol{\nu} = \mathbf{t}_f - \alpha_f p_f \boldsymbol{\nu}, \tag{4.24}$$

where $\mathbf{t}_f$ is the traction on the fracture surface, which is given by:

$$\mathbf{t}_f = \sigma_\nu \boldsymbol{\nu} + \sigma_\tau \boldsymbol{\tau}, \tag{4.25}$$

where σ_ν and σ_τ are, respectively, the fracture normal and shear stress due to the mechanical resistance of the contact points.

The constitutive relation between traction and displacement jump, $\mathbf{t}_f = \mathbf{t}_f([\![\mathbf{u}]\!])$, is generally nonlinear and is usually based on empirical measurements (BANDIS; LUMSDEN; BARTON, 1983; BARTON; BANDIS; BAKHTAR, 1985). Such relationship will be discussed in details on chapter 5.

4.2 STEADY STATE MODEL

In the sequel of this work the analysis will be restricted to steady state condition, obtained by disregarding variations in the Lagrangian fluid mass content m_{fl}. Gathering the previous equations, the resulting hydromechanical problem reads:

$$\nabla \cdot \boldsymbol{\sigma}_T = 0 \quad \text{on } \Omega \setminus \Sigma \times I, \tag{4.26}$$

$$\boldsymbol{\sigma}_T = \boldsymbol{\sigma}_0 + \boldsymbol{C} : \boldsymbol{\varepsilon} - \alpha p \mathbf{1} \quad \text{on } \Omega \setminus \Sigma \times I, \tag{4.27}$$

$$\boldsymbol{\sigma}_T \cdot \boldsymbol{\nu} = \mathbf{t}_f - \alpha_f p_f \boldsymbol{\nu} \quad \text{on } \Sigma \times I, \tag{4.28}$$

$$\nabla \cdot \boldsymbol{v} = q \quad \text{on } \Omega \setminus \Sigma \times I, \tag{4.29}$$

$$\boldsymbol{v} = -\frac{1}{\mu}\mathbf{K}\nabla p \quad \text{on } \Omega \setminus \Sigma \times I, \tag{4.30}$$

$$\nabla_\tau \cdot (w \boldsymbol{v}_{f,\tau}) = w q_f - [\![\boldsymbol{v} \cdot \boldsymbol{\nu}]\!] \quad \text{on } \Sigma \times I, \tag{4.31}$$

$$\boldsymbol{v}_{f,\tau} = -\frac{1}{\mu}\mathrm{K}_{f,\tau} \boldsymbol{\nabla}_\tau p_f \quad \text{on } \Sigma \times I, \tag{4.32}$$

$$p^+ = p_f = p^- \quad \text{on } \Sigma \times I, \tag{4.33}$$

with the boundary condition (4.17). Within the hypothesis of steady state conditions, geomechanics is affected by hydrodynamics solely by the gradient of pressure that acts to balance the effective stress, both in the the porous material and on the discontinuities. Conversely, geomechanics affects hydrodymanics by changes in the porous skeleton permeability due to volumetric deformations and discontinuities permeability by changes in the aperture.

4.3 REGULARIZED DISCONTINUOUS PRESSURE AND DISPLACEMENT FIELDS

The regularization strategy adopted to treat the pressure field p on chapter 2 will now be extended to the displacement field $\mathbf{u}$. Let $\Omega_\Sigma \subset \Omega$ be the *regulatization band* centered in Σ with width $h > 0$, $\Omega_\Sigma = \{\mathbf{s} + t\boldsymbol{\nu}; \mathbf{s} \in \Sigma,\ t \in [-\frac{h}{2}, \frac{h}{2}]\}$, such that:

$$p(\mathbf{x}, t) = \overline{p}(\mathbf{x}, t) + Z(\nu)[\![p]\!](\mathbf{x}, t), \tag{4.34}$$

$$\mathbf{u}(\mathbf{x}, t) = \overline{\mathbf{u}}(\mathbf{x}, t) + Z(\nu)[\![\mathbf{u}]\!](\mathbf{x}, t), \tag{4.35}$$

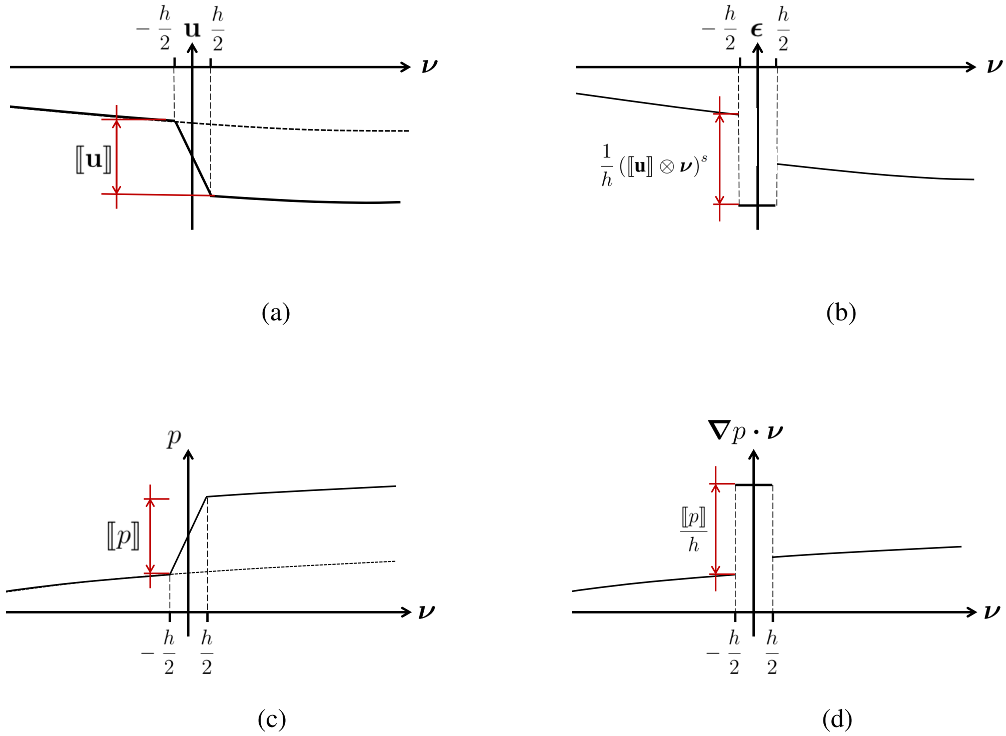

Figure 4.1: Regularized displacement and pressure fields and the respective strain and gradient fields.

where ν is the coordinate of the material point $\mathbf{x}$ according to the local coordinate system (τ, ν) along Σ, such that $\mathbf{x}(\tau, 0) = \Sigma$ and $Z(\nu)$ is the continuous *unit ramp function* given by Eq. (2.39).

The strain and the gradient of pressure can be obtained from Eqs. (4.35) and (4.34) by:

$$\boldsymbol{\varepsilon} = \nabla^s \mathbf{u} = \underbrace{\nabla^s \hat{\mathbf{u}}}_{\hat{\varepsilon}\text{ (regular)}} + \underbrace{\frac{\mu_{\Omega_\Sigma}(\nu)}{h}\left([\![\mathbf{u}]\!] \otimes \boldsymbol{\nu}\right)^s}_{\tilde{\varepsilon}\text{ (bounded)}}, \tag{4.36}$$

$$\nabla p = \underbrace{\nabla \hat{p}}_{\text{(regular)}} + \underbrace{\frac{\mu_{\Omega_\Sigma}(\nu)}{h}[\![p]\!]\boldsymbol{\nu}}_{\boldsymbol{\nabla}\tilde{p}\text{ (bounded)}} \tag{4.37}$$

where $\mu_{\Omega_\Sigma}(\nu)$ is the collocation function on Ω_Σ, ∇^s is the symmetric part of the gradient operator and $\hat{\varepsilon}$ and $\nabla\hat{p}$ are the continuous part of the strain and the gradient of pressure, while $\tilde{\boldsymbol{\varepsilon}}$ and $\boldsymbol{\nabla}\tilde{\boldsymbol{p}}$ are the discontinuous counterparts, which can be expressed according to the local (τ, ν) coordinate system as:

$$\tilde{\boldsymbol{\varepsilon}} = \begin{bmatrix} [\![\varepsilon_{\tau\tau}]\!] & [\![\varepsilon_{\tau\nu}]\!] \\ [\![\varepsilon_{\nu\tau}]\!] & [\![\varepsilon_{\nu\nu}]\!] \end{bmatrix} = \frac{1}{h}\begin{bmatrix} 0 & [\![u_\tau]\!]/2 \\ [\![u_\tau]\!]/2 & [\![u_\nu]\!] \end{bmatrix}, \tag{4.38}$$

$$\boldsymbol{\nabla}\tilde{\boldsymbol{p}} = \left\{ \begin{array}{c} [\![\nabla p_\tau]\!] \\ [\![\nabla p_\nu]\!] \end{array} \right\} = \frac{1}{h} \left\{ \begin{array}{c} 0 \\ [\![p]\!] \end{array} \right\}. \tag{4.39}$$

The stress tensor $\boldsymbol{\sigma}$ can be expressed in term of strains by:

$$\boldsymbol{\sigma} = \boldsymbol{C} : \left(\boldsymbol{\varepsilon} - \boldsymbol{\varepsilon}^{in}\right), \tag{4.40}$$

where $\boldsymbol{\varepsilon}^{in}$ correspond to the inelastic part of the strain. According to Eq. (4.36) the stresses within Ω_Σ become:

$$\boldsymbol{\sigma} = \boldsymbol{C} : \left(\hat{\boldsymbol{\varepsilon}} + \tilde{\boldsymbol{\varepsilon}} - \boldsymbol{\varepsilon}^{in}\right). \tag{4.41}$$

Following Manzoli et al. (2012), if a linearly elastic constitutive model is adopted, the inelastic strain must vanish. According to Eq. (4.41), in the limit when $h \to 0$, the stress component $\tilde{\boldsymbol{\varepsilon}}$ must also disappears in order to maintain the stress bounded, leading to $[\![\mathbf{u}]\!] \to \mathbf{0}$. Therefore, for small values of h, the term $1/h$ plays the role of a penalty parameter, enforcing continuity of the displacement field along Σ.

For nonlinear constitutive models, on the other hand, when h tends to zero the stresses given by Eq. (4.41) can only be bounded if the strain component $\tilde{\boldsymbol{\varepsilon}}$ vanishes with the inelastic strain $\boldsymbol{\varepsilon}^{in}$ so their difference remain bounded, i.e. $\boldsymbol{\varepsilon}^{in} \to \tilde{\boldsymbol{\varepsilon}}$ when $h \to 0$. Hence, for small values of h, the strain regular part $\hat{\boldsymbol{\varepsilon}}$ becomes negligible in comparison to $\tilde{\boldsymbol{\varepsilon}}$ and the displacement jump $[\![\boldsymbol{u}]\!]$ can be approximated by the strain $\boldsymbol{\varepsilon}$, according to the local (τ, ν) reference frame, by $[\![u_\nu]\!] \approx h\varepsilon_{\nu\nu}$ and $[\![u_\tau]\!] \approx h\varepsilon_{\tau\nu}$.

4.3.1 Modeling the effects of the discontinuity on the coupled hydromechanical problem

Following a similar approach to Manzoli et al. (2019), the effects of the fracture Σ are accounted on Ω_Σ by incorporating convenient properties into the mass conservation equation, the linear momentum balance equation the effective stress tensor constitutive equation and Darcy's law, such that:

$$\tilde{\mathbf{K}}(\mathbf{x}) = \begin{cases} \mathbf{K}_m, & \text{for } \mathbf{x} \in \Omega \setminus \Omega_\Sigma, \\ \dfrac{h\mathrm{K}_{f,\nu}}{w}\boldsymbol{\nu} \otimes \boldsymbol{\nu} + \dfrac{w\mathrm{K}_{f,\tau}}{h}\boldsymbol{\tau} \otimes \boldsymbol{\tau}, & \text{for } \mathbf{x} \in \Omega_\Sigma, \end{cases} \tag{4.42}$$

$$\tilde{q}(\mathbf{x}) = \begin{cases} q, & \text{for } \mathbf{x} \in \Omega \setminus \Omega_\Sigma, \\ \dfrac{wq_f}{h}, & \text{for } \mathbf{x} \in \Omega_\Sigma, \end{cases} \tag{4.43}$$

$$\tilde{\boldsymbol{\sigma}}(\boldsymbol{\varepsilon}) = \begin{cases} \boldsymbol{C} : \boldsymbol{\varepsilon}, & \text{for } \mathbf{x} \in \Omega \setminus \Omega_\Sigma, \\ \boldsymbol{\sigma}_{\Omega_\Sigma}(\boldsymbol{\varepsilon}), & \text{for } \mathbf{x} \in \Omega_\Sigma, \end{cases} \tag{4.44}$$

$$\tilde{\alpha} = \begin{cases} \alpha, & \text{for } \mathbf{x} \in \Omega \setminus \Omega_\Sigma, \\ 1, & \text{for } \mathbf{x} \in \Omega_\Sigma, \end{cases} \tag{4.45}$$

where $\boldsymbol{\sigma}_{\Omega_\Sigma}(\boldsymbol{\varepsilon})$ is an appropriate constitutive relation on Ω_Σ, such that $\boldsymbol{\sigma}_{\Omega_\Sigma}(\boldsymbol{\varepsilon}) \cdot \boldsymbol{\nu} \to \mathbf{t}_f$ when $h \to 0$. Such relation will be developed in details in the following chapter.

The complete summary of the governing equations is given by:

$$\nabla \cdot \tilde{\boldsymbol{\sigma}}_T = \mathbf{0} \quad \text{on} \quad \Omega \times I, \tag{4.46}$$

$$\boldsymbol{\sigma}_T = \boldsymbol{\sigma}_0 + \tilde{\boldsymbol{\sigma}}(\boldsymbol{\varepsilon}) - \tilde{\alpha} p \quad \text{on} \quad \Omega \times I, \tag{4.47}$$

$$\nabla \cdot \tilde{\boldsymbol{v}} = \tilde{q} \quad \text{on} \quad \Omega \times I, \tag{4.48}$$

$$\tilde{\boldsymbol{v}} = -\frac{1}{\mu} \tilde{\mathbf{K}} \left(\nabla p \right) \quad \text{on} \quad \Omega \times I, \tag{4.49}$$

with the boundary condition (4.17).

CHAPTER 5

FRACTURE CONSTITUTIVE MODEL

The main approaches employed to quantitatively describe the mechanical behavior of rock fractures are the theoretical approach, which adopts known theories, like plasticity and contact theory, to simulate the observed behavior, and the empirical approach, in which measured physical data are analyzed to derive correlations between variables of influence and models are formulated according to observed behavior. Among several empirical and theoretical constitutive models describing fracture's mechanical behavior, the Barton-Bandis empirical model (BARTON, 1973; BARTON; CHOUBEY, 1977; BANDIS; LUMSDEN; BARTON, 1983; BARTON; BANDIS; BAKHTAR, 1985) has been widely used because it is simple to apply and includes several important behaviors, such as prediction of fracture closure due to normal stress compression, prediction of peak shear strength and peak shear displacement of non-planar rock fractures, roughness degradation, pre and post-peak shear strength, and the dilatancy prediction of fractures subjected to direct shear loading.

5.1 BARTON-BANDIS EMPIRICAL MODEL

This section presents the main features of the Barton-Bandis fracture model: the normal stress-normal displacement relationship, the shear stress-shear displacement relationship, and the shear-induced dilation.

5.1.1 FRACTURE NORMAL DEFORMATION

Based on experimental laboratory works, rock fractures exhibit nonlinear relation between compressive normal stress and normal displacement. Let σ_ν denote the normal compressive stress and $[\![u_{\nu,c}]\!]$ denote the part of the normal displacement due to compression. According to Bandis, Lumsden e Barton (1983), σ_ν relates to $[\![u_{\nu,c}]\!]$ by the hyperbolic law, given by (see Fig. 5.1):

$$\sigma_\nu([\![u_{\nu,c}]\!]) = \frac{k_{ni}V_m}{V_m + [\![u_{\nu,c}]\!]}[\![u_{\nu,c}]\!], \tag{5.1}$$

where k_{ni} is the normal stiffness on the reference configuration and V_m is the maximum al-

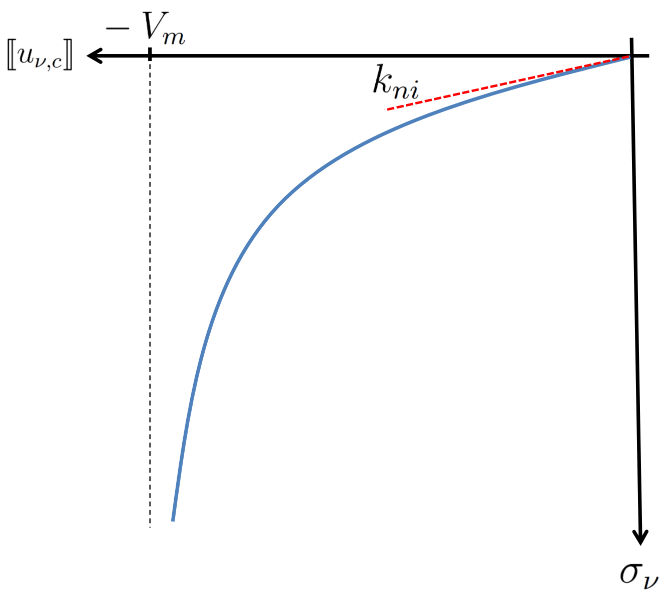

Figure 5.1: Normal stress vs normal displacement give by the Barton-Bandis hyperbolic law.

lowable closure. Recalling the tension positive stress convention, $\sigma_\nu < 0$ on compression and $[\![u_{\nu,c}]\!] < 0$ on closure, therefore the parameter V_m is positive. The hyperbolic law describes how the fracture stiffness increase with fracture closure, due to the progressive increase of contact points between the fracture opposite walls, as illustrated on Fig. 5.2

Equation (5.1) can be rearranged to provide the fracture closure as a function of the normal normal stress:

$$[\![u_{\nu,c}]\!](\sigma_\nu) = \frac{\sigma_\nu V_m}{k_{ni} V_m - \sigma_\nu}. \tag{5.2}$$

The maximum closure V_m is usually less than or equal to the fracture aperture in the reference configuration, w_0, providing an upper bound to fracture closure, $-[\![u_{\nu,c}]\!] < V_m \leq w_0$ (the equality holds only with the hypothesis of perfectly matched fractures). In fact, taking the limit when $\sigma_\nu \to -\infty$ on Eq.(5.2):

$$[\![u_{\nu,c}]\!](\sigma_\nu \to -\infty) = -V_m. \tag{5.3}$$

5.1.2 Fracture shear deformation

Direct shear experiments shows that the shear stress-displacement curve of the rock fractures presents two distinct stages, the pre-peak stage and the post-peak, as shown on Fig. 5.3. The shearing event can be summarized by the following order of events:

1. During the pre-peak stage, shear increases by first mobilizing friction.

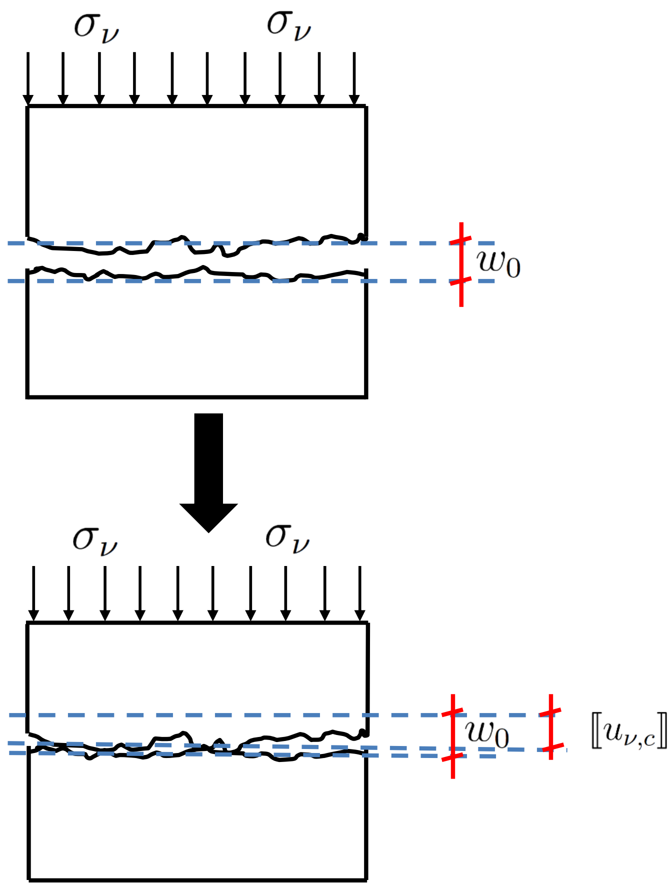

Figure 5.2: Fracture closure process due to normal compression.

2. When the shear displacement $[\![u_\tau]\!]$ reaches about 30% of the peak shear displacement $[\![u_{\tau,peak}]\!]$, roughness mobilization starts and dilation begins. Shear stress increases until the peak shear stress is reached.

3. Peak strength is reached when $[\![u_\tau]\!] = [\![u_{\tau,peak}]\!]$.

4. After this point, post-peak stage begins as roughness is gradually destroyed or worn down and shear decreases to a residual value, while dilation continues at a reduce rate due to roughness reduction.

5. Residual strength is finally reached

The parameters required for a complete characterization of the fracture are: the fracture roughness coefficient JRC, the fracture compressive strength JCS and the fracture residual friction angle ϕ_r. The first parameter, JRC, is a dimensionless number varying from 0 (smooth fracture) to 20 (roughest possible fracture without actual steps). The second parameter JCS, depends on the weathering grade of the fracture walls and varies up to the value of the unconfined compression strength of the unweathered rock σ_c, but reduces to about $\sigma_c/4$ for weathered fractures. The friction angle ϕ_r usually ranges from $25°$ to $35°$ (BARTON, 1973; BARTON; CHOUBEY, 1977).

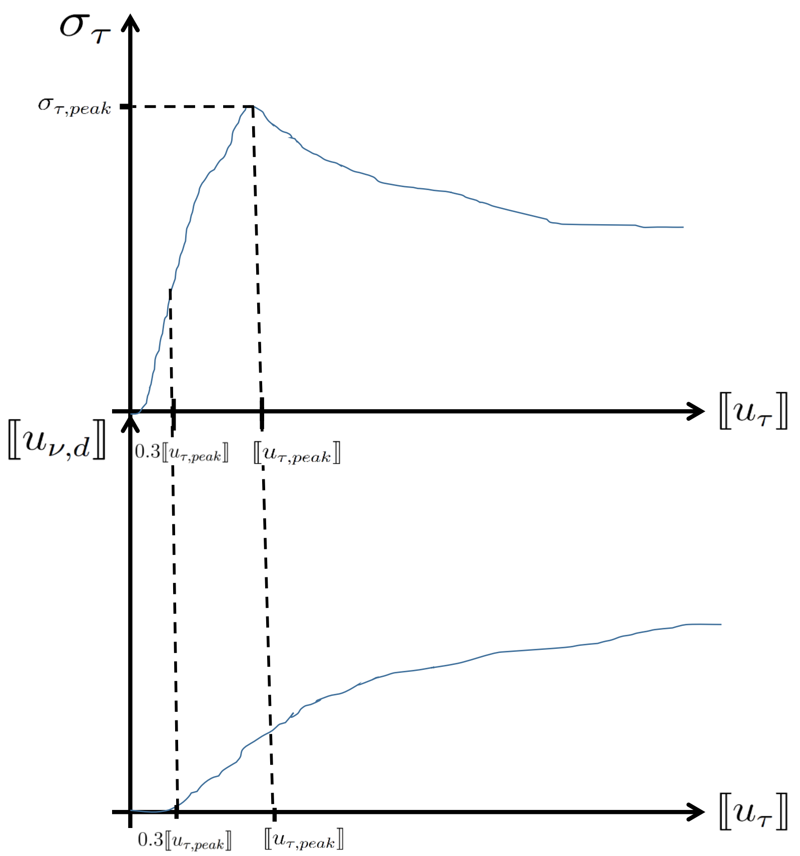

Figure 5.3: Shear stress vs shear displacement curve and dilation vs shear dislpacement curve

Barton (1973) suggested a empirical law for the peak shear strength, given by:

$$\sigma_{\tau,peak} = |\sigma_\nu| \cdot \tan\left(JRC \cdot \log_{10}\left(\frac{JCS}{|\sigma_\nu|}\right) + \phi_r\right). \tag{5.4}$$

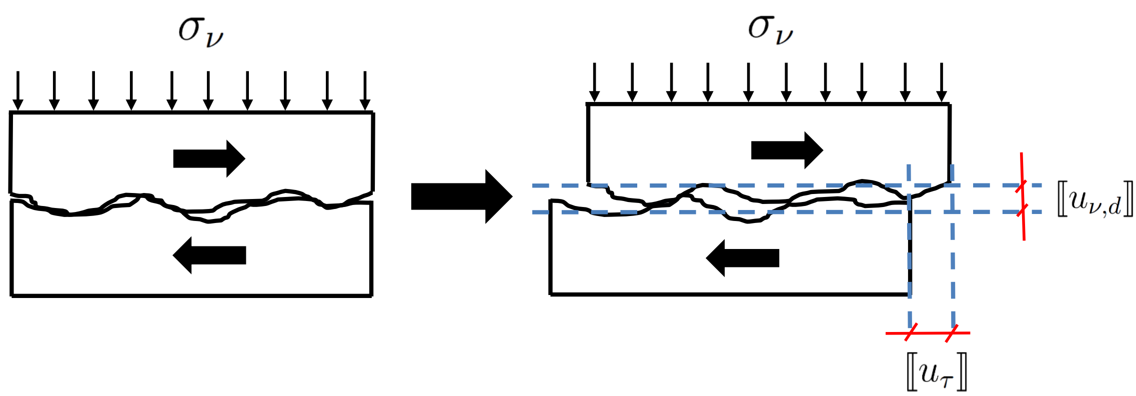

Figure 5.4: Fracture shearing process with dilation.

According to Barton (1982), Barton, Bandis e Bakhtar (1985) the current shear stress σ_τ may be obtained by using shear displacement dependent JRC values, the mobilized value JRC_{mob}, in Eq. (5.4):

$$\sigma_\tau = |\sigma_\nu| \cdot \tan \underbrace{\left(JRC_{\text{mob}} \cdot \log_{10}\left(\frac{JCS}{|\sigma_\nu|}\right) + \phi_r \right)}_{\phi_{mob}} = |\sigma_\nu| \cdot \tan\left(\phi_{mob}\right). \tag{5.5}$$

where JRC_{mob} can be calculated using the dimensionless model showed in table 5.1, in which $[\![u_\tau]\!]$ is the current shear displacement and $[\![u_{\tau,peak}]\!]$ is the peak shear displacement, and ϕ_{mob} is mobilized friction angle.

Table 5.1: Dimensionless model for sheas stress-strain calculation (BARTON, 1982).

$[\![u_\tau]\!]/[\![u_{\tau,peak}]\!]$	JRC_{mob}/JRC
0.0	$-\phi_r/\left[JRC \cdot \log_{10}\left(JCS/\lvert\sigma_\nu\rvert\right)\right]$
0.3	0.0
0.6	0.75
1.0	10
2.0	0.85
4.0	0.70
10.0	0.50
25.0	0.40
100.0	0.0

According to Barton e Choubey (1977), Bandis, Lumsden e Barton (1981), the fracture parameters JRC and JCS are scale-dependent, i.e. their values in field scale, denoted JRC_n and JCS_n, can be estimated from the values obtained from laboratory samples, by using (BARTON; BANDIS; BAKHTAR, 1985):

$$JRC_n = JRC_0 \left(\frac{L_n}{L_0}\right)^{-0.02 JRC_0}, \tag{5.6}$$

$$JCS_n = JCS_0 \left(\frac{L_n}{L_0}\right)^{-0.03 JRC_0}, \tag{5.7}$$

where L_n is the effective fracture length (i.e. size of a block edge between fracture intersections), and JRC_0 and JCS_0 are values measured on the laboratory samples with length L_0. Here, the subscript 0 denotes laboratory scale instead of reference configuration. The scale dependency of peak shear displacement $[\![u_{\tau,peak}]\!]$ is given by (BARTON, 1982; BARTON; BANDIS; BAKHTAR, 1985):

$$[\![u_{\tau,peak}]\!] = \frac{L_n}{500}\left(\frac{JRC_n}{L_n}\right)^{0.33}. \tag{5.8}$$

5.1.3 FRACTURE SHEAR DILATION

Denote $[\![u_{\nu,d}]\!]$ the fracture dilation, i.e. positive normal displacement (fracture aperture) induced by shearing. According to Olsson e Barton (2001), dilation begins when $[\![u_\tau]\!] = 0.3[\![u_{\tau,peak}]\!]$ and follows the incremental rule:

$$d[\![u_{\nu,d}]\!] = \tan(d_{mob})d[\![u_{\tau,peak}]\!], \tag{5.9}$$

where d_{mob} is the dilation angle, given by:

$$d_{mob} = \begin{cases} 0, & [\![u_\tau]\!] < 0.3[\![u_{\tau,peak}]\!], \\ \dfrac{1}{2}JRC_{mob} \cdot \log_{10}\left(\dfrac{JCS_n}{|\sigma_n|}\right), & [\![u_\tau]\!] \geq 0.3[\![u_{\tau,peak}]\!]. \end{cases} \tag{5.10}$$

Integrating Eq. (5.9), the fracture dilation reads:

$$[\![u_{\nu,d}]\!] = \int_0^{[\![u_\tau]\!]} \tan\left(d_{mob}(u)\right)\, du. \tag{5.11}$$

5.1.4 COUPLED NORMAL AND SHEAR BEHAVIOR

Fractures under changing stress conditions may experience a combination of shearing and variable normal stress. According to Saeb e Amadei (1992), Gens, Carol e Alonso (1990), the fracture normal displacement $[\![u_\nu]\!]$ is given by the sum of the normal displacement part due to compression, $[\![u_{\nu,c}]\!]$ (Eq. 5.2), and the normal displacement part due to shear dilation $[\![u_{\nu,d}]\!]$ (Eq. 5.11):

$$[\![u_\nu]\!] = [\![u_{\nu,d}]\!] + \frac{V_m \sigma_\nu}{k_{ni}V_m - \sigma_\nu}, \tag{5.12}$$

or, after rearranging the above equation:

$$\sigma_\nu = \frac{k_{ni}V_m\left([\![u_\nu]\!] - [\![u_{\nu,d}]\!]\right)}{V_m + \left([\![u_\nu]\!] - [\![u_{\nu,d}]\!]\right)}. \tag{5.13}$$

5.2 FACTURE CONTINUUM CONSTITUTIVE MODEL

To reproduce the nonlinear mechanical behavior of the fracture Σ described by the Barton-Bandis model, i.e. Eqs. (5.13), (5.5) and (5.11), we introduce a continuum (stress-strain) constitutive model placed on the *regularization band* Ω_Σ. The constitutive model is based on a damage criteria in terms of the shear component of the stress tensor and a contact criteria in terms of the normal component of the stress tensor. Since the fracture introduces mechanical orthotropy on the domain, the model is posed in terms of the local coordinate system (τ, ν)

along Σ. The damage criteria is given by:

$$\Phi\left(r\right)=\parallel\sigma_{\tau}\parallel-q\left(r\right), \tag{5.14}$$

where q and r are stress-like and strain-like internal variables. The damage and the contact model are expressed in terms of the elastic effective stress tensor $\overline{\boldsymbol{\sigma}}=\boldsymbol{C}:\boldsymbol{\varepsilon}$, (i.e., the stresses related to the intact, undamaged porous material) and $\boldsymbol{C}$ is the isotropic rank-4 elastic tensor. For sake of simplicity, we assume that the Young Modulus E on Ω_{Σ} is the same of the surrounding porous media and the Poisson coefficient is null, $\nu=0$.

Recalling that for very small values of the band width h, the regular component $\hat{\boldsymbol{\varepsilon}}$ can be disregarded in comparison with the unbounded part $\tilde{\boldsymbol{\varepsilon}}$, thus the displacement jump relates to strain according to (see section 4.3):

$$[\![u_{\nu}]\!]\approx h\varepsilon_{\nu\nu}, \qquad [\![u_{\tau}]\!]\approx 2h\varepsilon_{\tau\nu}. \tag{5.15}$$

In order to account for dilation effects, we introduce a strain-like variable $\varepsilon^{d}_{\nu\nu}$ related to the dilational part of the normal displacement, such that $[\![u_{\nu,d}]\!]=h\varepsilon^{d}_{\nu\nu}$. The elastic effective stress tensor $\overline{\boldsymbol{\sigma}}_{\Omega_{\Sigma}}$ on the *regularization band* Ω_{Σ} is defined as:

$$\overline{\boldsymbol{\sigma}}_{\Omega_{\Sigma}}=\begin{bmatrix}\overline{\sigma}_{\tau\tau} & \overline{\sigma}_{\tau\nu}\\ \overline{\sigma}_{\nu\tau} & \overline{\sigma}_{\nu\nu}\end{bmatrix}=\underbrace{\boldsymbol{C}:\begin{bmatrix}0 & 0\\ 0 & \varepsilon_{\nu\nu}-\varepsilon^{d}_{\nu\nu}\end{bmatrix}}_{\overline{\boldsymbol{\sigma}}_{\nu}}+\underbrace{\boldsymbol{C}:\begin{bmatrix}\varepsilon_{\tau\tau} & \varepsilon_{\tau\nu}\\ \varepsilon_{\nu\tau} & 0\end{bmatrix}}_{\overline{\boldsymbol{\sigma}}_{\tau}}. \tag{5.16}$$

The stress tensor $\boldsymbol{\sigma}_{\Omega_{\Sigma}}$ is given in terms of the elastic effective stress tensor $\overline{\boldsymbol{\sigma}}_{\Omega_{\Sigma}}$ by:

$$\boldsymbol{\sigma}_{\Omega_{\Sigma}}=\xi\overline{\boldsymbol{\sigma}}_{\nu}+(1-d)\overline{\boldsymbol{\sigma}}_{\tau}, \tag{5.17}$$

where $d\in[0,1]$ is the scalar damage variable and $\xi\in[0,1]$ is a contact variable. Dividing Eq. (5.14) by $(1-d)$, the damage criteria can be expressed in terms of $\overline{\boldsymbol{\sigma}}_{\Omega_{\Sigma}}$ by:

$$\overline{\Phi}(r)=\parallel\overline{\boldsymbol{\sigma}}_{\tau}\parallel-r, \tag{5.18}$$

with $r=q/(1-d)$, which leads to the damage evolution rule in terms of r:

$$d(r)=1-\frac{q}{r}. \tag{5.19}$$

The constitutive model for the shear is completed by the Kuhn-Tucker loading–unloading conditions:

$$\overline{\Phi}\leq 0, \qquad \dot{r}\geq 0, \qquad \dot{r}\overline{\Phi}=0, \tag{5.20}$$

and the consistency condition:

$$\dot{r}\dot{\overline{\Phi}}=0 \text{ if } \overline{\Phi}=0, \tag{5.21}$$

which, together with Eq. (5.18), lead to the following explicit evolution law for the strain-like internal variable r:

$$r = \max_{s\in[0,t]} \left[\parallel \overline{\boldsymbol{\sigma}}_{\tau}(s) \parallel, 0\right]. \tag{5.22}$$

where t is the pseudo-time associated with the loading process. According to Eq. (5.22), the variable r assumes the maximum value reached by the norm of the shear component of the elastic effective stress during the loading process. Therefore, the evolution of the shear stress is driven by the elastic effective stresses, so that the stresses can be obtained from the strains in a closed form. This constitutes the main advantage of this model, since iterative methods are not required at the constitutive model level.

The contact variable is given, at any instant t, in terms of the elastic effective stress $\boldsymbol{\sigma}_{\Omega_\Sigma}$ by:

$$\xi(\boldsymbol{\sigma}_{\Omega_\Sigma}(t)) = \frac{k_{ni}V_m}{\dfrac{V_m E}{h} - \parallel \overline{\boldsymbol{\sigma}}_{\nu}(t) \parallel}. \tag{5.23}$$

In the limit when h tends to zero, the continuum (stress-strain) constitutive relation given by Eq. (5.17) tends to the discrete (stress-displacement) relation between the shear stress and the longitudinal displacement given by:

$$\sigma_{\tau\nu} = G\frac{(1-d)}{h}[\![u_\tau]\!], \tag{5.24}$$

where G is the shear modulus associated to $\boldsymbol{C}$. Therefore, for a monotonically increasing displacement, the equation of the discrete model become:

$$r = \frac{G}{h}[\![u_\tau]\!], \tag{5.25}$$

$$d = 1 - \frac{q\left(\frac{G}{h}[\![u_\tau]\!]\right)}{\frac{G}{h}[\![u_\tau]\!]}, \tag{5.26}$$

$$\sigma_{\tau\nu} = G\frac{(1-d)}{h}[\![u_\tau]\!] = q\left(\frac{G}{h}[\![u_\tau]\!]\right). \tag{5.27}$$

In view of Eqs. (5.25) and (5.5), the stress-like variable is given by:

$$q(r) = \parallel \boldsymbol{\sigma}_{\nu} \parallel \cdot \tan\left(\phi_{mob}\left(\frac{hr}{G}\right)\right), \tag{5.28}$$

while the strain variable $\varepsilon^d_{\nu\nu}$ is given in terms of r, according to Eq. (5.11), by:

$$\varepsilon^d_{\nu\nu} = \frac{1}{h}\int_0^{\frac{rh}{G}} \tan\left(d_{mob}(u)\right)\, du. \tag{5.29}$$

Analogously, the relation between normal stress and normal component of the displacement jump is given by:

$$\sigma_{\nu\nu} = \frac{E\xi}{h}\left(\llbracket u_\nu \rrbracket - \llbracket u_{\nu,d} \rrbracket\right) = \frac{k_{ni} V_m E \left(\dfrac{\llbracket u_\nu \rrbracket - \llbracket u_{\nu,d} \rrbracket}{h} \right)}{\dfrac{V_m E}{h} - \dfrac{E\left(\llbracket u_\nu \rrbracket - \llbracket u_{\nu,d} \rrbracket\right)}{h}} = \frac{k_{ni} V_m \left(\llbracket u_\nu \rrbracket - \llbracket u_{\nu,d} \rrbracket\right)}{V_m + \left(\llbracket u_\nu \rrbracket - \llbracket u_{\nu,d} \rrbracket\right)}, \quad (5.30)$$

which correspond to Eq. (5.13). Therefore, the discrete constitutive model given by the Barton-Bandis empirical model emerges from the continuum model when h tends to zero:

$$\boldsymbol{\sigma}_{\Omega_\Sigma} \cdot \boldsymbol{\nu} = \left\{ \begin{array}{c} \sigma_{\tau\nu} \\ \sigma_{\nu\nu} \end{array} \right\} \rightarrow \mathbf{t}_f \quad \text{when} \quad h \rightarrow 0. \quad (5.31)$$

Table 5.2 summarizes the equations of the fracture continuum constitutive model.

Table 5.2: Equations of the fracture continuum constitutive model

Constitutive relation	$\boldsymbol{\sigma}_{\Omega_\Sigma} = \xi \overline{\boldsymbol{\sigma}}_\nu + (1-d)\overline{\boldsymbol{\sigma}}_\tau$
Effective stress	$\overline{\boldsymbol{\sigma}}_{\Omega_\Sigma} = \boldsymbol{C} : \left(\boldsymbol{\varepsilon} - \boldsymbol{\varepsilon}^d\right) = \overline{\boldsymbol{\sigma}}_\nu + \overline{\boldsymbol{\sigma}}_\tau$
Damage criterion	$\overline{\Phi}(r) = \parallel \overline{\boldsymbol{\sigma}}_\tau \parallel - r$
Evolution law for the strain-like variable	$r = \max\limits_{s \in [0,t]} \left[\parallel \overline{\boldsymbol{\sigma}}_\tau(s) \parallel, 0\right]$
Damage evolution	$d(r) = 1 - \frac{q(r)}{r}$
Contact evolution	$\xi(\overline{\boldsymbol{\sigma}}_\nu) = \dfrac{k_{ni} V_m}{\frac{V_m E}{h} - \parallel \overline{\boldsymbol{\sigma}}_\nu \parallel}$
Stress-like variable evolution	$q(r) = \parallel \boldsymbol{\sigma}_\nu \parallel \cdot \tan\left(\phi_{mob}\left(\frac{hr}{G}\right)\right)$
Dilation variable evolution	$\varepsilon^d_{\nu\nu}(r) = \dfrac{1}{h}\displaystyle\int_0^{\frac{rh}{G}} \tan\left(d_{mob}(u)\right)\, du$

5.2.1 Implicit-explicit integration scheme

In order to avoid numerical convergence problems related to the nonlinear constitutive model, and implicit-explicit (IMPL-EX) integration algorithm proposed by Oliver et al. (2006), Oliver, Huespe e Cante (2008) is used to integrate the mechanical stress-strain relations, instead of using a implicit integration scheme (as classical backward-Euler implicit algorithm). This algorithm combines implicit and explicit integration schemes, exploiting the robustness of explicit integration schemes and the stability of implicit schemes.

The fracture continuum constitutive model is slightly rephrased to become suitable to the IMPL-EX algorithm, by introducing a dummy internal variable $\alpha = \epsilon - \epsilon^d_{\nu\nu}$ in the contact model. The IMPL-EX algorithm is basically an implicit backward-Euler integration scheme where, at each time step, the damage and the contact variables, d and ξ, are computed with an explicit linear extrapolation on the internal variables, $\tilde{r}$ and $\tilde{\alpha}$, instead of their real value, r and α. The extrapolated variables remain constant at each time step, and the algorithmic tangent constitutive tensor remains constant at each time step, thus the Newton-Raphson procedure should converge in an unique iteration per time step (OLIVER; HUESPE; CANTE, 2008). As a consequence, there is an error associated with the use of this alternative integration scheme, since it may violate the consistency condition. The error can be controlled by decreasing the time step length, as can be seen in the numerous examples performed by Oliver, Huespe e Cante (2008). The IMPL-EX algorithm has been widely tested for the integration of constitutive models based on damage mechanics (OLIVER et al., 2006; OLIVER; HUESPE; CANTE, 2008; MANZOLI et al., 2012).

The IMPL-EX scheme allow further simplifications that considerably reduce the of the problem: at time step $n+1$ the shear stress $\sigma_{\tau\nu_{(n+1)}}$ is calculated using the normal stress from the previous time step $\sigma_{\nu\nu_{(n)}}$, which is constant at the current time step, making the damage model uncoupled from the contact model. Similarly, using the dilation strain from the previous time step, $\epsilon^d_{\nu\nu_{(n)}}$, in the contact model makes it uncoupled from the damage model. Table 5.3 summarizes the main stages associated with the update of the stresses at the time step $t_{(n+1)}$ using the fracture continuum constitutive model with the IMPL-EX method.

Table 5.3: IMPL-EX integration scheme for the fracture constitutive model.

INPUT: $\boldsymbol{\varepsilon}_{(n+1)}$, $\boldsymbol{\sigma}_{\nu_{(n)}}$, $\boldsymbol{\varepsilon}^d_{(n)}$, $\alpha_{(n)}$, $\Delta\alpha_{(n)}$, $r_{(n)}$, $\Delta r_{(n)}$

(i) Transform the current strain tensor according to the local coordinate system (τ, ν)

(ii) Compute the elastic stress tensor

$$\overline{\boldsymbol{\sigma}}_{(n+1)} = \boldsymbol{C} : \left(\boldsymbol{\varepsilon} - \boldsymbol{\varepsilon}^d\right)$$

(iii) Check for loading-unloading condition

IF $\| \overline{\boldsymbol{\sigma}}_{\tau_{(n+1)}} \| - r_{(n)} \leq 0$, THEN

$r_{(n+1)} := r_{(n)}$

ELSE

$r_{(n+1)} := \| \overline{\boldsymbol{\sigma}}_{\tau_{(n+1)}} \|$

END IF

(iv) Compute the strain-like internal variable increment

$$\Delta r_{(n+1)} := r_{(n+1)} - r_{(n)}$$

(v) Compute the explicit extrapolation of the strain-like internal variable

$$\tilde{r}_{(n+1)} := r_{(n)} + \frac{\Delta t_{(n+1)}}{\Delta t_{(n)}} \Delta r_{(n)}$$

(vi) Compute the dummy internal variable increment

$$\alpha_{(n+1)} := \varepsilon_{\nu\nu_{(n+1)}} + \varepsilon^d_{\nu\nu_{(n)}}; \qquad \Delta\alpha_{(n+1)} := \alpha_{(n+1)} - \alpha_{(n)}$$

(vii) Compute the explicit extrapolation of the dummy internal variable

$$\tilde{\alpha}_{(n+1)} := \alpha_{(n)} + \frac{\Delta t_{(n+1)}}{\Delta t_{(n)}} \Delta\alpha_{(n)}$$

(viii) Update damage and contact variables

$$\tilde{d}_{(n+1)} := 1 - \frac{q(\tilde{r}_{(n+1)})}{\tilde{r}_{(n+1)}}; \quad q(\tilde{r}_{(n+1)}) := \| \boldsymbol{\sigma}_{\nu_{(n)}} \| \cdot \tan\left(\phi_{mob}\left(\frac{h\tilde{r}_{(n+1)}}{G}\right)\right);$$

$$\tilde{\xi}_{(n+1)} := \xi\left(\tilde{\alpha}_{(n+1)}\right)$$

(ix) Compute the stress tensor according to Eq. (5.17)

$$\boldsymbol{\sigma}_{(n+1)} := \tilde{\xi}_{(n+1)} \overline{\boldsymbol{\sigma}}_{\nu_{(n+1)}} + (1 - \tilde{d}_{(n+1)}) \overline{\boldsymbol{\sigma}}_{\tau_{(n+1)}}$$

(x) Update the dilation variable

$$\varepsilon^d_{\nu\nu_{(n+1)}} := \frac{1}{h} \int_0^{\frac{h\tilde{r}_{(n+1)}}{G}} \tan\left(d_{mob}(u)\right) \, du$$

(xi) Rotate the stress tensor to obtain its components according to the global coordinate system

OUTPUT: $\boldsymbol{\sigma}_{(n+1)}, \ \boldsymbol{\sigma}_{\nu_{(n+1)}}, \ \varepsilon^d_{\nu\nu_{(n+1)}}, \ r_{(n+1)}, \ \Delta r_{(n+1)}, \ \alpha_{(n+1)}, \ \Delta\alpha_{(n+1)}$

CHAPTER 6

FINITE ELEMENT SCHEME FOR THE HYDROMECHANICAL PROBLEM

6.1 WEAK FORM OF THE GOVERNING EQUATIONS

Define the solution function spaces for the fluid pressure and displacement, satisfying the essential boundary conditions,

$$\mathcal{V} = \left\{ \eta = \overline{\eta} + Z_{\Omega_\Sigma}(\nu)[\![\eta]\!] \mid \overline{\eta},\ [\![\eta]\!] \in \mathcal{H}^1(\Omega), \eta = p_D \text{ on } \Gamma_D^p \right\}, \tag{6.1}$$

$$\mathcal{U} = \left\{ \mathbf{w} = \overline{\mathbf{w}} + Z_{\Omega_\Sigma}(\nu)[\![\mathbf{w}]\!] \mid \overline{\mathbf{w}}, [\![\mathbf{w}]\!] \in (H^1(\Omega))^d, \mathbf{w} = \mathbf{u}_D \text{ on } \Gamma_D^u \right\}, \tag{6.2}$$

and the corresponding test function spaces, satisfying the homogeneous counterpart of the essential boundary conditions,

$$\mathcal{V}_0 = \left\{ \eta = \overline{\eta} + Z_{\Omega_\Sigma}(\nu)[\![\eta]\!] \mid \overline{\eta},\ [\![\eta]\!] \in \mathcal{H}^1(\Omega), \eta = 0 \text{ on } \Gamma_D^p \right\}, \tag{6.3}$$

$$\mathcal{U}_0 = \left\{ \mathbf{w} = \overline{\mathbf{w}} + Z_{\Omega_\Sigma}(\nu)[\![\mathbf{w}]\!] \mid \overline{\mathbf{w}}, [\![\mathbf{w}]\!] \in (H^1(\Omega))^d, \mathbf{w} = \mathbf{0} \text{ on } \Gamma_D^u \right\}, \tag{6.4}$$

Using standard arguments, i.e. integrating over the domain the governing multiplied by the test functions, applying the divergence theorem, imposing the natural boundary conditions, and exploiting symmetry of the stress tensor, the weak form of the stead state hydromechanical problem reads:

At any time $t \in I$, find $(p, \mathbf{u}) \in \mathcal{V} \times \mathcal{U}$ such that:

$$\int_\Omega \nabla\varphi \cdot \left(\frac{1}{\mu} \tilde{\mathbf{K}} \nabla p \right) d\Omega = - \int_{\Gamma_N^p} \varphi q_N d\Gamma + \int_\Omega \varphi \tilde{q} d\Omega \qquad \forall\, \varphi \in \mathcal{V}_0, \tag{6.5}$$

$$\int_\Omega \nabla^s \boldsymbol{\psi} : (\tilde{\boldsymbol{\sigma}} - \tilde{\alpha} p \mathbf{1})\, d\Omega = \int_{\Gamma_N^u} \boldsymbol{\psi} \cdot \mathbf{t}_N \, d\Gamma \qquad \forall\, \boldsymbol{\psi} \in \mathcal{U}_0. \tag{6.6}$$

6.2 DISCRETIZATION

Let $\mathcal{T}_h$ be a partition of the domain Ω into n_{elem} nonoverlapping elements E_j, such that $\Omega \approx \Omega^h = \cup_{j=1}^{n_{elem}} E_j$ and $\Omega^h_\Sigma \subset \Omega^h$ is a finite element discretization os the *regularization band* Ω_Σ, as shown on chapter 3 for the flow problem. The finite element space associated with the standard Galerkin finite element method requires only $\mathcal{C}^0$ continuity for pressure and displacement:

$$\mathcal{V}^h = \left\{ \eta^h = \overline{\eta}^h + Z_{\Omega_\Sigma}(\nu)[\![\eta]\!]^h \mid \overline{\eta}^h, [\![\eta]\!]^h \in \mathcal{C}^0(\Omega) \right\}, \tag{6.7}$$

$$\mathcal{U}^h = \left\{ \mathbf{w}^h = \overline{\mathbf{w}}^h + Z_{\Omega_\Sigma}(\nu)[\![\mathbf{w}]\!]^h \mid \overline{\mathbf{w}}^h, [\![\mathbf{w}]\!]^h \in \left[\mathcal{C}^0(\Omega)\right]^d \right\}, \tag{6.8}$$

where $\mathcal{P}^1(E_j)$ denotes the polinomial space of degree 1 on E_j. The pressure and displacement field are interpolated as follows:

$$p^h = \sum_{i=1}^{n_{elem}} \varphi_i P_i, \tag{6.9}$$

$$\mathbf{u}^h = \sum_{j=1}^{n_{elem}} \boldsymbol{\psi}_j \mathbf{U}_j, \tag{6.10}$$

where P_j are the nodal pressures and $\mathbf{U}_j$ are the nodal displacements. The functions φ_i (respectively $\boldsymbol{\psi}_j$) are the usual finite element linear interpolation functions, which takes the value 1 at node i (respectively node j) and 0 at all the other nodes.

Applying Galerkin technique, the finite element discretization of Eqs. (6.5) and (6.6) reads:

$$\mathbf{K}^p\mathbf{P} = \mathbf{Q}^p, \tag{6.11}$$

$$\int_\Omega \nabla^s \boldsymbol{\psi}_j : \tilde{\boldsymbol{\sigma}} d\Omega - \mathbf{G}^u\mathbf{P} = \mathbf{F}^u, \tag{6.12}$$

where $\mathbf{P}$ is the vector of nodal pressures, $\mathbf{U}$ is the vector of nodal displacements, and $\mathbf{K}^p$, $\mathbf{Q}^p$, $\mathbf{G}^u$ and $\mathbf{F}^u$ are given by:

$$\mathbf{K}^p_{i,j} = \int_\Omega \boldsymbol{\nabla}\varphi_i \frac{1}{\mu} \tilde{\mathbf{K}} \boldsymbol{\nabla}\varphi_j d\Omega, \tag{6.13}$$

$$\mathbf{Q}^p_i = -\int_{\Gamma^p_N} \varphi_i q_N d\Gamma + \int_\Omega \varphi_i \tilde{q} d\Omega, \tag{6.14}$$

$$\mathbf{G}^u_{i,j} = \int_\Omega \nabla^s \boldsymbol{\psi}_i \tilde{\alpha} \mathbf{1} \varphi_j d\Omega, \tag{6.15}$$

$$\mathbf{F}^u_i = \int_{\Gamma^u_N} \boldsymbol{\psi}_i \cdot \mathbf{t}_N \, d\Gamma \tag{6.16}$$

6.2.1 Interface HAR finite element for the hidromechanical problem

The finite element strain and gradient of pressure fields on the interface element (see Fig. 3.2) can be written, according to the local coordinate system (τ, ν), as:

$$\boldsymbol{\epsilon} = \tilde{\boldsymbol{\epsilon}} + \underbrace{\frac{1}{h}\left(\boldsymbol{\nu} \otimes [\![\mathbf{u}]\!]\right)^s}_{\hat{\boldsymbol{\epsilon}}}, \tag{6.17}$$

$$\boldsymbol{\nabla} p = \boldsymbol{\nabla}\tilde{p} + \underbrace{\frac{1}{h}[\![p]\!]\boldsymbol{\nu}}_{\boldsymbol{\nabla}\hat{p}}, \tag{6.18}$$

where $\boldsymbol{\nu}$ represents the unit vector normal to the element base, $[\![\mathbf{u}]\!]$ and $[\![p]\!]$ are, respectively, the relative displacement and relative pressure between node 1 and its base projection $1'$, $\tilde{\boldsymbol{\epsilon}}$ and $\boldsymbol{\nabla}\tilde{p}$ are the counterpart of the standard approximations that do not depend on h. According to the local coordinate system (ν, τ), these components are given by:

$$\hat{\boldsymbol{\varepsilon}} = \frac{1}{b}\begin{bmatrix} u_\tau^{(3)} - u_\tau^{(2)} & \frac{1}{2}\left(u_\nu^{(3)} - u_\nu^{(2)}\right) \\ \frac{1}{2}\left(u_\nu^{(3)} - u_\nu^{(2)}\right) & 0 \end{bmatrix}, \tag{6.19}$$

$$\tilde{\boldsymbol{\varepsilon}} = \frac{1}{h}\begin{bmatrix} 0 & \frac{1}{2}[\![u_\tau]\!] \\ \frac{1}{2}[\![u_\tau]\!] & [\![u_\nu]\!] \end{bmatrix}, \tag{6.20}$$

$$\boldsymbol{\nabla}\hat{p} = \frac{1}{b}\left\{\begin{matrix} p^{(3)} - p^{(2)} \\ 0 \end{matrix}\right\}, \tag{6.21}$$

$$\boldsymbol{\nabla}\tilde{p} = \frac{1}{h}\left\{\begin{matrix} 0 \\ [\![p]\!] \end{matrix}\right\}, \tag{6.22}$$

where

$$[\![\mathbf{u}]\!] = \left\{\begin{matrix} [\![u_\tau]\!] \\ [\![u_\nu]\!] \end{matrix}\right\} = \left\{\begin{matrix} u_\tau^{(1)} - u_\tau^{(1')} \\ u_\nu^{(1)} - u_\nu^{(1')} \end{matrix}\right\}, \qquad [\![p]\!] = p^{(1)} - p^{(1')}. \tag{6.23}$$

Here, $u_\tau^{(i)}$, $u_\nu^{(i)}$ and $p^{(i)}$ are the components of the displacement and the pressure of node i, $u_{\tau,\nu}^{(1')} = u_{\tau,\nu}^{(3)} b_2/b + u_{\tau,\nu}^{(2)}(1 - b_2/b)$ and $p^{(1')} = p^{(3)} b_2/b + p^{(2)}(1 - b_2/b)$ are the displacement and pressure evaluated at the point $1'$ by interpolation the corresponding nodal values. Note that the expressions (6.17) and (6.18) are equivalent to the regularized discontinuity regime (Eqs. 4.36 and 4.37).

In the limit when the height h tends to zero, node 1 tends to the same material point as its projection $1'$, consequently the relative displacement $[\![\mathbf{u}]\!]$ and pressure $[\![p]\!]$ become a measurement of the corresponding field discontinuity. Therefore, HAR elements provide the element for the spaces $\mathcal{V}^h$ and $\mathcal{U}^h$, been suitable to represent fractures, as long as provided with appropriate constitutive equations as shown on chapter 5.

CHAPTER 7

NUMERICAL RESULTS

Some numerical results are presented in this section in order to illustrate the properties of the numerical model proposed in this work. The efficiency of the flow model presented on chapter 2 is verified on sec. 7.1 through some synthetic, yet representative, numerical examples. The constitutive model for the fracture's mechanical behavior presented in chapter 5 is validated on sec. 7.2, showing good agreement to the nonlinear Barton-Bandis model. Finally, the coupled hydromechanical model is used in sec. 7.3 to investigate the effects of natural fractures on the overall permeability of a fractured porous rock, and its dependence of the stress state.

7.1 NUMERICAL RESULTS FOR THE FLOW PROBLEM ON FRACTURATED POROUS DOMAIN

The numerical examples begins by first exploring the flow model. The first test case consists on a single fracture crossing the whole porous domain. In section 7.1.1, it is show that, as long the aspect ratio (AR) of the interface HAR element remains small, the numerical scheme presented in this work provides consistent results, properly modeling velocity jumps across the fracture that can occur when the longitudinal permeability is large enough. In section 7.1.1, the second test case shows that the proposed interface model is able to properly handle a geological barrier (with a small normal permeability in the fracture). The test case of section 7.1.2 is a combination of the two previous problems: a fracture with anisotropic permeabilities, which creates a zone where both pressure field and fluid velocity are discontinuous across the fracture. The test case of section 7.1.3 consists on a domain containing a partially immersed fracture. Finally, the last test case ofr the flow problem is given on section 7.1.4, consisting on a benchmark case with a network of crossing fractures, where the solution obtained by the interface HAR model is compared against the solution given by different models available in the literature.

In order to evaluate the numerical solution obtained by the interface HAR model, the solution is compared with a reference solution obtained using the standard model, where the fracture domain Ω_f is properly discretized with standard Galerkin elements on a very fine unstructured mesh. The reference solution is considered a good approximation of the actual solution when the mesh convergence is reached, that is when the magnitude of the difference between solutions do not vary significantly when the meshes are refined.

7.1.1 Single fracture with isotropic permeability

To show the efficiency of the interface HAR model and the influence of the interface element height h, we first perform two test cases presented by Martin, Jaffré e Roberts (2005) and Ahmed et al. (2015), involving a rectangular domain containing a single fracture, with different permeability and boundary conditions, as shown in Fig. 7.1. The lengths of the porous domain in the x and y directions are $L_x = 2$m and $L_y = 1$m, and the fracture width is $w = 0.01$m. The fluid viscosity and the source term are adopted as $\mu = 1$ and $q = q_f = 0$. The reference solution is obtained on a unstructured mesh containing 9662 triangular elements, which resolves the fracture with 4 elements in its normal direction and becomes coarser away from the fracture (see fig. 7.2). The interface model solutions are obtained with regular meshes of triangular elements of side length L_h, where the regularization band is discretized with HAR elements. For all the examples, the aspect ratio of the HAR elements is AR $= 100$ (i.e. the element height h is equal to 1% of the length b of the base), unless stated otherwise.

High permeability in the fracture and Dirichlet boundary conditions

The test case is described in Fig. 7.1(a). The matrix permeability tensor is given by the rank-2 identity tensor, $\mathbf{K} = \mathbf{1}$, while the permeability tensor in the whole fracture is given by $\mathbf{K}_{f_1} = \mathbf{K}_{f_2} = 100\mathbf{K}$ (i.e. $\mathrm{K}_{f,\tau} = \mathrm{K}_{f,\nu} = 100$), allowing the fluid to flow along and across the fracture. The interface model solution was computed on meshes of size $L_h = 1.25 \times 10^{-1}$ m and $L_h = 6.25 \times 10^{-2}$ m. Figure 7.3 compares the pressure field of the reference solution and the interface model solution, while Fig. 7.4 shows the pressure field on the cut lines $y = 0.125$ m and $y = 0.5$ m. It can be seen on Fig. 7.4 a small difference on the curves obtained with the reference solution and the interface model for $L_h = 1.25 \times 10^{-1}$ m, while the curves for $L_h = 6.25 \times 10^{-2}$ m are nearly identical to the reference.

In order to evaluate the influence of the aspect ratio of the HAR element on the solution, Fig. 7.5 compares the reference solution and the interface model solution computed on meshes of size $L_h = 6.25 \times 10^{-2}$ m and different values of AR. The curve with AR $= 100$ is hidden behind the curve with AR $= 20$, while the solution for AR $= 2.86$ shows a discrepancy from the reference solution. It can also be seen on the zoomed detail on Fig 7.5 that the solution becomes closer to the reference as the aspect ratio decreases. Therefore, smaller AR should produce more accurate responses. The value of AR $= 100$ is recommended, based on the author experience and on Manzoli et al. (2016).

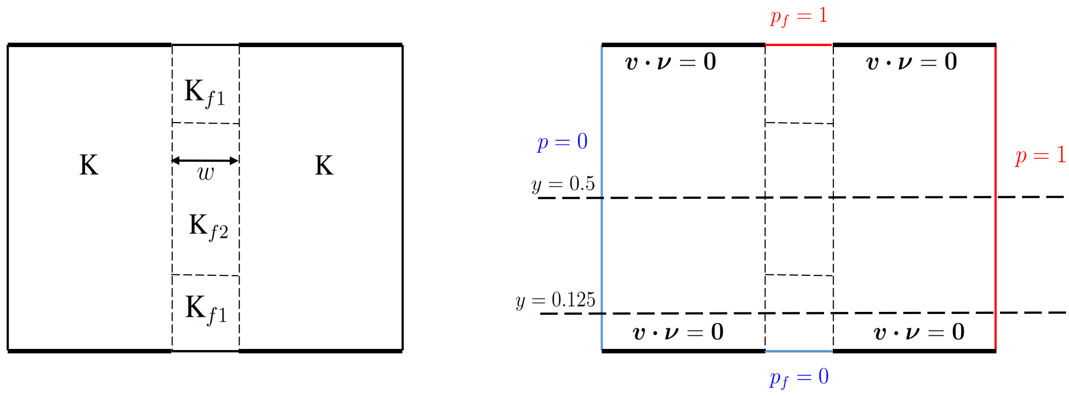

(a) Fracture with Dirichlet boundary condition.

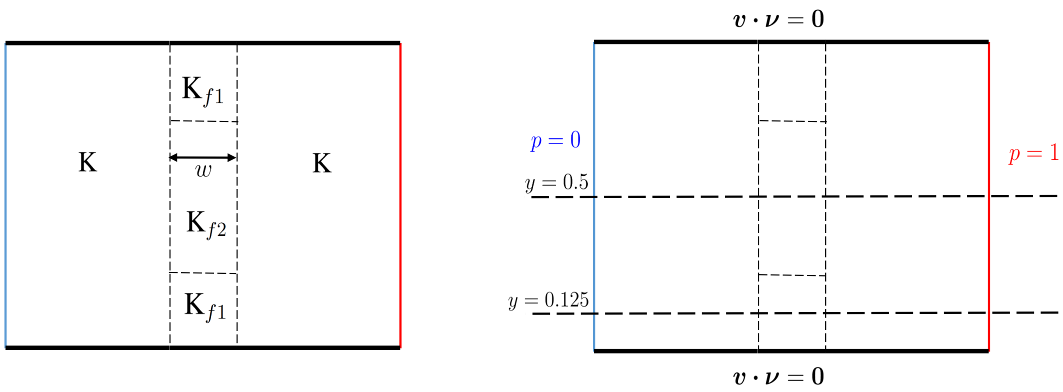

(b) Fracture with Neumann boundary condition.

Figure 7.1: Domain crossed by a single fracture, depicted with dashed lines. The fracture is caracterized by two permeability tensors. Homogeneous Neumann boundary conditions are depicted with fat lines.

LOW PERMEABILITY IN THE CENTER PART OF THE FRACTURE AND NEUMANN BOUNDARY CONDITIONS

The test case is described in Fig. 7.1(b). The permeability in the outer part of the fracture equals the matrix, $\mathbf{K}_{f_1} = \mathbf{K} = \mathbf{1}$, while the central part of the fracture has a lower permeability, $\mathrm{K}_{f_2,\tau} = \mathrm{K}_{f_2,\nu} = 0.002$, representing a geological barrier. Obviously, the fluid tends to avoid the geological barrier and flow around it. Therefore, pressure is discontinuous across the fracture. Figures 7.6 and 7.7 shows the good agreement between the interface model solution and the reference solution, showing that the model is able to reproduce barrier effects.

7.1.2 SINGLE FRACTURE WITH ANISOTROPIC PERMEABILITY

This test case is described by Fig. 7.10(a), with an anisotropic and discontinuous permeability tensor in the fracture, given by $\mathrm{K}_{f_1,\nu} = \mathrm{K}_{f_2,\tau} = 0.005$ and $\mathrm{K}_{f_1,\tau} = \mathrm{K}_{f_2,\nu} = 200$. With this

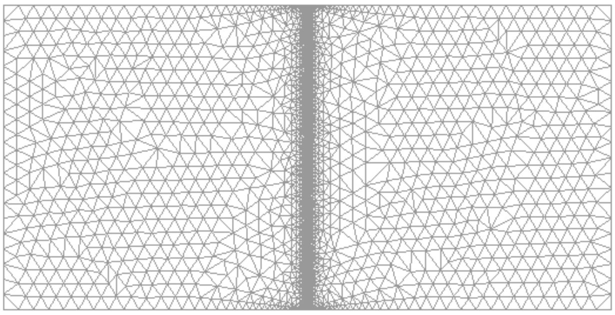

(a) Reference mesh, 9662 standard elements and aperture $w = 0.01$ m.

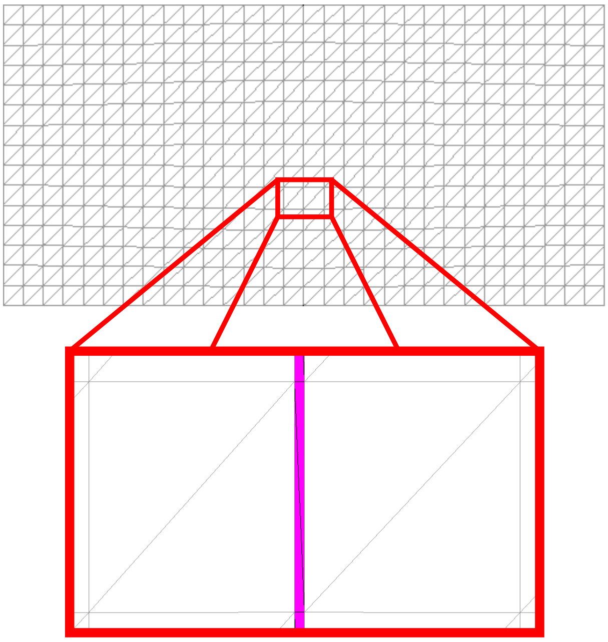

(b) Interface model with mesh size $L_h = 6.25 \times 10^{-2}$ m. 900 standard elements + 30 interface HAR elements.

Figure 7.2: (a) Standard mesh, where the fracture domain Ω_f is explicitly representend. (b) Interface model mesh, where the fracture is represented by a thin strip of interface HAR elements. The HAR elements are so thin they can hardly be spotted on the mesh.

configuration fluid cannot flow along the middle part of the fracture but can cross it. The flow behavior is opposite in the outer parts of the fracture.

Figure 7.8 compares the pressure field of the reference solution with the interface model solution, while Fig. 7.9 shows the pressure field on the cut lines $y = 0.125$ m and $y = 0.5$ m. The zoomed detail on Figs. 7.9(a) and 7.9(b) shows that, in this test case, the interface model solution does not correctly approach the reference solution everywhere, especially in the regions close to the extremities of the fracture. According to (MARTIN; JAFFRÉ; ROBERTS, 2005), this discrepancy close to the fracture extremities might be due to the high singularities at the exits of the fractures.

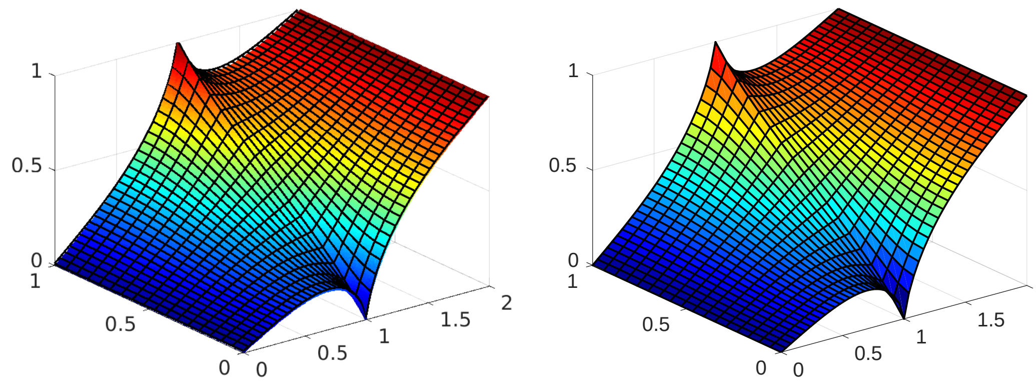

(a) Reference solution. (b) Interface model, $L_h = 6.25 \times 10^{-2}$ m.

Figure 7.3: Pressure field for the reference solution and the interface HAR model for the conductive fracture case. For visualization purposes, the mesh was replaced by a square grid, providing a better comprehension of the results.

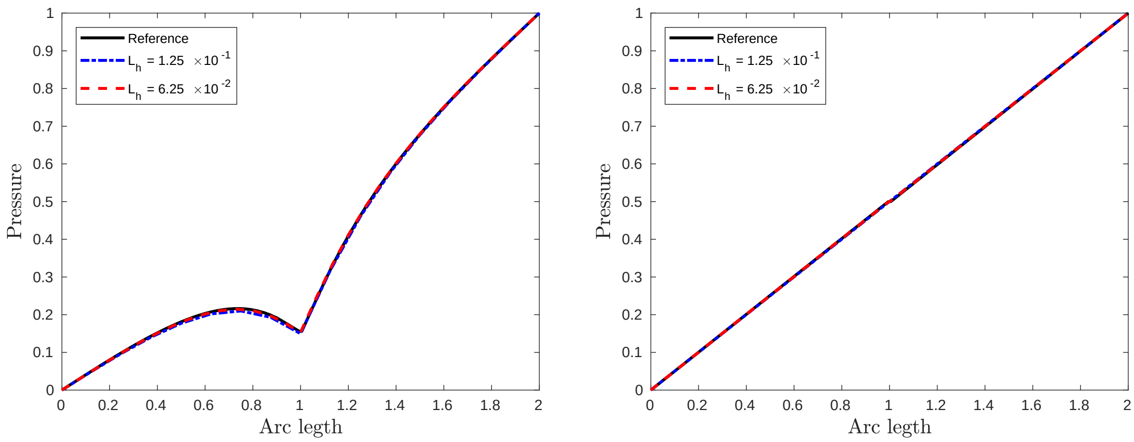

(a) Pressure along the cutline $y = 0.125$ m. (b) Pressure along the cutline $y = 0.5$ m.

Figure 7.4: Comparison of the pressure across the fracture for the reference solution and interface HAR model for different mesh sizes.

7.1.3 Half fracture

We now solve the test case presented in Angot, Boyer e Hubert (2009) where the fracture crosses only half of the domain. The porous domain is a square with lengths $L_x = L_y = 1.0$m, with a half fracture $\Sigma \times \left[-\frac{w}{2}, \frac{w}{2}\right]$, with $\Sigma = \{(x, y) \in \mathbb{R}^2;\ x = 0.5,\ y \geq 0.5\}$ and constant width $w = 0.01$ m. The fracture has a very high anisotropy, $\mathrm{K}_{f,\nu} = 1.0 \times 10^{-4}$, $\mathrm{K}_{f,\tau} = 100$. Two different Dirichlet boundary conditions are considered (see Fig. 7.10), the first one leading to a symmetric flow (Fig. 7.10(a)), and the second one leading to a non-symmetric flow (Fig. 7.10(b)).

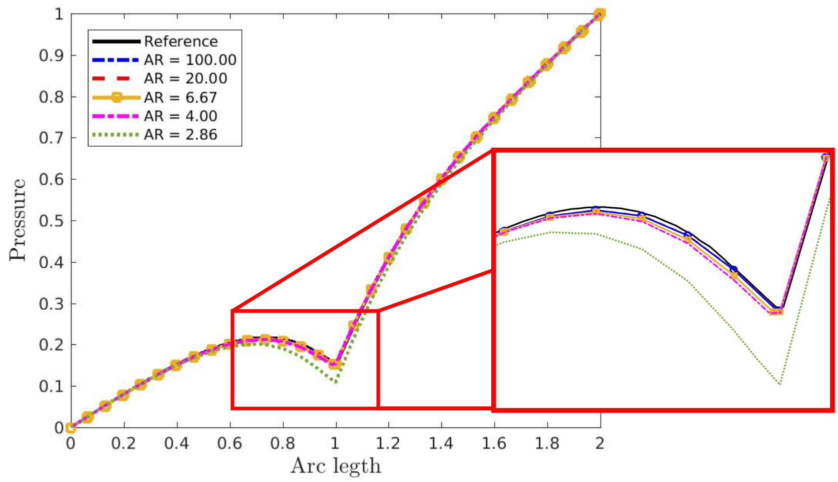

(a) Pressure along the cut line $y = 0.125$ m.

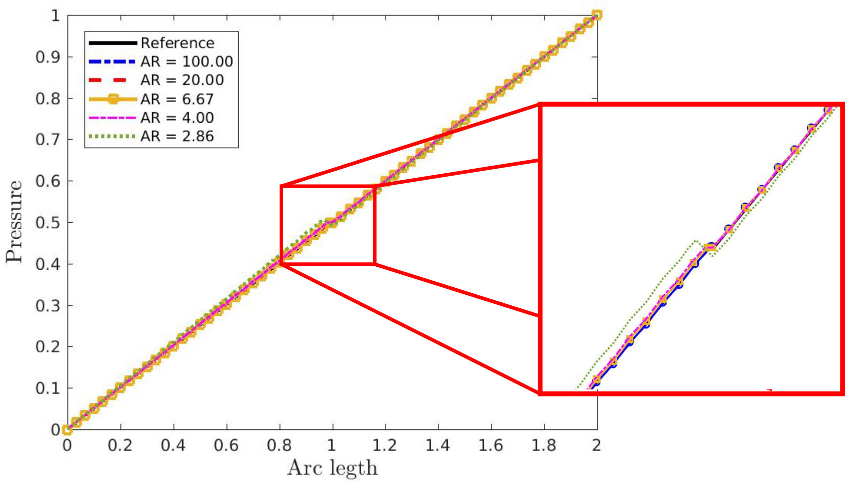

(b) Pressure along the cut line $y = 0.5$ m.

Figure 7.5: Comparison of the pressure field across the fracture for the reference solution and interface HAR model for different values of aspect ratios AR.

The numerical results for both the Standard model and the interface HAR model are presented when the mesh convergence is reached, that is when the magnitude of the difference between the two solutions do not vary when the meshes are refined, and are shown on Fig. 7.11. The pressure field of the reference solution and the interface model for the symmetric case are shown on Fig. 7.12 and for non-symmetric flow on Fig. 7.14. The pressure distribution on the cut lines $y = 0.5625$ m and $y = 0.75$ m, and along the fracture, are represented for the symmetric case on Fig. 7.13 and for the non-symmetric case on Fig. 7.15. The pressure along the fracture computed by the reference solution is represented by the mean pressure $p(s) = \frac{1}{w}\int_{-w/2}^{w/2} p(s,t)\, dt$.

Note that, for both cases, the pressure field given by the reference solution varies inside the fracture and, for that reason, the interface model does not approach correctly the reference solution. A similar result is reported by (ANGOT; BOYER; HUBERT, 2009) and is a consequence

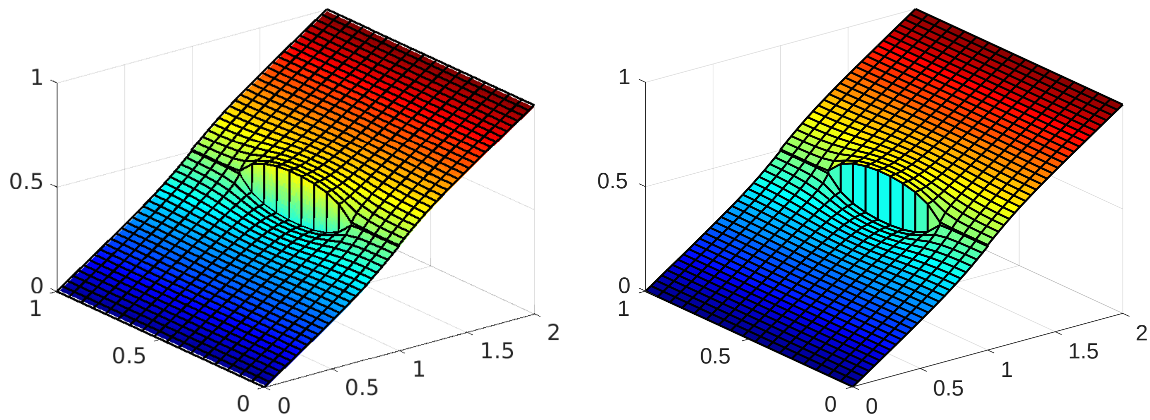

(a) Reference solution.

(b) $h = 5.0 \times 10^{-2}$ m.

Figure 7.6: Pressure field for the reference solution and interface HAR model for the barrier case.

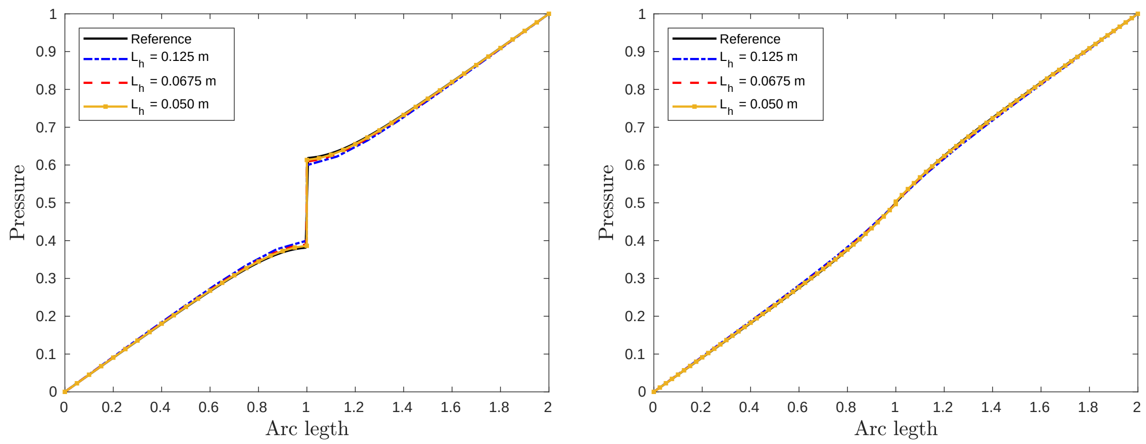

(a) Pressure along the cut line $y = 0.125$ m.

(b) Pressure along the cut line $y = 0.5$ m.

Figure 7.7: Comparison of the pressure across the fracture for the reference solution and interface HAR model for different mesh sizes.

of the fracture simplification made by the reduction of the fracture dimension.

7.1.4 Benchmark

In this section we consider one of the benchmark cases defined in (FLEMISCH et al., 2018). It consists on a square domain with lengths $L_x = L_y = 1.0$ m, including the fracture network geometry and boundary conditions shown on Fig. 7.16(a). The mesh used to compute the interface HAR model solution in shown on Fig. 7.16(b). The matrix permeability is $\mathbf{K} = \mathbf{1}$ and the fractures have constant aperture $w = 1.0 \times 10^{-4}$ m. For the fracture permeability, two cases are considered: a highly conductive fracture network with $\mathrm{K}_{f,\nu} = \mathrm{K}_{f,\tau} = 1.0 \times 10^4$, and the

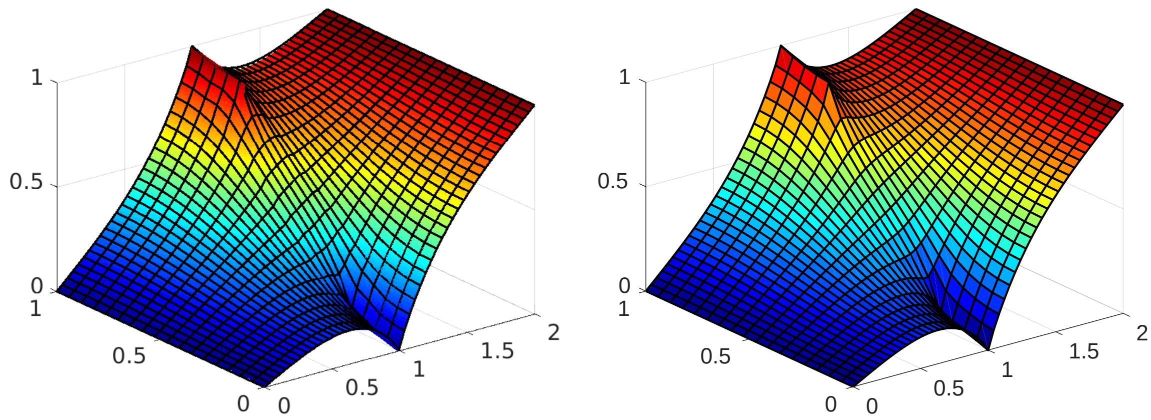

(a) Reference solution. (b) Interface model, $L_h = 5.0 \times 10^{-2}$ m.

Figure 7.8: Pressure field for the reference solution and interface HAR model for the anisotropic case.

case of blocking fractures with $\mathrm{K}_{f,\nu} = \mathrm{K}_{f,\tau} = 1.0 \times 10^{-4}$.

The results obtained with the interface HAR model are compared against those given in (FLEMISCH et al., 2018), which are available at <https://git.iws.uni-stuttgart.de/benchmarks/fracture-flow>. The reference solution obtained in (FLEMISCH et al., 2018) was computed using a mimetic finite difference (MFD) method on a very fine reference mesh containing 1175056 elements, which resolves every fractures with 10 elements in its normal direction and becomes coarser away from the fracture. The six methods considered in (FLEMISCH et al., 2018) are listed in table 7.1. For details about those methods, the reader must refer to (FLEMISCH et al., 2018) and the references therein.

Table 7.1: List of methods in the original benchmark paper (FLEMISCH et al., 2018).

Box	Vertex-centered finite-volume method
TPFA	Control volume two-point flux approximation
MPFA	Control volume multi-point flux approximation
EDFM	Embedded discrete fracture–matrix model
Flux-Mortar	Mortar discrete fracture–matrix model
P-XFEM	Primal extended finite element method
D-FEM	Dual extended finite element method

The pressure field for the interface HAR model solution for both conductive and blocking case is shown on Fig. 7.17. For the conductive case, Fig. 7.18 shows the plot of the pressure distribution along the cut lines $y = 0.7$ m and $x = 0.5$ m, in comparison to the results reported in (FLEMISCH et al., 2018). For the blocking case, Fig 7.19 compares the pressure distribution along the diagonal cut line $(0.0, 0.1) - (0.9, 1.0)$ crossing the whole domain. As can be seen, for both cases the solution obtained with the interface HAR model shows a good agreement with the compared methods.

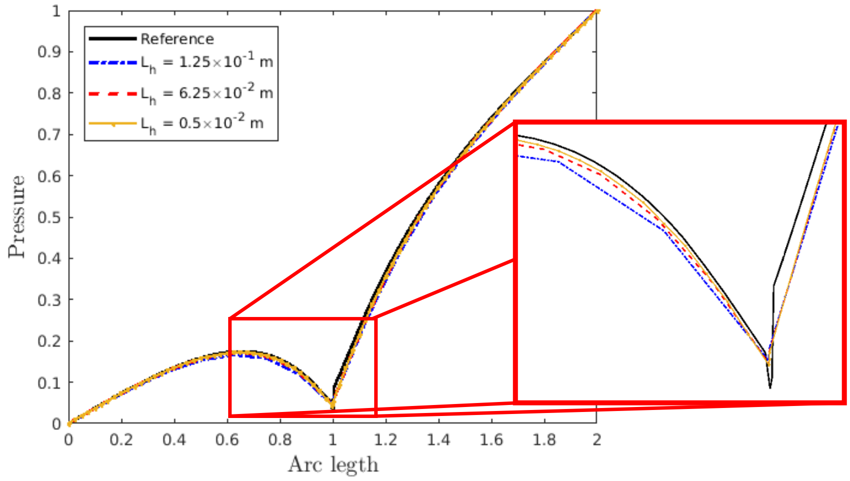

(a) Pressure along the cut line $y = 0.125$ m.

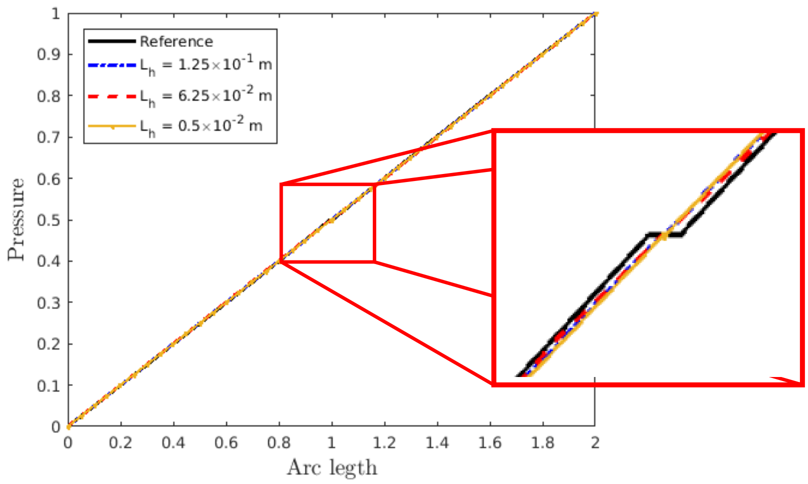

(b) Pressure along the cut line $y = 0.5$ m.

Figure 7.9: Comparison of the pressure across the fracture for the global solution and HAR-scheme.

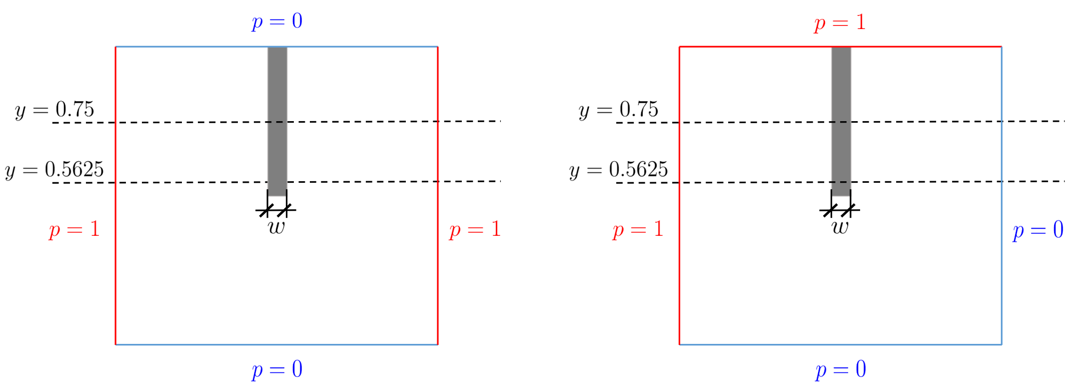

(a) Symmetric flow.

(b) Non symmetric flow.

Figure 7.10: Domain and boundary conditions for a half fracture tests.

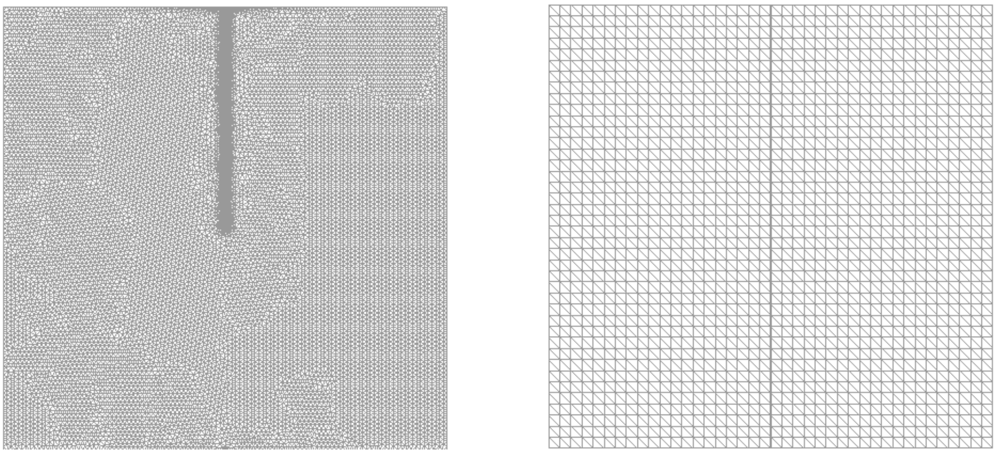

(a) Reference mesh, 39512 standard elements. (b) Interface model mesh, 3200 standard elements + 39 interface HAR elements.

Figure 7.11: Explicitly representation of the fracture with a locally refined mesh around the fracture and interface model mesh.

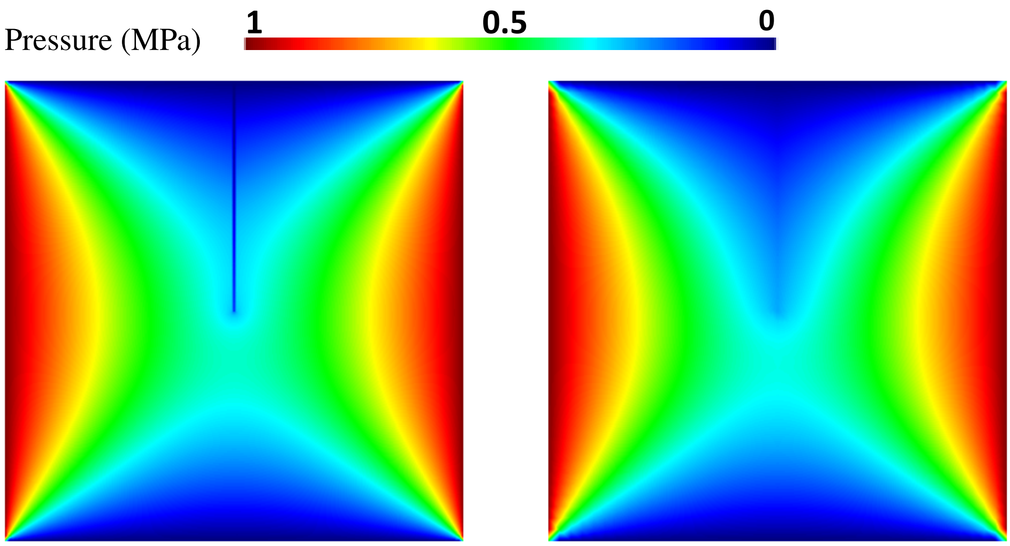

(a) Reference solution. (b) Interface model solution.

Figure 7.12: Pressure field for for the symmetric case computed by the global solution and HAR-scheme.

7.2 Numerical results for the fracture constitutive model

Some examples are now given to validate the fracture continuum constitutive model proposed on chapter 5. A numerical simulation of a compression test is presented on section 7.2.1, in order to compare the fracture continuum constitutive model and the Barton-Bandis hyperbolic law, Eq. (5.1). A parametric study about the influence of the initial normal stiffness k_{ni} and the maximum closure V_m on the fracture normal deformation is conducted on section 7.2.2. A direct shear test is simulated on section 7.2.3 in order to validate the proposed model against

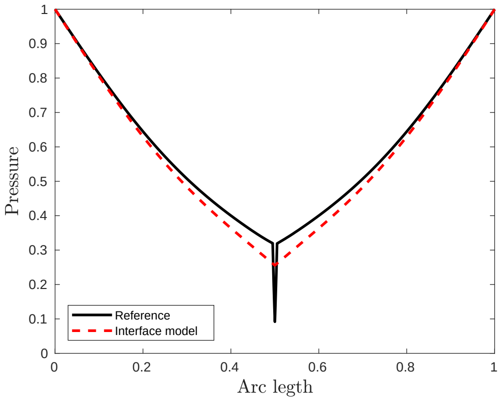

(a) Pressure on the cutline $y = 0.5625$m.

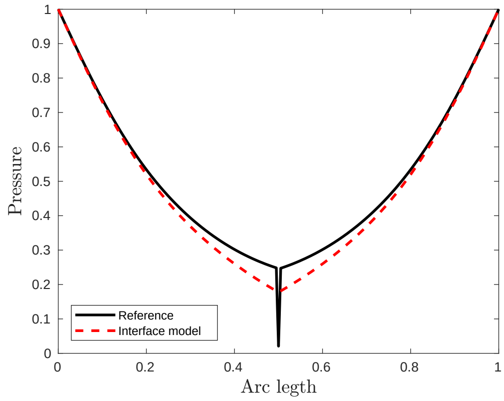

(b) Pressure on the cutline $y = 0.75$m.

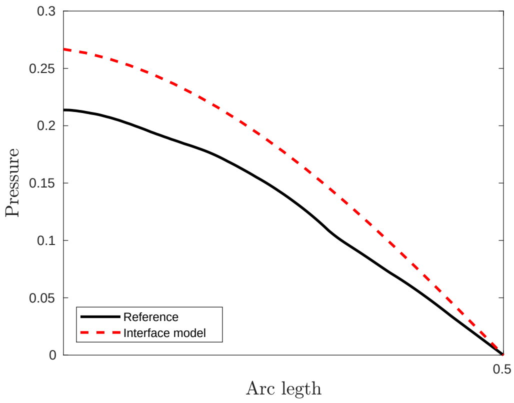

(c) Pressure along the fracture.

Figure 7.13: Comparison of the pressure along and across the fracture for the global solution and HAR-scheme.

the prediction of the Barton-Bandis shear deformation equation, Eq. (5.5). Section 7.2.4 conducts a study of the influence of fracture size on the shear deformation. Finally, the study of the influence of normal compressive stress on the shear deformation is conducted on section 7.2.5.

7.2.1 Single fracture normal deformation

The compression test is performed on a rectangular block with lengths $L_x = 0.1$ m and $L_y - 0.2$ m on the x and y directions, respectively. The block contains a horizontal planar fracture at $y = 0.1$ m and is subjected to a vertical loading of 5 MPa. On the left side figure 7.20 we show a representation of the finite element mesh employed and boundary conditions applied. The size of interface elements representing the fracture is intentionally exaggerated in order to provide a better visualization. On the right the side of figure 7.20 we show the real mesh employed, where the interface element height is $h = 1.0 \times 10^{-4}$ m.

The block has a Young modulus $E = 30$ GPa and Poisson coefficient $\nu = 0.3$, while the

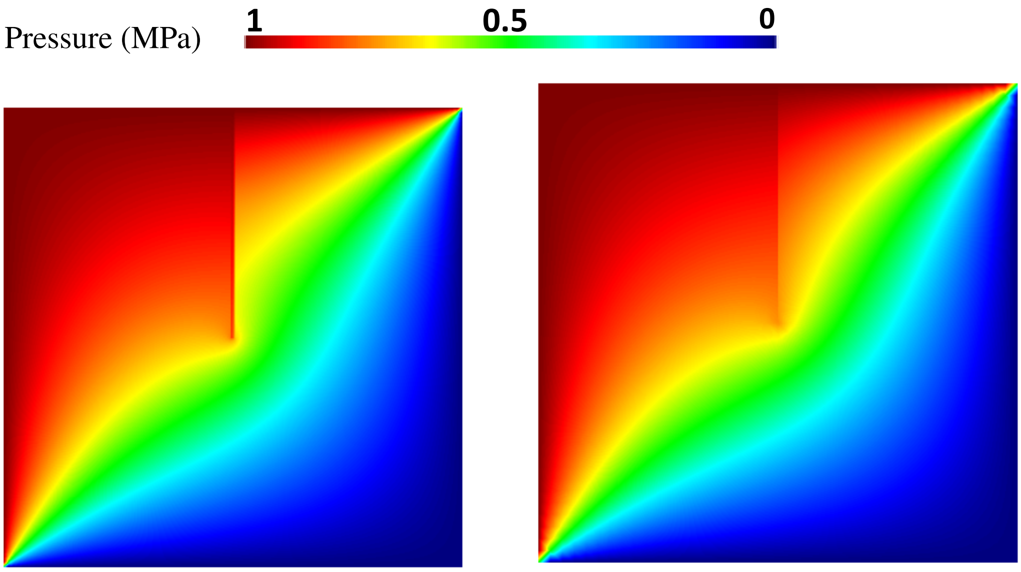

(a) Reference solution.

(b) Interface model solution.

Figure 7.14: Pressure field for the non-symmetric case computed by the global solution and HAR-scheme.

fracture has an initial normal stiffness of $k_{ni} = 1.0 \times 10^5$ MPa/m and a maximum closure of $V_m = 5.0 \times 10{-}5$ m. Figure 7.21 shows the normal stress-displacement curve predicted by Barton-Bandis model and the curves obtained from the proposed constitutive model, for different values of time step. As can be seen, for smaller time step values, the proposed constitutive model is able to capture the nonlinear behavior of the hyperbolic law. The model, however, presents some small oscillations around the theoretical curve for larger time steps. These oscillations are caused by the IMPL-EX integration algorithm, due to the relaxation on the consistency equation by linearly extrapolate the internal contact variable. Therefore, the value of the time step must be controlled in order to reduce the error to an acceptable precision.

7.2.2 Parametric study of the initial normal stiffness

We now study the influence of the initial normal stiffness on the fracture normal deformation. The maximum closure has a fixed value ($V_m = 2.0 \times 10^{-4}$ m), and the problem is solved for three different values of the initial normal stiffness k_{ni}.

Figure 7.22 shows normal stress-displacement for different values of k_{ni} and a fixed value of the maximum closure $V_m = 2.0 \times 10^{-4}$ m. As can be seen, the stiffer the fracture initially is, the less it closes. From a numerical point of view, stiffer fracture are more nonlinear, and therefore require lower time steps to be simulated with and acceptable precision. From a practical point of view, the flow on a porous media containing conductive fractures will be dominated by the stiffer fractures in case of depletion (i.e. decrease on the fluid pressure on the porous medium), since these fractures will remain more opened than the others. On the other hand, if the porous

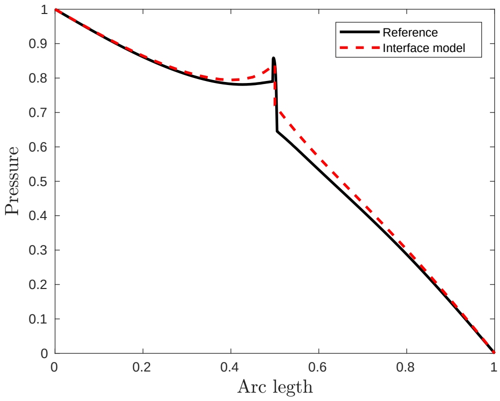

(a) Pressure on the cutline $y = 0.5625$m.

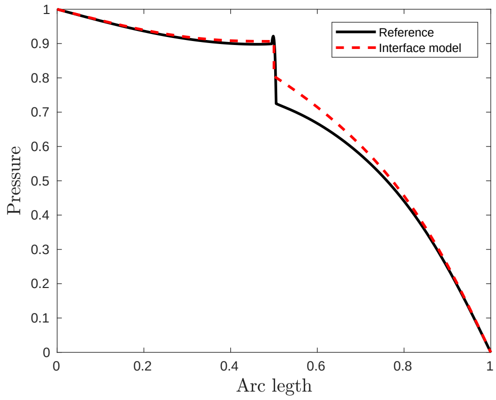

(b) Pressure on the cutline $y = 0.75$m.

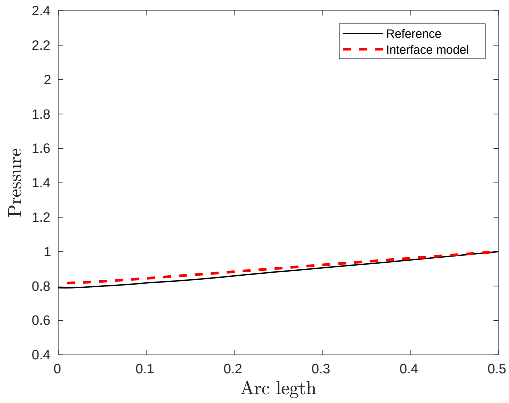

(c) Pressure along the fracture.

Figure 7.15: Comparison of the pressure along and across the fracture for the global solution and the HAR-scheme.

media contains only lower stiffness fractures, depletion will cause a rapidly decrease on the flow, which is undesirable for oil and gas production, for example.

7.2.3 Single fracture shear deformation

The simulation of a direct shear test is now performed on the rectangular block from the previous example. The block is first subjected to a vertical load such that the compressive stress on the fracture is 5 MPa. Keeping this force constant, an increasing horizontal displacement is imposed on the upper block (see Fig. 7.23).

The fractures parameters for the shear model are $JRC = 15$, $JCS = 150$ MPa, $\phi = 30°$, $k_{ni} = 1.0 \times 10^5$ MPa/m, and $V_m = 5.0 \times 10^{-5}$ m.

The fractures parameters for the shear model are $JRC = 15$, $JCS = 150$ MPa, $\phi = 30°$, $k_{ni} = 1.0 \times 10^5$ MPa/m, and $V_m = 5.0 \times 10^{-5}$ m. Figure 7.24(a) shows a good agreement between the shear stress-displacement curve obtained from the proposed constitutive model

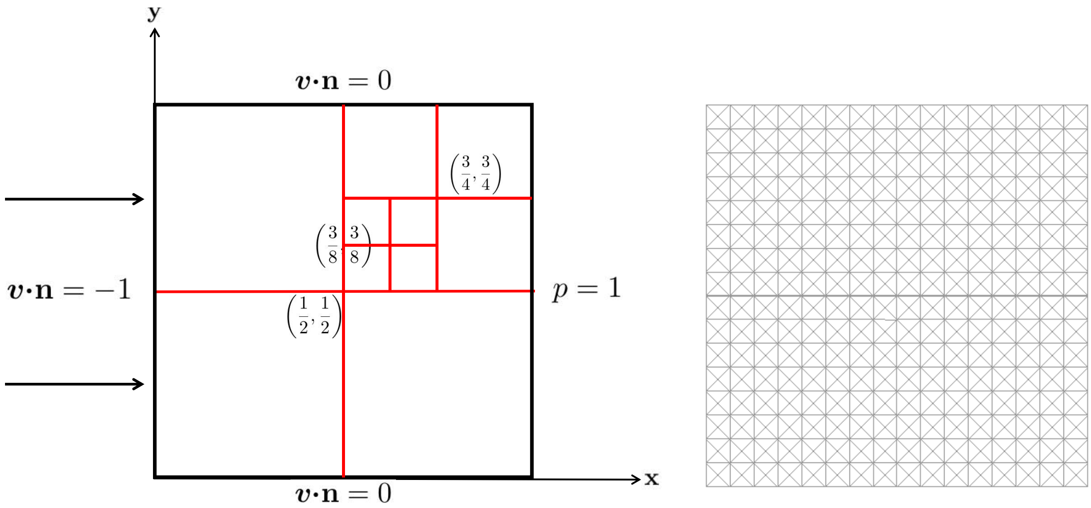

(a)

(b)

Figure 7.16: Benchmark case. (a) Domain geometry and boundary conditions. (b) Interface model mesh, 1024 standard elements + 112 interface HAR elements.

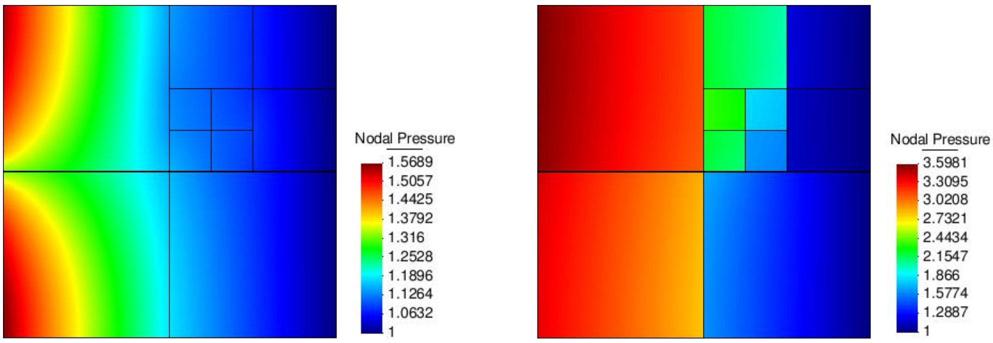

(a) Conductive case.

(b) Blocking case.

Figure 7.17: Interface HAR model solution for the benchmark case.

and the one predicted by Barton-Bandis model. Good agreement is also found on the dilation curves shown on fig. 7.24(b). The IMPL-EX algorithm also causes numerical oscillations on the shear and dilation curves, but they usually become negligible for the typical time step required for the contact model.

7.2.4 Study of the influence of fracture scale on shear deformation

In order to investigate the influence of the scale on fracture's shear and dilation, we simulate the direct shear test for different size of fractures, considering test on section 7.2.3 as the laboratory scale. Table 7.2 shows that increasing fracture size or length leads to a gradual increase in the peak shear displacement, while the values of the roughness coefficient JRC and

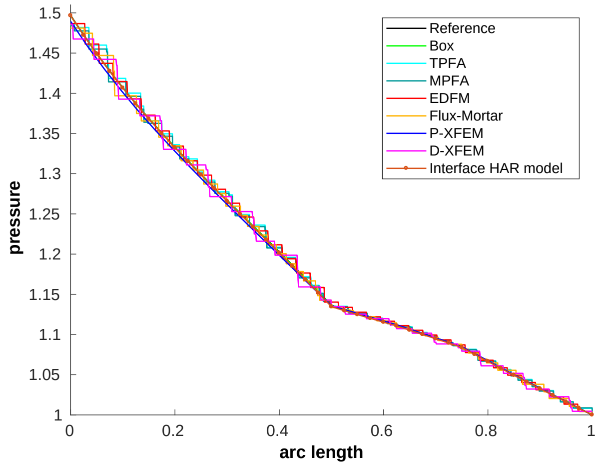

(a) Pressure along the cut line $y = 0.7$ m.

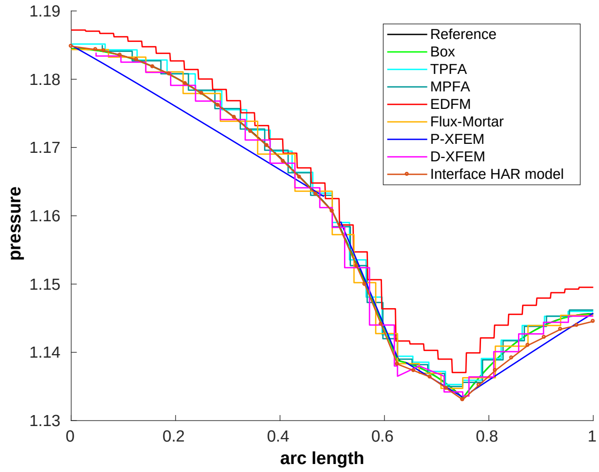

(b) Pressure along the cut line $x = 0.5$ m.

Figure 7.18: Benchmark conductive case: comparison of the pressure distribution along two cut lines.

the compressive strength JCS gradually decrease.

Table 7.2: Scaled parameter of the fracture.

L [m]	0.1	1.0	2.0
JRC $[-]$	15	7.5	6.6
JCS [MPa]	150	50	40
$[\![u_{\tau,peak}]\!]$ [mm]	10.0	4.0	6.1
ϕ $[°]$	30	30	30

Figure 7.25(a) shows a transitions on the mode of shear failure as the size of the fracture

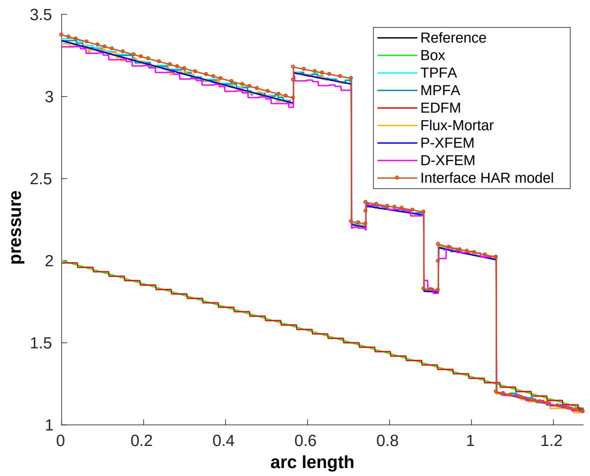

Figure 7.19: Benchmark blocking case: comparison of the pressure distribution along the cut line $(0.0, 0.1) - (0.9, 1.0)$.

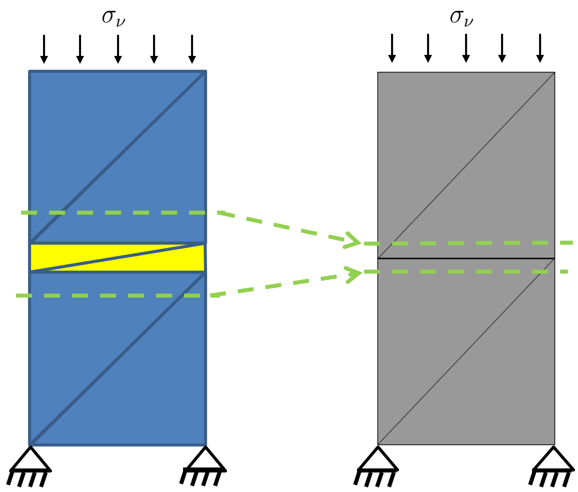

Figure 7.20: Numerical simulation of a compression test.

increases: from a brittle failure with small peak displacement for small fractures to a plastic failure with bigger peak displacement for larger fractures. This result suggests that the shear behavior of larger fractures can be well represented by a simple Mohr-Coulomb elastoplastic model, which leads to a great model simplification and reduction of computation effort.

Figure 7.25(b) shows that the dilation decreases with the increase of length, once the dilation angle follows the decrease on the JRC and JCS coefficients. It should be pointed that smoother fractures should be less affected by the increase of scale, since their roughness coefficient will not be greatly affected by the scale.

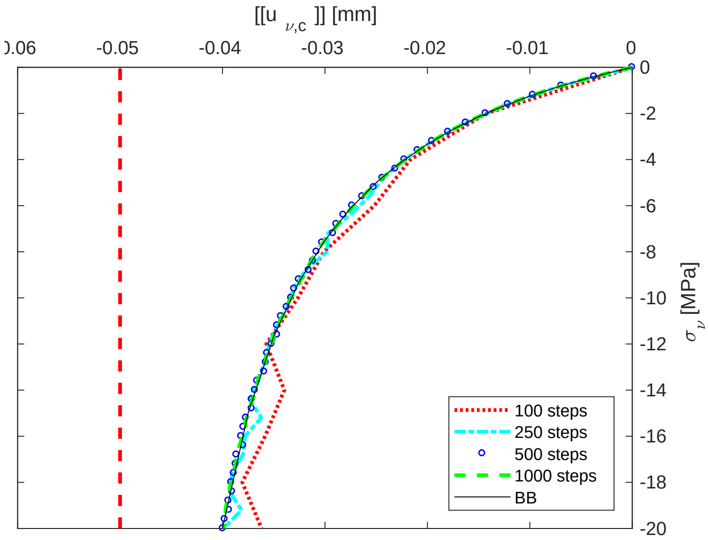

Figure 7.21: Comparison of the fracture normal deformation obtained from the Barton-Bandis model and the fracture constitutive model for different values of time step.

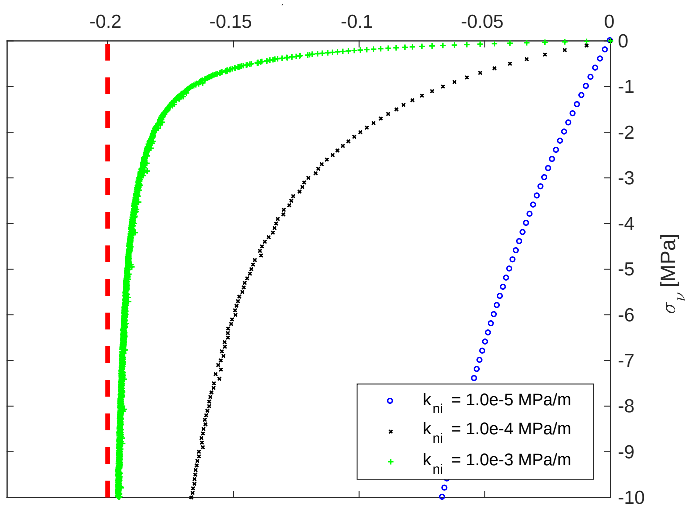

Figure 7.22: Fracture normal stress-displacement for different values of k_{ni}.

7.2.5 Study of the influence of normal stress on fracture shear deformation

The influence of the normal stress on fracture shear and dilation is shown on Figs. 7.26(a) and 7.26(b). Since the increase on the normal stress affects the mobilized friction angle ϕ_{mob}, the shear strength of the fracture increases on a sublinear rate with the normal stress, in contrast

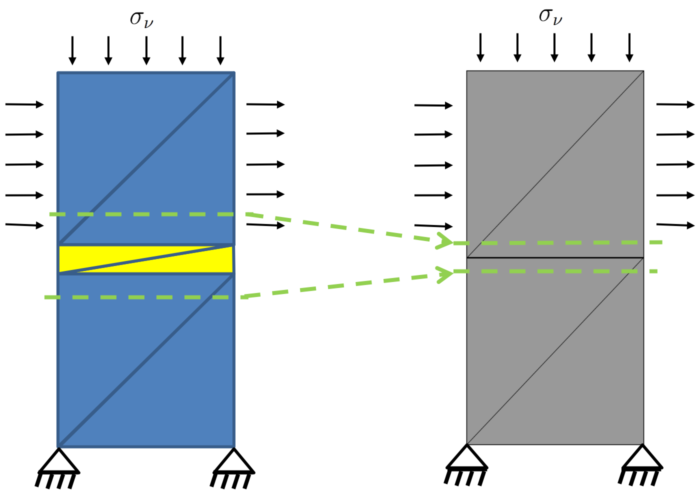

Figure 7.23: Numerical simulation of a direct shear test.

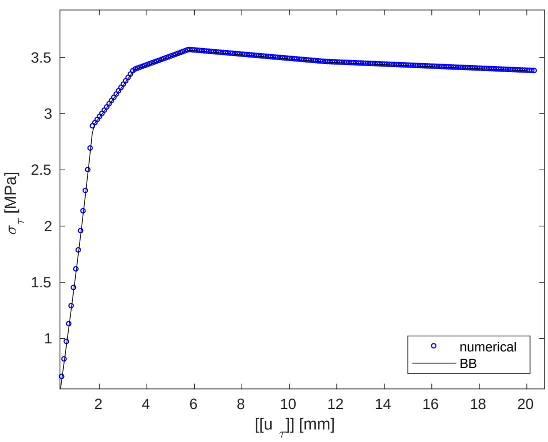

(a) Shear stress-displacement curve.

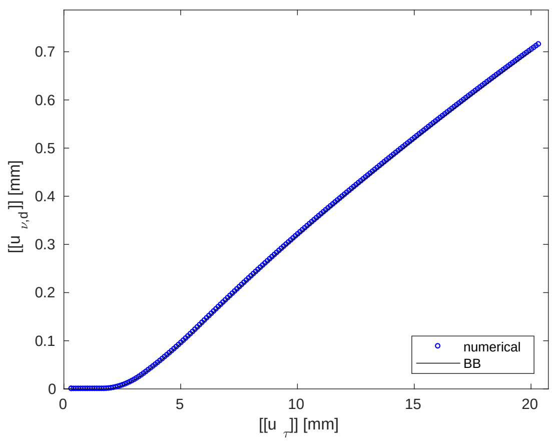

(b) Dilation vs shear displacement curve.

Figure 7.24: Comparison of the fracture constitutive model and the Barton-Bandis model for fracture shear deformation and dilation.

with the linear relation of the Mohr-Coulomb classical criteria. Dilation, instead, decreases with the increase of the normal stress, due to the reduction on the mobilized dilation angle d_{mob}.

7.3 Numerical results for the hydromechanical problem on fractured porous media

The main objective of the present work is to study the influence of fractures on the hydromechanical behavior of saturated porous media. Example 7.3.1 consists on the depletion of a porous domain containing a single fracture simple. The fracture closure caused by the depletion is compared to the Barton-Bandis model in order to validate the coupled hydromechanical

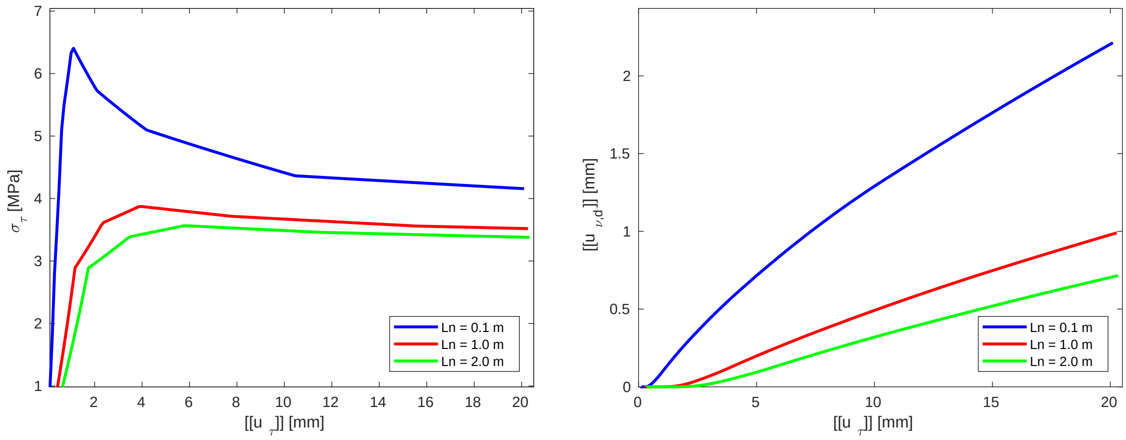

(a) Shear stress-displacement curve.

(b) Dilation vs shear displacement curve.

Figure 7.25: Scale effects on shear stress and dilation curves.

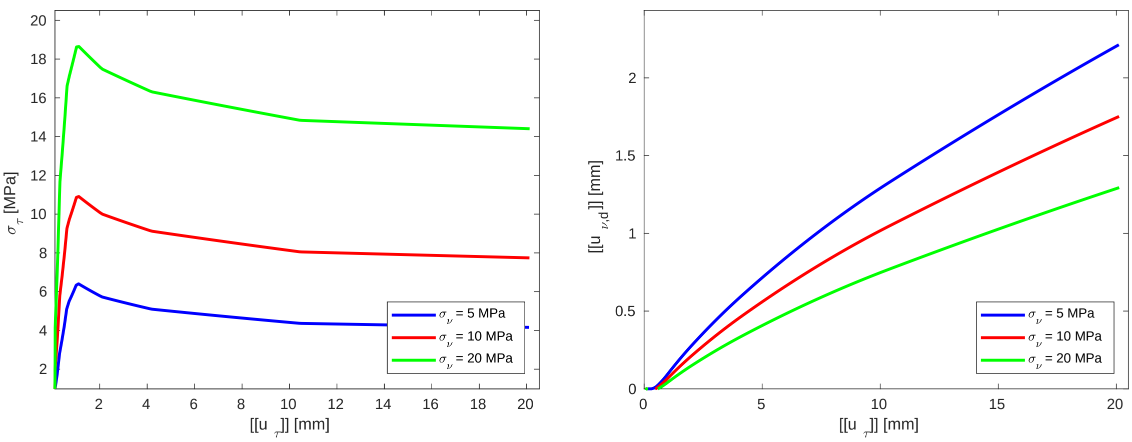

(a) Shear stress-displacement curve.

(b) Dilation vs shear displacement curve.

Figure 7.26: Effects of the compression normal load on shear stress and dilation curves.

model. Example 7.3.4 consists on a depletion of a porous domain with a complex network of fracture. Finally, example 7.3.3 consists on a study on the influence of fracture parameters on the permeability of a fractured porous domain.

For all the following cases, the Biot coefficient for both porous medium and fractures is equal to one, $\alpha = \alpha_f = 1.0$. In order to highlight the influence of the fractures on the permeability of the whole domain, changes in the matrix permeability will be neglected.

7.3.1 Depletion of a single horizontal fracture porous media

For the first example, consider a square domain with $L_x = L_y = 100$ m containing a single horizontal fracture $\Sigma \times \left[-\frac{w}{2}, \frac{w}{2}\right]$, with $\Sigma = \{(x, y) \in \mathbb{R}^2;\ 25 \leq x \leq 75,\ y = 50\}$. Figure 7.27(a) shows the finite element mesh with the domain dimensions. The fracture is highlighted with the red color. The domain is subjected to a vertical *in situ* stress of 50 MPa and a prescribed fluid pressure of 45.10 MPa on the top edge ($y = 100$ m) and 44.90 MPa on the bottom edge ($y = 0$ m), as shown on Fig. 7.27(b). The pressure is then progressively reduced, as shown on Fig. 7.27(c).

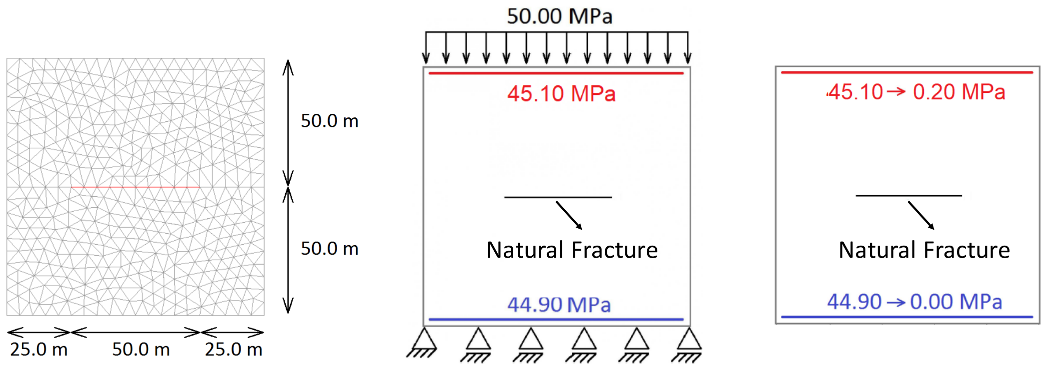

(a) (b) (c)

Figure 7.27: Depletion on a porous media containing a single horizontal fracture: (a) Geometry of the problem and finite element mesh. (b) Boundary conditions on the reference configuration. (c) Depletion.

The porous domain have a Young modulus $E = 16.9$ GPa, Poisson coefficient $\nu = 0.3$, and a isotropic permeability K $= 1.0 \times 10^{-2}$ mD, while the fracture has an initial normal stiffness $k_{ni} = 12041.0$ MPa/m, maximum closure $V_m = 6.5 \times 10^{-5}$ m, initial permeability $K_{f,\tau 0} = 1.0 \times 10^5$ mD, initial aperture $w_0 = 6.5 \times 10^{-5}$ m, $JRC = 15$, $JCS = 150$ MPa and $\phi = 32°$.

Note that in the reference configuration the pressure on the fracture is $p_f = 45.0$ MPa, and consequently its vertical effective stress is $\sigma_y = 5$ MPa. The progressive reduction of pressure increases the normal compressive effective stresses on the fracture without shearing, consequently causing the fracture to close, similar to a compression test. Figure 7.28 shows a comparison of the Barton-Bandis curve for normal deformation and curve of the vertical effective stress on the middle part of the fracture (i.e. $x = 50$ and $y = 50$) versus the fracture closure.

7.3.2 Permeability change due to edometric depletion of a porous media with a fracture network

A more complicated fracture network is considered in this example. The domain geometry is a square with dimensions $L_x = L_y = 100$ m and a complex fracture network, which contains

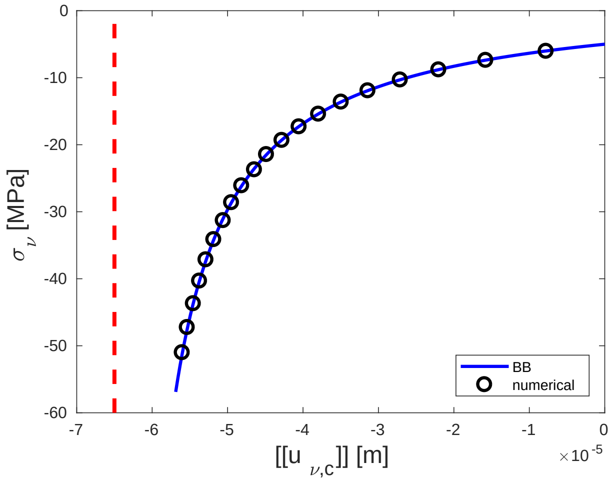

Figure 7.28: Fracture normal stress-displacement due to depletion.

fractures of different orientation and length intersecting each other, as shown on Fig. 7.29(a). The finite element mesh is shown on Fig. 7.29(b). The domain is subjected to an edometric boundary condition, which is representative of a reservoir stress state, with a vertical *in situ* stress $\sigma_y = 50$ MPa and a prescribed fluid pressure of 45.10 MPa on the top edge ($y = 100$ m) and 45.00 MPa on the bottom edge ($y = 0$ m), as shown on Fig. 7.29(c). The pressure is then progressively reduced, as shown on Fig. 7.29(d).

The material properties of the porous domain are the same from 7.3: Young modulus $E = 16.9$ GPa, Poisson coefficient $\nu = 0.3$, and a isotropic permeability K $= 1.0 \times 10^{-2}$ mD. For simplicity, it is assumed that all fractures have the same material properties. The initial normal stiffness is assumed $k_{ni} = 1.0 \times 10^5$ MPa/m, with initial aperture $w_0 = 6.5 \times 10^{-5}$ m, maximum closure $V_m = 6.5 \times 10^{-5}$ m, initial fracture permeability $K_{f,\tau 0} = 1.0 \times 10^5$ mD, $JRC = 15$, $JCS = 150$ MPa and $\phi = 32°$. Fracture models conventionally assume constant values of JRC and JCS based on an average joint length (KOBAYASHI; FUJITA; CHIJIMATSU, 2001), and constant friction angle based on the residual value (MIN et al., 2004). Given the complex geometry of the fracture network, a common length $L = 10.0$ m was adopted for all the fractures.

Figure 7.30 shows the pressure field and the pressure along the cut lines $y = 25.00$ m, $y = 50.00$ m and $y = 75.00$ m for three different pairs of applied boundary pressures: 45.00 MPa and 44.90 MPa, 25.10 MPa and 25.00 MPa and 4.85 MPa and 4.75. Since fracture's permeability is higher than the porous matrix, the pressure tends to remains constant along the fracture, forming a preferential path for flow. As the pressure is depleted, the effective compressive stress increases, causing the fractures to close and reduce its permeability. As a consequence, fractures permeability becomes closer to the porous matrix and the pressure field becomes more uniform.

In order to measure the effect of fracture's deformations on the overall permeability, the

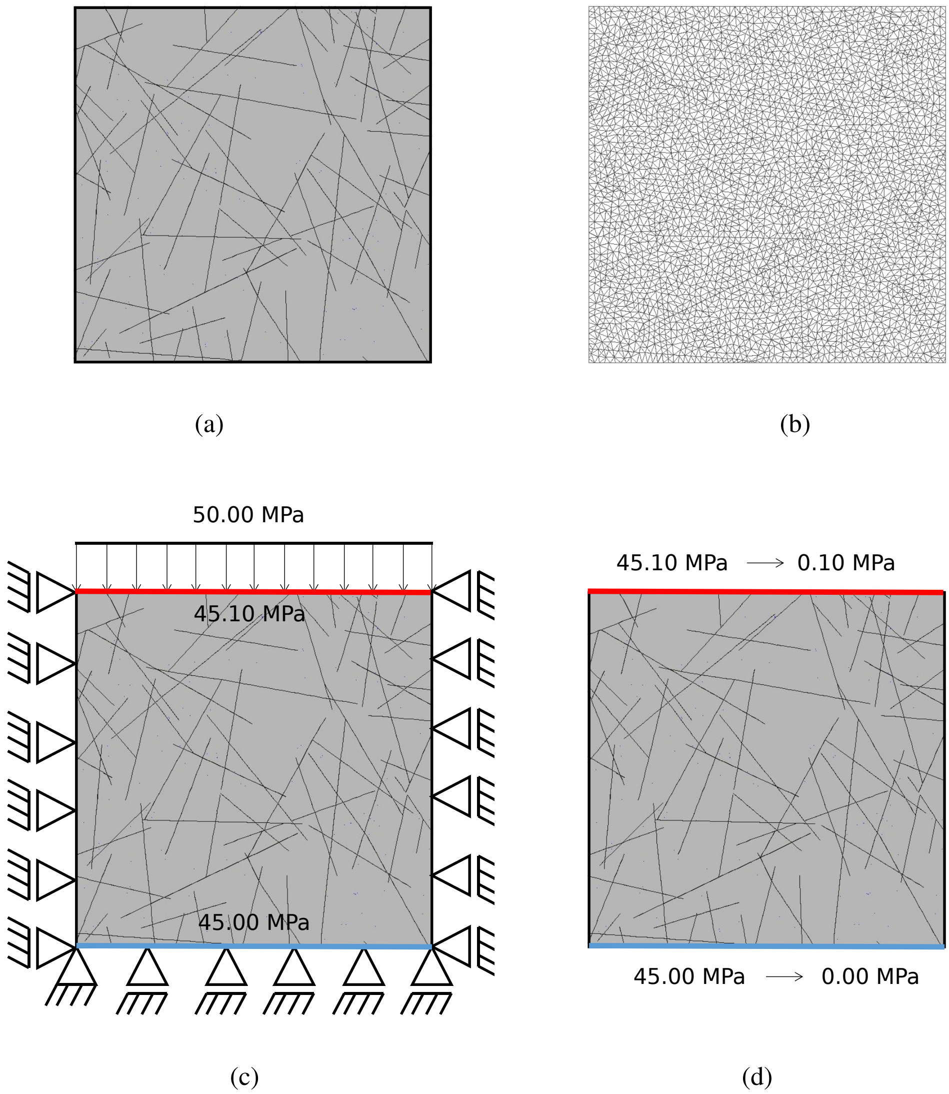

Figure 7.29: Depletion on a porous media with a fracture network. (a) Geometry of the problem. (b) Finite element mesh. (c) Boundary conditions on the reference configuration. (d) Depletion.

equivalent permeability K_{eq} is employed, given by the following equation:

$$K_{eq} = \frac{\mu \cdot Q \cdot L}{A \cdot \Delta P}, \tag{7.1}$$

where Q is the flow rate in the gradient direction, A is the cross section area perpendicular to the flow direction, L is the length of the region in the flow parallel direction and ΔP is the difference of pressure. Figure 7.31 shows the equivalent permeability as a function of pressure. Note that in the initial state the equivalent permeability of the overall domain is almost 40 times higher than the porous matrix permeability. The equivalent permeability progressively reduces as a consequence of the pressure depletion. After a depletion of 45.00 MPa, which is a much higher depletion than a reservoir usually experiences, the equivalent permeability value about 2.5 times higher than the porous matrix permeability, showing a great influence of the fracture

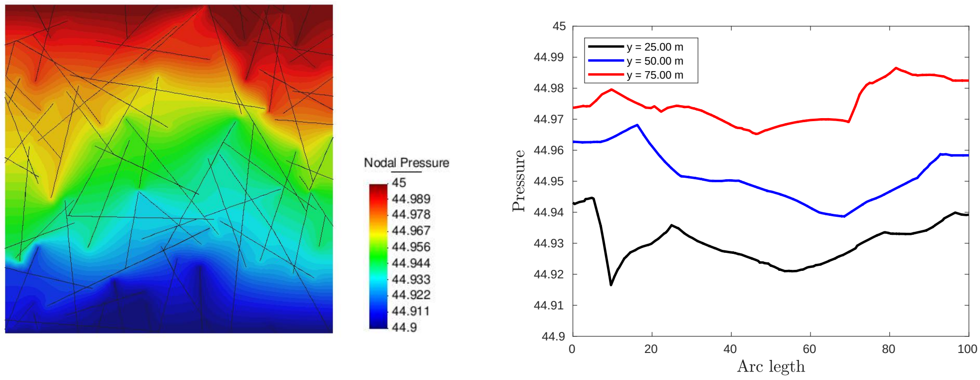

(a)

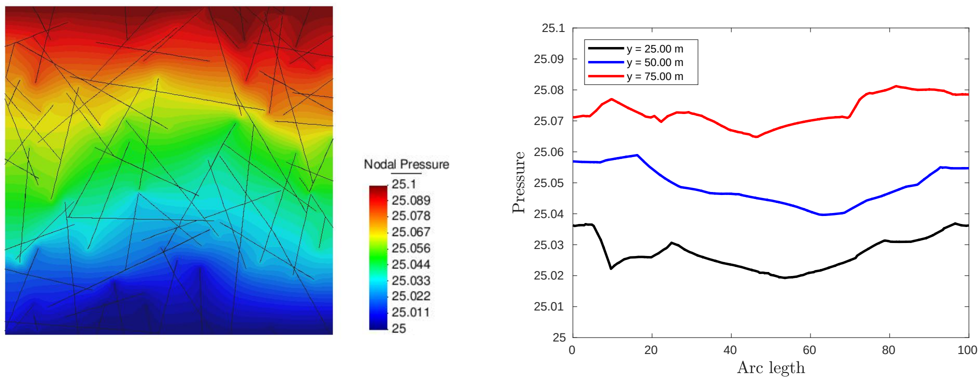

(b)

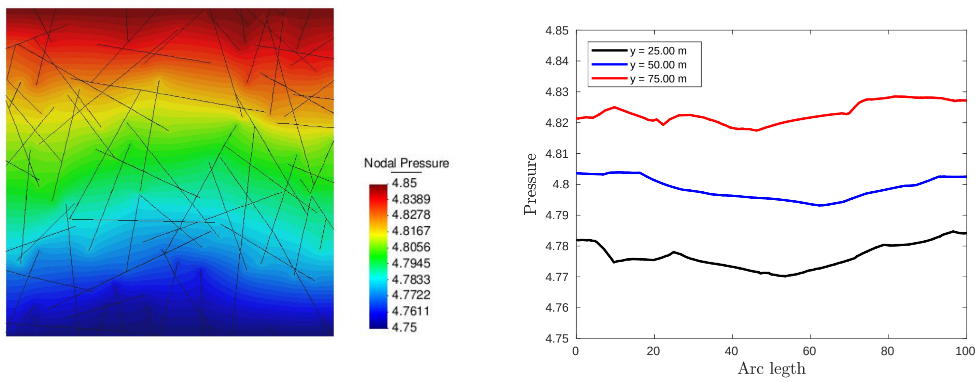

(c)

Figure 7.30: Pressure field along the cut lines $y = 25.00$ m, $y = 50.00$ m and $y = 75.00$ m. (a) Pressures 45.00 MPa and 44.90 MPa. (b) 25.10 MPa and 25.00 MPa. (c) 4.85 MPa and 4.75 MPa.

network on the overall flow.

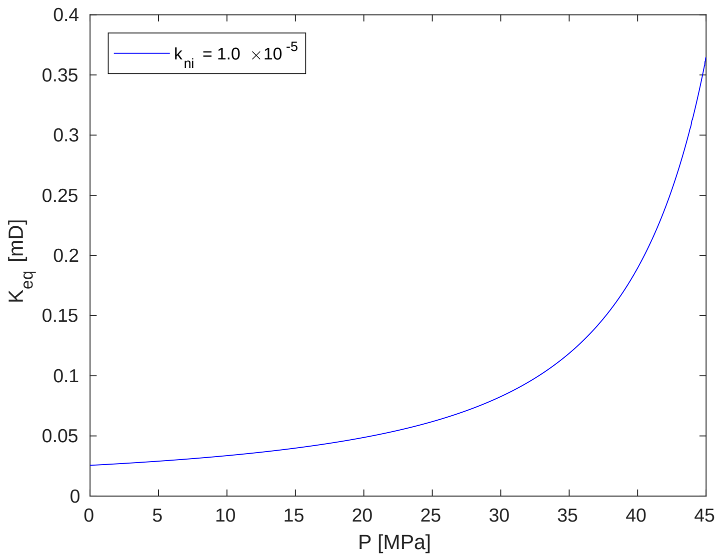

Figure 7.31: Equivalent permeability reduction due to depletion.

7.3.3 Influence of fracture parameters on the overall permeability

Under edometric boundary condition the stress ratio, defined as the ratio of the maximum to minimum principal stresses, is too small to cause shear failure of fractures (see Fig. 7.32). As a consequence, the normal stresses is expected to be the main mechanism of fracture deformation, leading to a general decrease of permeability of rock masses.

In order to investigate the influence of the fracture initial normal stiffness k_{ni}, the same test case was performed with, $k_{ni} = 1.0 \times 10^5$ MPa/m, $k_{ni} = 1.0 \times 10^4$ MPa/m and $k_{ni} = 1.0 \times 10^3$ MPa/m, and maintaining fixed all the other parameters. Figure 7.33 compares the equivalent permeability for the different values of k_{ni}. As pointed on sec. 7.2.2, the stiffer the fracture, the less it closes and the higher the equivalent permeability.

The influence of the roughness coefficient JRC is evaluated by comparing the equivalent permeability for $JRC = 15$ and $JRC = 5$. As shown on Fig. 7.34, the two curves are nearly identical, suggesting that for edometric conditions shear dilation has a small effect and the fracture deformation is indeed governed by the normal stress.

7.3.4 Permeability change due to increase of stress ratio

In order to observe the influence of shear dilation on the overall permeability, a stress boundary condition with increasing ratio of horizontal to vertical stress is applied, as illustrated by

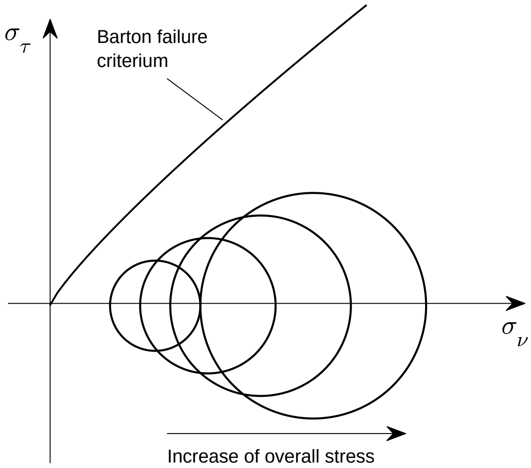

Figure 7.32: Increase of stress magnitude under edometric conditions and the Barton-Bandis criteria. No shear failure is expected

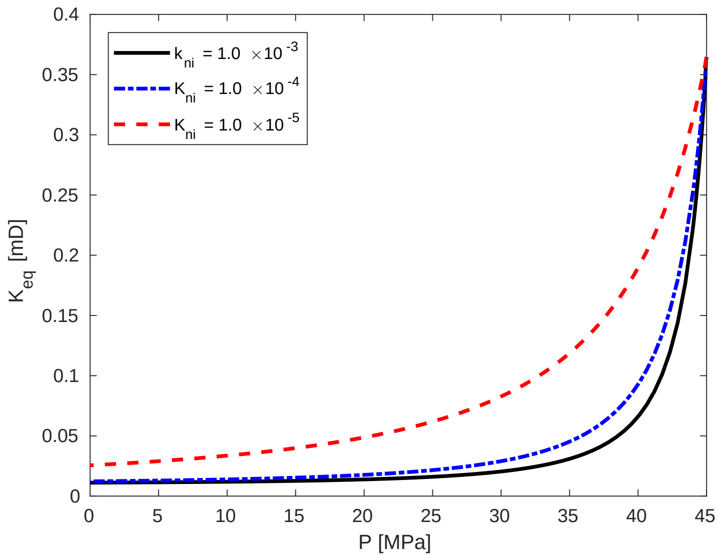

Figure 7.33: Equivalent permeability for different normal initial stiffness.

Fig. 7.35. The vertical *in situ* stress 50.00 MPa is maintained fixed, with a prescribed fluid pressure of 45.10 MPa on the top edge and 45.00 MPa on the bottom edge. The horizontal *in situ* stress 47.50 MPa is progressively increased in steps until 75.00 MPa, increasing the stress ratio R of horizontal to vertical effective stress, $R = \sigma_x/\sigma_y$, from 0.5 to 5.0. By keeping the vertical stress constant, it is expected that shear failure to be induced in some critically oriented fractures by larger differential stresses, as illustrated by Fig. 7.36.

Figure 7.37 shows the equivalent permeability as a function of the stress ratio R. As can be seen, for stress ratio values between 0.5 and 1.5 the equivalent permeability is decreasing and the increase of normal stress is the mechanism governing the permeability changes. When stress

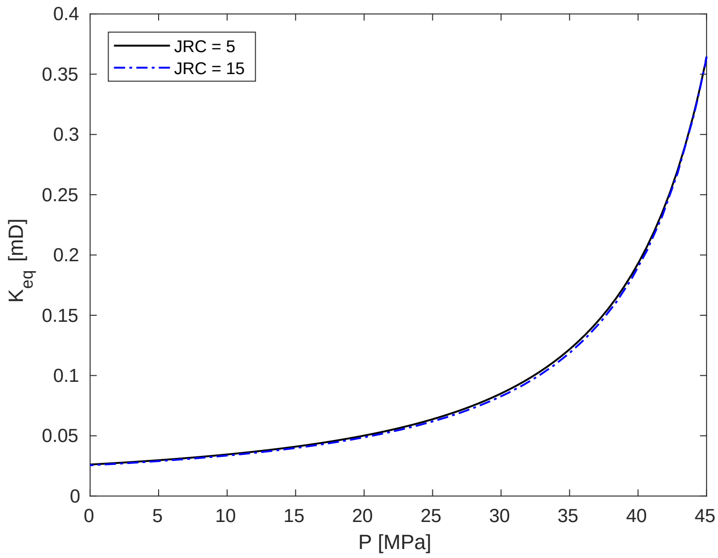

Figure 7.34: Equivalent permeability for different roughness coefficient JRC.

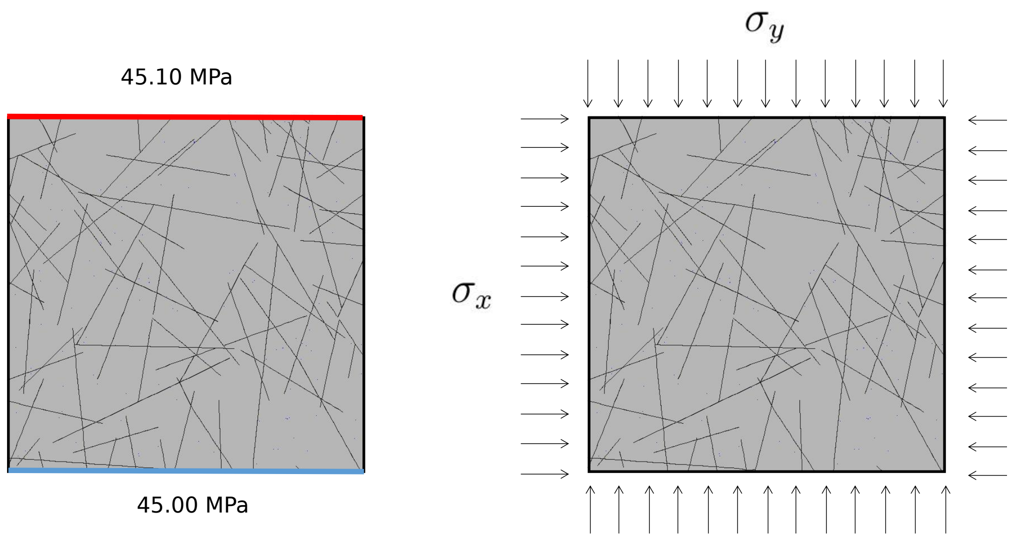

(a) (b)

Figure 7.35: Increasing stress ratio case. (a) Stress boundary condition. (b) Pressure gradient.

ratio becomes higher than 1.5, shear failure starts on fractures and dilation causes fractures to open, increasing the equivalent permeability by orders of magnitude. At this point when shearing begins, shear dilation takes the control of the variations in the equivalent permeability.

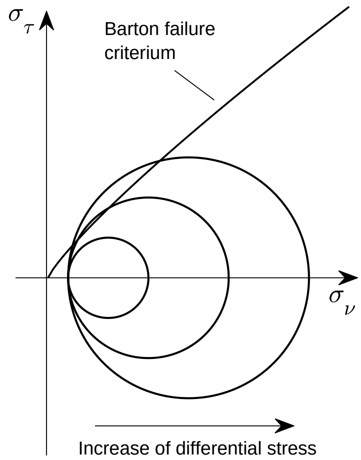

Figure 7.36: Increase of differential stress magnitude with the Barton-Bandis criteria. It is expected shear failure for some critically oriented fractures.

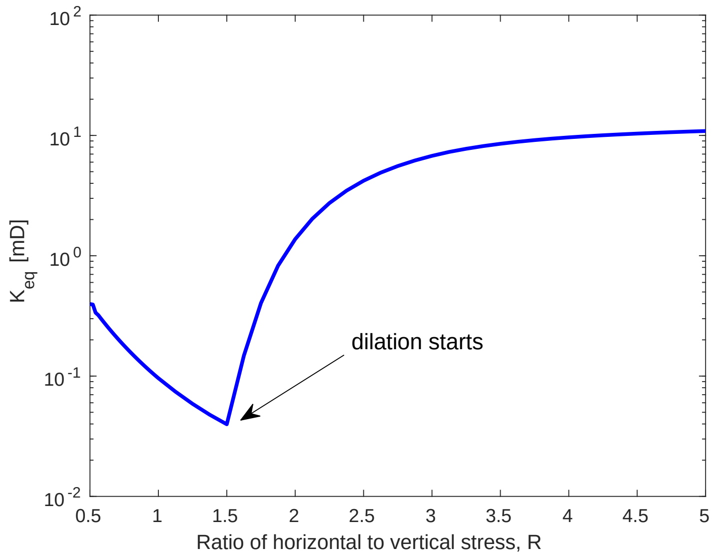

Figure 7.37: Equivalent permeability as a function of stress ratio.

CHAPTER 8

CONCLUSIONS

This work presents a numerical scheme to treat fluid flow and geomechanics in fractured porous media on $\mathbb{R}^d$, $d = 2$ or 3. The reduced dimension model for fluid flow was developed following Angot, Boyer e Hubert (2009), where the fracture domain, whose width is small compared to its length, is modeled as a $d - 1$ dimensional surface. According to the reduced dimension model, the pressure field is (possibly) discontinuous across the fractures. Thus a regularization method was employed to treat the pressure discontinuities. A finite element scheme is proposed, where a narrow *regularization band* containing the 1D fracture is discretized by 2D interface triangular elements with high aspect ratio (HAR elements). This kind of interface elements, combined with an appropriated constitutive model, are able to treat the 1D Darcy-type equations of the fracture as a limit case of the 2D Darcy-type equations of the surrounding porous medium.

The model for coupled flow and geomechanics is an extension of the of the reduced dimension model to account geomechanical deformations of fractures. The Barton-Bandis constitutive model was adopted to describe fracture's deformation. The discontinuous displacement field on the fracture was regularized similarly to the pressure field. A continuum (stress-strain) constitutive model was proposed to describe the discrete (stress-displacement) Barton-Bandis model on the *regularization band*. The finite element scheme for geomechanics is similar to the flow.

Numerical tests are used to demonstrate the efficiency of the proposed scheme. The flow model was proved able to treat at the same time, in the same model, the case where there is a small permeability in the fracture, which involves a pressure discontinuity, the case where there is a large permeability in the fracture, which involves a velocity discontinuity, and the anisotropic case where both phenomena appear combined. The solutions obtained by the scheme shown good agreement with the solutions obtained by solving the global Darcy problem refined meshes where the fracture domain is properly discretized. The number of required degrees of freedom saved with the use of the interface model proves the relevance of the model, spatially for large permeability jumps. The fracture continuum constitutive model was able to properly describe the main features of the Barton-Bandis model: the hyperbolic relation between normal stress-fracture closure, fracture's shear strength, dilation and roughness degradation. Finally, the coupled flow and geomechanics model was used to investigate the effects of a fracture network on the permeability of a porous rock domain, as well as the influence of the stress state. It was shown that the fracture network contribute to increase the overall permeability of the domain. The influence of the stress state was investigated by considering two cases: pressure depletion under edometric state and increase of the stress ratio. On the depletion case, it was shown that shear failure is not expected and the changes in the equivalent permeability are dominated by changes in the normal stress. On the case of increasing stress ratio, where the vertical stress is maintained constant and the horizontal stress is progressively increased. It was shown that for high values of stress ratio, shear failure occurs in the fractures and shear dilation dominates the changes in the equivalent permeability, causing it to increase.

The main feature of the proposed numerical scheme is its simplicity: since the interface HAR elements are essentially the usual linear tree-noded triangular element for $d = 2$, the method can be easily incorporated in any commercial finite element software by introducing the proposed constitutive model and performing some changes in the pre-processing phase, avoiding the need of implement any new element. The case $d = 3$ is only addressed on the theoretical development, but can be treated similarly to the case $d = 2$ by using the four-noded tetrahedral elements with high aspect ratio to discretize the *regularization band*.

Bibliography

AHMED, R. et al. Control-volume distributed multi-point flux approximation coupled with a lower-dimensional fracture model. *Journal of Computational Physics*, v. 284, p. 462 – 489, 2015. ISSN 0021-9991. Disponível em: <http://www.sciencedirect.com/science/article/pii/S0021999114008705>.

ALBOIN, C. et al. Domain decomposition for flow in porous media with fractures. Citeseer, 1999.

AMADEI, B.; STEPHANSSON, O. *Rock stress and its measurement*. [S.l.]: Springer Science & Business Media, 1997.

ANGOT, P.; BOYER, F.; HUBERT, F. Asymptotic and numerical modelling of flows in fractured porous media. *ESAIM: Mathematical Modelling and Numerical Analysis*, EDP Sciences, v. 43, n. 2, p. 239–275, 2009.

ARBOGAST, T.; DOUGLAS JR, J.; HORNUNG, U. Derivation of the double porosity model of single phase flow via homogenization theory. *SIAM Journal on Mathematical Analysis*, SIAM, v. 21, n. 4, p. 823–836, 1990.

BACA, R. G.; ARNETT, R. C.; LANGFORD, D. W. Modelling fluid flow in fractured-porous rock masses by finite-element techniques. *International Journal for Numerical Methods in Fluids*, v. 4, n. 4, p. 337–348, 1984. Disponível em: <https://onlinelibrary.wiley.com/doi/abs/10.1002/fld.1650040404>.

BANDIS, S.; LUMSDEN, A.; BARTON, N. Experimental studies of scale effects on the shear behaviour of rock joints. *International Journal of Rock Mechanics and Mining Sciences & Geomechanics Abstracts*, v. 18, n. 1, p. 1 – 21, 1981. ISSN 0148-9062. Disponível em: <http://www.sciencedirect.com/science/article/pii/014890628190262X>.

BANDIS, S. C.; LUMSDEN, A. C.; BARTON, N. R. Fundamentals of rock joint deformation. *Int. J. Rock Mech. Min. Sci. & Geomech*, v. 20, n. 6, p. 249–268, 1983.

BARENBLATT, G.; ZHELTOV, I. P.; KOCHINA, I. Basic concepts in the theory of seepage of homogeneous liquids in fissured rocks [strata]. *Journal of applied mathematics and mechanics*, Pergamon, v. 24, n. 5, p. 1286–1303, 1960.

BARTON, N. Review of a new shear-strength criterion for rock joints. *Engineering Geology*, v. 7, p. 287–332, 1973.

BARTON, N. The shear strength of rock and rock joints. In: ELSEVIER. *International Journal of rock mechanics and mining sciences & Geomechanics abstracts*. [S.l.], 1976. v. 13, n. 9, p. 255–279.

BARTON, N. *Modelling rock joint behavior from in situ block tests: implications for nuclear waste repository design*. [S.l.]: Office of Nuclear Waste Isolation, Battelle Project Management Division, 1982.

BARTON, N.; BANDIS, S.; BAKHTAR, K. Strength, deformation and conductivity coupling of rock joints. In: ELSEVIER. *International Journal of Rock Mechanics and Mining Sciences & Geomechanics Abstracts*. [S.l.], 1985. v. 22, n. 3, p. 121–140.

BARTON, N.; CHOUBEY, V. The shear strength of rock joints in theory and practice. *Rock Mechanics*, v. 1/2, p. 1–54, 1977.

BIOT, M. A. General theory of three-dimensional consolidation. *Journal of applied physics*, AIP, v. 12, n. 2, p. 155–164, 1941.

BORJA, R. I. On the mechanical energy and effective stress in saturated and unsaturated porous continua. *International Journal of Solids and Structures*, Elsevier, v. 43, n. 6, p. 1764–1786, 2006.

BUDHU, M. Earth fissure formation from the mechanics of groundwater pumping. *International Journal of Geomechanics*, v. 11, n. 1, p. 1–11, 2011. Disponível em: <https://ascelibrary.org/doi/abs/10.1061/%28ASCE%29GM.1943-5622.0000060>.

COUSSY, O. *Poromechanics*. [S.l.]: John Wiley & Sons, 2004.

COUSSY, O. *Mechanics and physics of porous solids*. [S.l.]: John Wiley & Sons, 2011.

DAVID, C. et al. Laboratory measurement of compaction-induced permeability change in porous rocks: Implications for the generation and maintenance of pore pressure excess in the crust. *pure and applied geophysics*, v. 143, n. 1, p. 425–456, Mar 1994. ISSN 1420-9136. Disponível em: <https://doi.org/10.1007/BF00874337>.

DEAN, R.; LO, L. et al. Simulations of naturally fractured reservoirs. *SPE reservoir engineering*, Society of Petroleum Engineers, v. 3, n. 02, p. 638–648, 1988.

DUSSEAULT, M. B. Geomechanical challenges in petroleum reservoir exploitation. *KSCE Journal of Civil Engineering*, v. 15, n. 4, p. 669–678, Apr 2011. ISSN 1976-3808. Disponível em: <https://doi.org/10.1007/s12205-011-0007-5>.

FAILLE, I. et al. A new fault model in geological basin modelling. application of finite volume scheme and domain decomposition methods. In: *Finite volumes for complex applications*. [S.l.: s.n.], 2002. v. 3, p. 543–550.

FAILLE, I. et al. Model reduction and discretization using hybrid finite volumes for flow in porous media containing faults. *Computational Geosciences*, v. 20, n. 2, p. 317–339, Apr 2016. ISSN 1573-1499. Disponível em: <https://doi.org/10.1007/s10596-016-9558-3>.

FLEMISCH, B. et al. Benchmarks for single-phase flow in fractured porous media. *Advances in Water Resources*, v. 111, p. 239 – 258, 2018. ISSN 0309-1708. Disponível em: <http://www.sciencedirect.com/science/article/pii/S0309170817300143>.

FREDRICH, J. T. et al. Geomechanical modeling of reservoir compaction, surface subsidence, and casing damage at the belridge diatomite field. *SPE Reservoir Evaluation & Engineering*, Society of Petroleum Engineers, v. 3, n. 04, p. 348–359, 2000.

FRIH, N.; ROBERTS, J. E.; SAADA, A. Modeling fractures as interfaces: a model for forchheimer fractures. *Computational Geosciences*, v. 12, n. 1, p. 91–104, Mar 2008. ISSN 1573-1499. Disponível em: <https://doi.org/10.1007/s10596-007-9062-x>.

GEERTSMA, J. et al. The effect of fluid pressure decline on volumetric changes of porous rocks. Society of Petroleum Engineers, 1957.

GENS, A.; CAROL, I.; ALONSO, E. A constitutive model for rock joints formulation and numerical implementation. *Computers and Geotechnics*, v. 9, n. 1, p. 3 – 20, 1990. ISSN 0266-352X. Special Issue on Soil-Structure Interaction. Disponível em: <http://www.sciencedirect.com/science/article/pii/0266352X9090026R>.

GLäSER, D. et al. A discrete fracture model for two-phase flow in fractured porous media. *Advances in Water Resources*, v. 110, p. 335 – 348, 2017. ISSN 0309-1708. Disponível em: <http://www.sciencedirect.com/science/article/pii/S0309170817304414>.

GOODMAN, R. E. The mechanical properties of joints. In: ISMR. *3rd ISRM Congress*. Denver, 1974. v. 1A, p. 127–140.

GOODMAN, R. E.; TAYLOR, R. L.; BREKKE, T. L. A model for the mechanics of jointed rock. *Journal of the Soil Mechanics and Foundations Division*, v. 94, n. 3, p. 637–660, 1968.

HENCHER, S. R.; RICHARDS, L. R. Assessing the shear strength of rock discontinuities at laboratory and field scales. *Rock Mechanics and Rock Engineering*, v. 48, n. 3, p. 883–905, May 2015. ISSN 1434-453X. Disponível em: <https://doi.org/10.1007/s00603-014-0633-6>.

HOMAND, F.; BELEM, T.; SOULEY, M. Friction and degradation of rock joint surfaces under shear loads. *International Journal for Numerical and Analytical Methods in Geomechanics*, v. 25, n. 10, p. 973–999, 2001. Disponível em: <https://onlinelibrary.wiley.com/doi/abs/10.1002/nag.163>.

JACKSON, C. P.; HOCH, A. R.; TODMAN, S. Self-consistency of a heterogeneous continuum porous medium representation of a fractured medium. *Water Resources Research*, v. 36, n. 1, p. 189–202, 2000. Disponível em: <https://agupubs.onlinelibrary.wiley.com/doi/abs/10.1029/1999WR900249>.

JAEGER, J. Friction of rocks and stability of rock slopes. *Geotechnique*, Thomas Telford Ltd, v. 21, n. 2, p. 97–134, 1971.

JAFFRÉ, J.; MNEJJA, M.; ROBERTS, J. A discrete fracture model for two-phase flow with matrix-fracture interaction. *Procedia Computer Science*, v. 4, p. 967 – 973, 2011. ISSN 1877-0509. Proceedings of the International Conference on Computational Science, ICCS 2011. Disponível em: <http://www.sciencedirect.com/science/article/pii/S1877050911001608>.

JING, L. *Numerical modelling of jointed rock masses by distinct element method for two-and three-dimensional problems*. Tese (Doutorado) — Luleå tekniska universitet, 1990.

JING, L.; STEPHANSSON, O. *Fundamentals of discrete element methods for rock engineering: theory and applications*. [S.l.]: Elsevier, 2007.

JR, J. D.; ARBOGAST, T. Dual porosity models for flow in naturally fractured reservoirs. *Dynamics of Fluids in Hierarchical Porous Media*, Academic Press London, UK, p. 177–221, 1990.

KARIMI-FARD, M. et al. An efficient discrete fracture model applicable for general purpose reservoir simulators. In: SOCIETY OF PETROLEUM ENGINEERS. *SPE Reservoir Simulation Symposium*. [S.l.], 2003.

KARIMI-FARD, M.; FIROOZABADI, A. et al. Numerical simulation of water injection in 2d fractured media using discrete-fracture model. In: SOCIETY OF PETROLEUM ENGINEERS. *SPE annual technical conference and exhibition*. [S.l.], 2001.

KAZEMI, H. et al. Numerical simulation of water-oil flow in naturally fractured reservoirs. *Society of Petroleum Engineers Journal*, Society of Petroleum Engineers, v. 16, n. 06, p. 317–326, 1976.

KOBAYASHI, A.; FUJITA, T.; CHIJIMATSU, M. Continuous approach for coupled mechanical and hydraulic behavior of a fractured rock mass during hypothetical shaft sinking at sellafield, uk. *International Journal of Rock Mechanics and Mining Sciences*, v. 38, n. 1, p. 45 – 57, 2001. ISSN 1365-1609. Decovalex II. Disponível em: <http://www.sciencedirect.com/science/article/pii/S1365160900000630>.

KRSMANOVIĆ, D.; LANGOF, Z. Large scale laboratory tests of the shear strength of rocky material. In: *Grundfragen auf dem Gebiete der Geomechanik/Principles in the Field of Geomechanics*. [S.l.]: Springer, 1964. p. 20–30.

LADANYI, B.; ARCHAMBAULT, G. et al. Simulation of shear behavior of a jointed rock mass. In: AMERICAN ROCK MECHANICS ASSOCIATION. *The 11th US Symposium on Rock Mechanics (USRMS)*. [S.l.], 1969.

LEE, S. et al. An efficient finite difference model for flow in a reservoir with multiple length-scale fractures. In: SOCIETY OF PETROLEUM ENGINEERS. *SPE Annual Technical Conference and Exhibition*. [S.l.], 1999.

LI, L.; LEE, S. H. et al. Efficient field-scale simulation for black oil in a naturally fractured reservoir via discrete fracture networks and homogenized media. In: SOCIETY OF PETROLEUM ENGINEERS. *International oil & gas conference and exhibition in China*. [S.l.], 2006.

LOMIZE, G. Water flow through jointed rock. *Gosenergoizdat, Moscow*, p. 127, 1951.

LONG, J. C. S. et al. Porous media equivalents for networks of discontinuous fractures. *Water Resources Research*, v. 18, n. 3, p. 645–658, 1982. Disponível em: <https://agupubs.onlinelibrary.wiley.com/doi/abs/10.1029/WR018i003p00645>.

MANZOLI, O. et al. Modeling of interfaces in two-dimensional problems using solid finite elements with high aspect ratio. *Computers & Structures*, Elsevier, v. 94, p. 70–82, 2012.

MANZOLI, O. et al. Modeling of multiple cracks in reinforced concrete members using solid finite elements with high aspect ratio. *Computational Modelling of Concrete Structures*, CRC Press, p. 383, 2014.

MANZOLI, O. L. et al. On the use of high aspect ratio finite elements to model hydraulic fracturing in deformable porous media. *Computer Methods in Applied Mechanics and Engineering*, v. 350, p. 57 – 80, 2019. ISSN 0045-7825. Disponível em: <http://www.sciencedirect.com/science/article/pii/S0045782519301355>.

MANZOLI, O. L. et al. On the use of finite elements with a high aspect ratio for modeling cracks in quasi-brittle materials. *Engineering Fracture Mechanics*, v. 153, p. 151 – 170, 2016. ISSN 0013-7944. Disponível em: <http://www.sciencedirect.com/science/article/pii/S001379441500702X>.

MARTIN, V.; JAFFRÉ, J.; ROBERTS, J. E. Modeling fractures and barriers as interfaces for flow in porous media. *SIAM Journal on Scientific Computing*, SIAM, v. 26, n. 5, p. 1667–1691, 2005.

MIN, K.-B. et al. Stress-dependent permeability of fractured rock masses: a numerical study. *International Journal of Rock Mechanics & Mining Sciences*, v. 41, p. 1191–1210, 2004.

MORALES, F.; SHOWALTER, R. The narrow fracture approximation by channeled flow. *Journal of Mathematical Analysis and Applications*, v. 365, n. 1, p. 320 – 331, 2010. ISSN 0022-247X. Disponível em: <http://www.sciencedirect.com/science/article/pii/S0022247X09008762>.

MORALES, F.; SHOWALTER, R. E. Interface approximation of darcy flow in a narrow channel. *Mathematical Methods in the Applied Sciences*, v. 35, n. 2, p. 182–195, 2012. Disponível em: <https://onlinelibrary.wiley.com/doi/abs/10.1002/mma.1555>.

ODA, M. Permeability tensor for discontinuous rock masses. *Géotechnique*, v. 35, n. 4, p. 483–495, 1985. Disponível em: <https://doi.org/10.1680/geot.1985.35.4.483>.

OLIVER, J. et al. Stability and robustness issues in numerical modeling of material failure with the strong discontinuity approach. *Computer Methods in Applied Mechanics and Engineering*, v. 195, n. 52, p. 7093 – 7114, 2006. ISSN 0045-7825. Computational Modelling of Concrete. Disponível em: <http://www.sciencedirect.com/science/article/pii/S0045782505003920>.

OLIVER, J.; HUESPE, A.; CANTE, J. An implicit/explicit integration scheme to increase computability of non-linear material and contact/friction problems. *Computer Methods in Applied Mechanics and Engineering*, v. 197, n. 21-24, p. 1865 – 1889, 2008. ISSN 0045-7825. Disponível em: <http://www.sciencedirect.com/science/article/pii/S0045782507004756>.

OLSSON, R.; BARTON, N. An improved model for hydromechanical coupling during shearing of rock joints. *International Journal of Rock Mechanics & Mining Sciences*, v. 38, n. 3, p. 317–329, 2001.

PATTON, F. D. et al. Multiple modes of shear failure in rock. In: INTERNATIONAL SOCIETY FOR ROCK MECHANICS. *1st ISRM Congress*. [S.l.], 1966.

PLESHA, M. E. Constitutive models for rock discontinuities with dilatancy and surface degradation. *International Journal for Numerical and Analytical Methods in Geomechanics*, v. 11, n. 4, p. 345–362, 1987. Disponível em: <https://onlinelibrary.wiley.com/doi/abs/10.1002/nag.1610110404>.

REICHENBERGER, V. et al. A mixed-dimensional finite volume method for two-phase flow in fractured porous media. *Advances in Water Resources*, v. 29, n. 7, p. 1020 – 1036, 2006. ISSN 0309-1708. Disponível em: <http://www.sciencedirect.com/science/article/pii/S0309170805002150>.

RUTQVIST, J.; STEPHANSSON, O. The role of hydromechanical coupling in fractured rock engineering. *Hydrogeology Journal*, v. 11, p. 7–40, 2003.

SAEB, S.; AMADEI, B. Modelling rock joints under shear and normal loading. *International Journal of Rock Mechanics and Mining Sciences & Geomechanics Abstracts*, v. 29, n. 3, p. 267 – 278, 1992. ISSN 0148-9062. Disponível em: <http://www.sciencedirect.com/science/article/pii/014890629293660C>.

SAMADHIYA, N. K.; VILADKAR, M. N.; AL-OBAYDI, M. A. Three-dimensional joint/interface element for rough undulating major discontinuities in rock masses. *International Journal of Geomechanics*, v. 8, n. 6, p. 327–335, 2008. Disponível em: <https://ascelibrary.org/doi/abs/10.1061/%28ASCE%291532-3641%282008%298%3A6%28327%29>.

SÁNCHEZ, M.; MANZOLI, O. L.; GUIMARÃES, L. J. Modeling 3-d desiccation soil crack networks using a mesh fragmentation technique. *Computers and Geotechnics*, Elsevier, v. 62, p. 27–39, 2014.

SEGURA, J. M.; CAROL, I. On zero-thickness interface elements for diffusion problems. *International Journal for Numerical and Analytical Methods in Geomechanics*, v. 28, n. 9, p. 947–962, 2004. Disponível em: <https://onlinelibrary.wiley.com/doi/abs/10.1002/nag.358>.

SEGURA, J. M.; CAROL, I. Coupled hm analysis using zero-thickness interface elements with double nodes. part i: Theoretical model. *International Journal for Numerical and Analytical Methods in Geomechanics*, v. 32, n. 18, p. 2083–2101, 2008. Disponível em: <https://onlinelibrary.wiley.com/doi/abs/10.1002/nag.735>.

SEGURA, J. M.; CAROL, I. Coupled hm analysis using zero-thickness interface elements with double nodes—part ii: Verification and application. *International Journal for Numerical and Analytical Methods in Geomechanics*, v. 32, n. 18, p. 2103–2123, 2008. Disponível em: <https://onlinelibrary.wiley.com/doi/abs/10.1002/nag.730>.

SNOW, D. T. A parallel plate model of fractured permeable media. *Ph.D. Thesis, Univ. of California*, 1965. Disponível em: <https://ci.nii.ac.jp/naid/10011929254/en/>.

TERZAGHI, K. Erdbaumechanik auf bodenphysikalischer grundlage. F. Deuticke, 1925.

TSANG, C.-F.; RUTQVIST, J.; MIN, K.-B. Fractured rock hydromechanics: from borehole testing to solute transport and co2 storage. *Geological Society, London, Special Publications*, Geological Society of London, v. 284, n. 1, p. 15–34, 2007. ISSN 0305-8719. Disponível em: <http://sp.lyellcollection.org/content/284/1/15>.

WARREN, J.; ROOT, P. J. et al. The behavior of naturally fractured reservoirs. SPE Journal, 1963.

WITHERSPOON, P. A. et al. Validity of cubic law for fluid flow in a deformable rock fracture. *Water Resources Research*, v. 16, n. 6, p. 1016–1024, 1980. ISSN 1944-7973. Disponível em: <http://dx.doi.org/10.1029/WR016i006p01016>.

WU, Y.-S. et al. A multiple-continuum model for simulating single-phase and multiphase flow in naturally fractured vuggy reservoirs. *Journal of Petroleum Science and Engineering*, v. 78, n. 1, p. 13 – 22, 2011. ISSN 0920-4105. Disponível em: <http://www.sciencedirect.com/science/article/pii/S0920410511001021>.

ZHU, J. B.; LI, H.; DENG, J. H. A one-dimensional elastoplastic model for capturing the nonlinear shear behaviour of joints with triangular asperities based on direct shear tests.

Rock Mechanics and Rock Engineering, Nov 2018. ISSN 1434-453X. Disponível em: <https://doi.org/10.1007/s00603-018-1674-z>.

ZIMMERMAN, R. W.; BODVARSSON, G. S. Hydraulic conductivity of rock fractures. *Transport in Porous Media*, v. 23, n. 1, p. 1–30, Apr 1996. ISSN 1573-1634. Disponível em: <https://doi.org/10.1007/BF00145263>.

ŢENE, M. et al. Projection-based embedded discrete fracture model (pedfm). *Advances in Water Resources*, v. 105, p. 205 – 216, 2017. ISSN 0309-1708. Disponível em: <http://www.sciencedirect.com/science/article/pii/S0309170817300994>.